Using Matrix Product States to study Chiral-Induced Spin Selectivity in Electron Transport

M. B. Ates

Submitted in partial fulfillment of the requirements
for the the degree of Master of Science
at the Delft University of Technology,
to be defended on Friday July 12, 2024.

Student number:	5077990	
Thesis Committee:	Prof. Dr. J. Thijssen	Supervisor
	Prof. Dr. N. Chepiga	
	Prof. Dr. M. Wimmer	

July 17, 2024

ŤUDelft

Abstract

Chirality-induced spin selectivity (CISS) is a general term denoting the interplay between the chiral structure of molecules and the electron spin. CISS has been studied for over two decades, leading to a consistent picture of experimental phenomena. In this thesis, we focus on transport experiments exhibiting CISS. In spite of the efforts of many scientists, there is no theoretical explanation for the high degrees of CISS that have been measured in electron transport experiments. In general, it is agreed upon by theorists that the effect is caused by the interplay between the electronic spin-orbit interaction and the helical molecule geometry, in combination with phase-breaking effects such as electron-electron or electron-phonon interactions. As of yet, no theoretical model has achieved realistic degrees of SOC without drastic inflation of the spin-orbit interaction strength.

In this thesis we explore the possibility of using matrix product states (MPS) to study spin-selectivity in boundary-driven electron transport through tight-binding models of chiral molecules, a novel approach in the field of CISS. To this end, we use a model proposed by Fransson in 2019, which considers interacting electrons in a Hubbard model with a spin-orbit interaction adapted from the Kane-Mele model. In this thesis work, the fermionic Hubbard model is mapped to a double spin chain using the Jordan-Wigner transformation. The state of the system is described by a matrix product density operator (MPDO) which is vectorised to a matrix product state (MPS). The system dynamics are described by a vectorised Lindblad equation. The advantage of this approach lies in the fact that it does not require the use of any systematic approximations to the Hamiltonian, in contrast to previous studies. The developed method is validated against the results of previous works studying the boundary-driven Heisenberg-XXZ model and the boundary-driven Hubbard model.

The method is shown to be capable of reproducing chirality-induced spin-selective effects for short chains. The results of this study show a finite magnetocurrent that is odd in bias voltage with an associated magnetoresistance of less than 1%. This is in line with previous studies of this model, but two orders of magnitude lower than experimentally measured values. However, these results are obtained using highly inflated values for the spin-orbit interaction strength. In multiple cases, the results do not satisfy the Onsager-Casimir and Büttiker reciprocity principles, which state that the magnetocurrent should vanish in the low-driving and in the non-interacting regimes. Moreover, the continuity of the current in the steady state was not fully satisfied. We provide evidence that indicates these problems result from the time-integration error introduced by the Suzuki-Trotter decomposition. We expect that these can be mitigated using higher order time-integration schemes.

From the results of this study we can conclude that matrix product states are a viable tool to study CISS in bound-electron transport. However, the method presented in this thesis suffer from numerical errors. We present several suggestions for improvement which address these shortcomings.

Acknowledgements

First of all, I would like to thank my supervisor, Jos Thijssen, for the guidance he provided during the course of this thesis project, the interesting conversations during our weekly meetings and his efforts to connect me with knowledgeable experts that helped progress this research. It has been a pleasure to work with you the past year. I also want to express my gratitude to Natalia Chepiga and Michael Wimmer, for being part of my thesis committee. I also want to thank my family for always supporting me in what I do and in the decisions

I make, and for pushing me in the right direction when I could use a little guidance. I would not have gotten to where I am now without your guidance and support over the years. Lastly, I want to thank Esmée for her support this past year. Thank you for hearing, understanding and helping me solve the numerous challenges I have faced during the course of this thesis work, thank you for being with me when the times were tough, for being with me when the times were good and for always making the tough times just a little better.

Contents

1 Chiral Induced Spin Selectivity

1.1 CISS in Experiments

Chiral induced spin selectivity, or CISS, is a phenomenon where electrons travelling through a chiral medium exhibit significant spin-polarisation. The effect was first observed in 1999 by Ray et al.[1], who used a laser beam to eject photoelectrons from an Au substrate on which a thin film of chiral molecules was deposited. When the incident light is circularly-polarised, the emitted electrons passing through the film are spin-polarised. For a monolayer of chiral molecules, a difference in electron transmission of up to 12% was shown for opposite electron polarisations (with unpolarised electrons exhibiting an intermediate transmission probability), implying an asymmetry in the scattering probability dependent on the chirality of the film and the spin of the electron. This study hinted at the existence of the CISS effect, however, in this setup the initial polarisations of the electrons could not be measured directly. It would take more than a decade before the conjecture was properly verified by Göhler et al. in 2011 [2], through the use of a Mott polarimeter. This allowed the spin-polarisation of the emitted electrons to be measured directly, unequivocally proving the existence of the CISS effect. In this study, the spin-polarisation of electrons transmitted through a self-assembled monolayer of double-stranded DNA (dsDNA) of 78 base pairs was measured to be over 60% at room temperature, with the degree of polarisation scaling linearly with the number of base pairs. The *spin polarisation* P is defined as

$$P = \frac{N_\uparrow - N_\downarrow}{N_\uparrow + N_\downarrow}, \tag{1.1}$$

with N_σ the number of transmitted electrons with spin-up ($\sigma = \uparrow$) and down ($\sigma = \downarrow$). The spin polarisation is obtained from the *scattering asymmetry A*,

$$A = \frac{I_\uparrow - I_\downarrow}{I_\uparrow + I_\downarrow} = \frac{P}{S}, \tag{1.2}$$

in which $I_\uparrow$ and $I_\downarrow$ denote the electron beam intensities at the two counters of the Mott polarimeter, respectively [3, 4]. S is a setup-dependent constant called the Sherman function, that can be used to relate the scattering asymmetry to the spin-polarisation.

Photoemission experiments are not the only situations in which CISS manifests itself. The term CISS refers to a whole group of related effects in which molecular chirality causes a spin selectivity in electron processes.
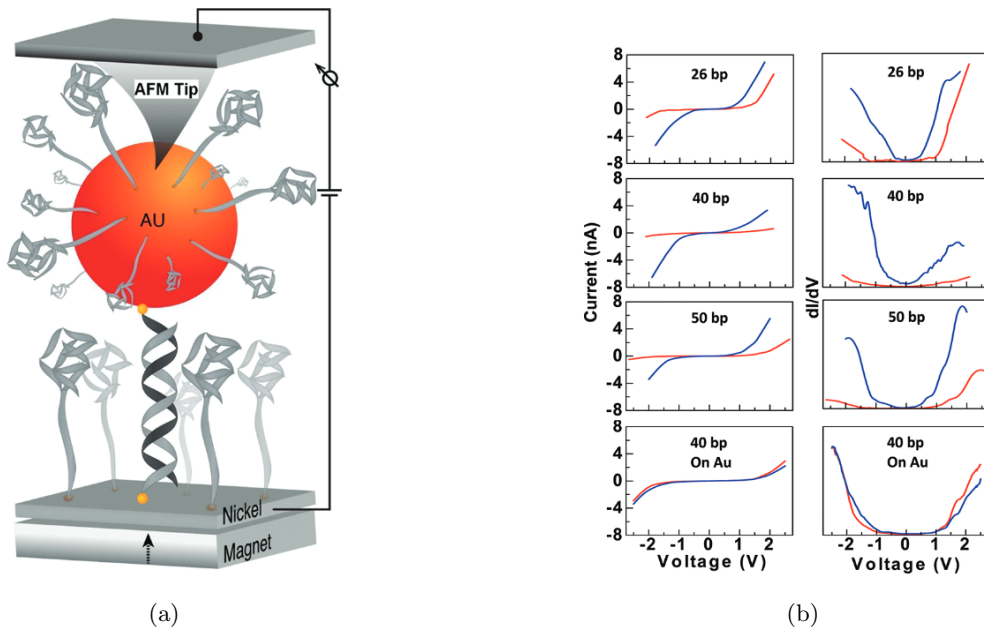
Figure 1.1: (a) Experimental setup used by Xie et al. [5] to measure spin-dependent transport through ds-DNA molecules. The ferromagnetic Nickel electrode is magnetised to control the spin-polarisation of the current through the junction. (b) Measured currents through the dsDNA as a function of applied voltage for different molecule lengths. Red curves indicate up-magnetisation of the Nickel while blue curves indicate down-magnetisation. The difference between the curves is referred to as the magnetocurrent.

Aside from scattering experiments, CISS also manifests itself in conductance experiments; the transport of valence electrons through chiral molecules, which will be the focus of this thesis. CISS in conduction was first observed by Xie et al. in 2011 [5] using a setup where single-stranded DNA (ssDNA) molecules were adsorbed on a Ni surface. Gold nanoparticles with ssDNA molecules bound to it were placed upon the surface, allowing complementary ssDNA molecules on the substrate and particle to form a single double-stranded DNA (dsDNA) molecule, with geometric constraints ensuring only one ds-DNA molecule connected the gold particle to the surface. The tip of an atomic force microscopy (AFM) probe was subsequently brought in close proximity to the nanoparticle, forming a two-terminal transport setup. The ferromagnetic Ni surface was magnetised, causing a splitting in the density of states for electrons oriented parallel and antiparallel to the magnetic field. Consequently, upon application of a bias voltage across the setup, a spin-polarised current would flow through the dsDNA molecule connecting the substrate and gold particle. The measured I/V curves showed a significant dependence of the current on the magnetisation of the substrate: that is, on the spin-polarisation of the electrons travelling through the setup. Again, for unpolarised electrons (an unmagnetised Ni-lead) an I/V curve in between that of the two polarised ones was found. The results of this work are included in figure 1.1b.

In two-terminal conduction setups such as the one used by Xie et al., the CISS effect is characterised by the *magnetoresistance* of the junction, defined as

$$\text{MR} = \frac{I(m,V) - I(-m,V)}{I(m,V) + I(-m,V)} \equiv \frac{\Delta I(m,V)}{I(m,V) + I(-m,V)}, \tag{1.3}$$

with $\Delta I(m,V) \equiv I(m,V) - I(-m,V)$ the measured *magnetocurrent*. The magnetocurrent has been experimentally observed to be dominantly odd in bias voltage (so the magnetoresistance has been found to be dominantly even) and values from 6% to 90% have been measured [6]. In this work, we will exclusively concern ourselves with CISS in transport.

Lastly, CISS has also been reported in electrochemistry studies [7, 8], where spin-polarisation of electrons gave rise to enantioselective effects in chemical reactions.

(a) Setup with a positively-magnetised Ni lead.　　　(b) Setup with a negatively-magnetised Ni lead.
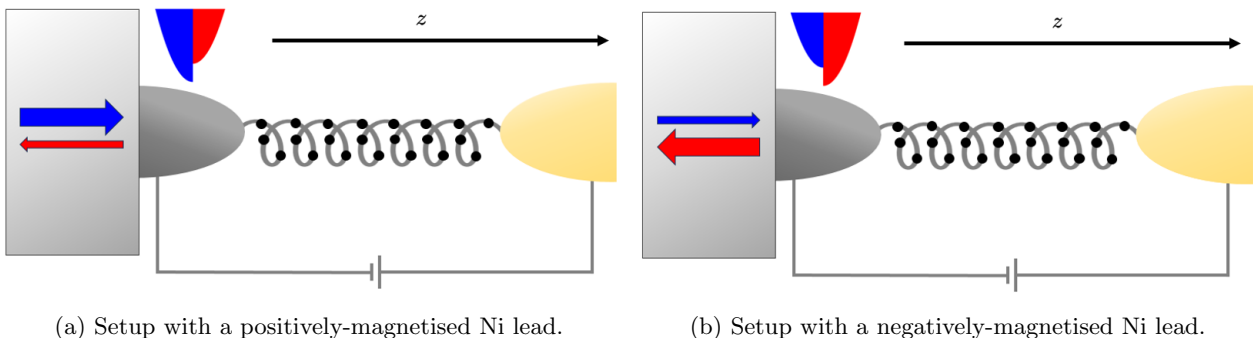
Figure 1.2: Typical transport setup in studies related to CISS. A chiral molecule is connected to two leads, a Nickel lead on the left and a gold lead on the right. The Nickel lead is connected to a magnet, causing the ferromagnetic Nickel lead to magnetise. This results in a spin-dependent shift in the density of electron states in the Nickel, which is depicted in the figure. When a bias voltage is applied across the junction, the electron current passing through the chiral molecule will consequently be spin-polarised.

Before moving on to the theoretical explanation of CISS (or lack thereof), we will discuss some general qualitative properties of the CISS effect. The information presented here is obtained from the recently published review by Bloom and coworkers [9] and the references therein. First and foremost, although the reported magnitudes of spin filtering vary, all studies report that the degree of spin-filtering increases monotonically with the length of the chiral molecules used in the experimental setup. Secondly, a rather unusual feature of CISS is that it exists at high temperatures, even room temperature. Certain theoretical explanations that will be discussed in the next section argue that molecule vibrations perform an assisting role in the spin-filtering process, which could explain the persistence of the effect at high temperatures. Experiments disagree, however, upon the specific temperature dependence of the effect, with some reporting positive correlations, others negative correlations and some even observe no correlation between the two. Even so, the existence of CISS both at low temperatures and at room temperature has been shown unequivocally.

As will also be discussed in the next section, the spin-orbit coupling is widely assumed to be the effect that ultimately causes spin-selective effects to occur in chiral molecules. However, one of the most puzzling aspects of the effect remains that films of biomolecules exhibit high degrees of spin filtering despite the low SOC of the

constituent carbon atoms. Some have argued the SOC in the substrate in combination with interface effects is instead at the heart of CISS, but this is contested by studies that indicate the relationship between substrate SOC and CISS to be limited.

1.2 CISS in Theory

1.2.1 Time Reversibility and Reciprocity Principles

To study spin-selectivity in two-terminal conductance experiments we will have to consider two important reciprocity principles, the Büttiker reciprocity and the Onsager-Casimir reciprocity. We will begin by discussing time-reversibility in quantum dynamics.

In absence of dissipation, the dynamics of a quantum system are governed by the system Hamiltonian following the time-dependent Schrödinger equation:

$$i\hbar \frac{\partial}{\partial t} |\psi(t)\rangle = \hat{\mathcal{H}} |\psi(t)\rangle. \tag{1.4}$$

Before we introduce the quantum mechanical time-reversal operator $\mathcal{T}$ let us consider the classical case. In classical mechanics, the motion of a particle moving through vacuum is time-reversible through the simple map $t \to -t$, $\mathbf{x} \to \mathbf{x}$, $\mathbf{p} \to -\mathbf{p}$, and consequently $\mathbf{L} \to -\mathbf{L}$. If the particle is charged and is moving through an external electromagnetic field $(\mathbf{E}, \mathbf{B})$ the time-reversal operator also maps $\mathbf{E} \to \mathbf{E}$, $\mathbf{B} \to -\mathbf{B}$. The reversal of the magnetic field is a consequence of the the momentum (motion) of the charge carriers generating the magnetic field reversing upon time-reversal. To summarize, in classical mechanics time-reversal is a map

$$t \to -t, \quad \mathbf{x} \to \mathbf{x}, \quad \mathbf{p} \to -\mathbf{p}, \quad \mathbf{L} \to -\mathbf{L}, \quad \mathbf{E} \to \mathbf{E}, \quad \mathbf{B} \to -\mathbf{B}. \tag{1.5}$$

In quantum mechanics, time reversal is a slightly trickier concept. For example, the canonical commutation relation $[\hat{x}, \hat{p}] = i\hbar$ is no longer satisfied if we use the classical time-reversal operation. If we exclude considerations regarding the electromagnetic field it is easily seen that, for spinless particles, the *complex conjugation operator* $\hat{\mathcal{K}}$ satisfies the requirements imposed on the time-reversal operator. So for the wavefunction of spinless particles $\hat{\mathcal{T}} = \hat{\mathcal{K}}$. Spin is another form of angular momentum and must therefore be reversed upon time-reversal, which for spin-1/2 fermions leads to a time-reversal operator $\hat{\mathcal{T}} = i\hat{\sigma}^y \hat{\mathcal{K}}$ with $\hat{\sigma}^y$ the second Pauli matrix.

The time operator $\hat{\mathcal{T}}$ commutes with the Hamiltonian,

$$[\hat{\mathcal{H}}, \hat{\mathcal{T}}] = 0, \tag{1.6}$$

which we can use to show that the Schrödinger equation is time-reversible. We apply $\hat{\mathcal{T}}$ to both sides of equation (1.4) and use the commutation relation (1.6) to rewrite it. We define $|\psi'\rangle \equiv \hat{\mathcal{T}} |\psi\rangle$ and obtain

$$\hat{\mathcal{T}}(i\hbar \frac{\partial}{\partial t} |\psi\rangle) = \hat{\mathcal{T}} \hat{\mathcal{H}} |\psi\rangle \Leftrightarrow i\hbar \frac{\partial}{\partial t} \hat{\mathcal{T}} |\psi\rangle = \hat{\mathcal{H}} \hat{\mathcal{T}} |\psi\rangle$$

$$\Leftrightarrow i\hbar \frac{\partial}{\partial t} |\psi'\rangle = \hat{\mathcal{H}} |\psi'\rangle.$$

We can therefore conclude that systems governed exclusively by the Schrödinger equation are time-reversible. It should be noted that $\hat{\mathcal{T}}$ is an anti-linear operator and hence $\hat{\mathcal{T}}$ and $\hat{\mathcal{H}}$ do not necessarily share eigenstates (which is the case for commuting *linear* operators) [10].

Having established the time-reversibility of systems without dissipation, let us now discuss time reversibility of driven quantum systems. In equation (1.3) we defined the magnetoresistance as

$$\text{MR} = \frac{I(m,V) - I(-m,V)}{I(m,V) + I(-m,V)} \equiv \frac{\Delta I(m,V)}{I(m,V) + I(-m,V)},$$

with $\Delta I(m,V)$ the magnetocurrent. We consider two thermally equilibrated leads connected to the molecule at either end. The current through the molecule is calculated using the Landauer formula [6]

$$I(m,V) = \frac{e}{h} \int_{-\infty}^{\infty} T_{RL}(m)(f_L(E) - f_R(E))dE, \tag{1.7}$$

in which $f_{L,R}(E)$ denote the Fermi-Dirac distribution of the left and right leads at energy E and T_{RL} is the transmission probability for an electron to travel from the right lead to the left lead, which can be calculated using the Meir-Wingreen formula [11]. In both leads we assume equal chemical potentials for spin up and down

electrons and symmetric capacitive coupling of the leads to the molecule, that is $\mu_L^i = E_F + \frac{V}{2}$ and $\mu_R^i = E_F - \frac{V}{2}$ for $i =\uparrow,\downarrow$. We expand the current in terms of the voltage as

$$I(m,V) = G_1(m)V + G_2(m)V^2 + ... \tag{1.8}$$

and use this to write the current asymmetry ΔI as

$$\Delta I(m,V) = I(m,V) - I(-m,V) = [G_1(m) - G_1(-m)]V + [G_2(m) - G_2(-m)]V^2 + ... \tag{1.9}$$

In 1988, Markus Büttiker demonstrated that the transmission probability through *non-interacting* systems coupled to two leads is invariant upon reversal of magnetisation, $T_{RL}(m) = T_{RL}(-m)$, as a consequence of time-reversal symmetry and charge conservation [12]. Equation (1.7) then implies a vanishing current asymmetry for non-interacting systems,

$$T_{RL}(m) = T_{RL}(-m) \Leftrightarrow I(m,V) = I(-m,V) \Leftrightarrow \Delta I(m,V) = 0, \tag{1.10}$$

and hence a vanishing magnetoresistance. This is known as the *Büttiker reciprocity principle*. It follows from equation (1.9) that $G_n(m) = G_n(-m)\,\forall n$ when Büttiker reciprocity holds. Conversely, this reciprocity principle implies that a finite magnetoresistance in a two-terminal system may only be found beyond the independent electron picture, where Büttiker reciprocity no longer holds. This can be done by explicitly considering many-body interactions or by modeling an effective interaction through generic dephasing probes (see for example [6]).

If we drop the non-interacting system requirement but now restrict ourselves to small bias voltages we still have to consider another reciprocity principle, the *Onsager-Casimir reciprocity*, which states that the current asymmetry vanishes *in the linear regime*. Specifically, the Onsager reciprocal relations tell us that transport is symmetric if it depends linearly on driving forces (i.e. bias voltage), as a consequence of time-reversal symmetry. The theory was extended to systems with an external magnetic field by Mazur and the Groot in 1953 [13], who showed that the reciprocal relations hold if the magnetic field is reversed upon time-reversal.

The Onsager relations demand a vanishing current asymmetry in the linear regime, $G_1(m) = G_1(-m)$. Substituting our expansion of $I(m,V)$ from equation (1.8) in the formula for the magnetoresistance (equation (1.3)) and recognising $G_1(m) - G_1(-m) = 0$ we obtain

$$\text{MR} = \frac{[G_2(m) - G_2(-m)]V + [G_3(m) - G_3(-m)]V^2 + ...}{G_1(m) + G_1(-m) + [G_2(m) + G_2(-m)]V + [G_3(m) + G_3(-m)]V^2 + ...}, \tag{1.11}$$

suggesting a vanishing magnetoresistance for zero bias voltage. Experimentally, the magnetocurrent has been observed to be an odd function of the bias voltage, implying the cubic term to be dominant. Consequently, the magnetoresistance is dominantly even in bias voltage.

In summary, the two reciprocity principles that are relevant for studying CISS are the Onsager and Büttiker reciprocity principles. Onsager reciprocity holds for both interacting and non-interacting systems, and states that the current asymmetry vanishes for small bias voltages. The Büttiker reciprocity only holds for non-interacting systems, for which it implies that no current asymmetry can be observed regardless of the strength of the driving.

1.2.2 Previous Theoretical Approaches in CISS Studies

The empirical evidence of the existence of chirality-induced spin filtering sparked an effort among scientists to rationalize the experimental results. Early theoretical works identified the spin-orbit coupling (SOC) as a likely cause of the CISS effect. However, while the SOC in chiral molecules *qualitatively* explains the existence of CISS, there is still a large *quantitative* discrepancy between experimental and theoretical results. Using realistic model parameters, theoretical estimates of the magnitude of spin filtering effects are typically orders of magnitude lower than experimentally measured values. Experimental values were only found for unrealistically high values of the SOC. Numerous studies have attempted to address this quantitative discrepancy, but as of yet no generally satisfactory explanation has been given. Even so, in the field there is a general consensus that the spin-orbit coupling in combination with the chiral molecular structure is a key ingredient for chirality induced spin selective phenomena.

Theoretical efforts on CISS can be broadly categorized in three groups: transport simulations with scattering models [14, 15, 16] or tight-binding models [17, 18, 19], or first principle calculations using density functional theory [20, 21, 22]. Early works studied the spin-selective properties of helical molecular structures with a Rashba-type spin-orbit interaction [14, 17, 18, 19]. These studies found the presence of at least two transport

channels and the presence of decoherence to be crucial prerequisites for spin-selective transport. A non-zero spin polarisation without the presence of dephasing effects was achieved in [19], but this required asymmetrical hopping parameters and spin-orbit coupling strengths.

Many of the earlier works, including the ones mentioned in the previous paragraph, considered only a single electron moving through the model and treated the SOC as a single term with an interaction strength controlled by a chosen parameter. Decoherence was introduced to the model through generic dephasing probes (Büttiker probes) that were coupled to each site. These type of studies are capable of qualitatively demonstrating the CISS effect, but are reliant on unrealistically large values for the SOC parameter to obtain experimental degrees of CISS [23].

One particularly interesting conjecture to address the quantitative deficit was put forward early on by Gersten et al. [24], who theorized the presence of an 'induced' spin filtering to explain the high degree of spin selectivity in photoemission experiments provided the presence of a strong SOC in the substrate. However, it has since been shown that the presented theory was insufficient as a general explanation for the high degrees of chirality induced spin filtering, since substantial CISS has also been observed in experimental photoemission setups using substrates with negligible SOC [25, 26].

Even so, this approach has recently garnered renewed interest [27, 28, 29, 30]. The method developed in references [28, 29] was able to reproduce the CISS effect at the same scale as experimentally observed, which was demonstrated by reproducing the data from the previously mentioned conduction experiment performed by Xie et al. [5]. In this approach, the magnitude of the effect is explained by a positive feedback loop, see [28]. In short, at the interface between the electrode and molecule the spin-orbit interaction of the electrons in the electrode is framed as an effective magnetic moment, resulting from the electron orbitals, that interacts with the electron spin. The theory suggests that, initially, the orientation of the effective magnetisation is random. Upon applying a bias voltage, an unpolarised current will pass through the chiral molecule. This current generates a solenoid magnetic field that interacts with the magnetic moment of the electrons at the interface, causing an energy splitting in the electrochemical potentials of up and down electrons (a Zeeman splitting). Consequently, the current passing through the molecule will become slightly spin-polarised (the orientation dictated by molecule handedness). The spin-current acts as an additional effective magnetic field through the *spin-transfer torque effect* [31] which adds to the force exerted on the magnetic moment in the interface, causing further splitting of the energy levels and further increasing the spin current. To clarify, in this mechanism the effective magnetic field generated by the current through the chiral molecule polarizes the orbital angular momentum of the electrons in the electrode, which causes spin-selective transmission through the electrode-molecule interface and results in an eventual steady-state spin current through the molecule. The authors relate this to a magnetoresistance in the junction by noting that electrons polarised anti-parallel to the ferromagnetic Ni-electrode experience a higher resistance passing into the electrode than electrons polarised parallel with the magnetisation of the electrode. In other words, the spin-polarised currents caused by the interface effects experience different effective resistances when passing through the junction, giving rise to the CISS effect.

Naturally, the strength of the spin-orbit coupling effect dictates the magnitude of the effective magnetic moment and hence the Zeeman splitting, implying the effect should be significantly reduced for substrates with low SOC such as Ag or Al. On the contrary, CISS has been observed experimentally using substrates of these materials. The author of [29] argues a lower SOC in the substrate can be offset by increasing the parameter of the spin-transfer torque. This claim is not motivated any further.

Recent experimental work of Adhikari and coworkers [32] investigated the dependence between substrate SOC and the magnitude of the CISS effect. The results clearly demonstrated that a substrate with stronger spin-orbit interaction (Au compared to Al) exhibits a greater spin-bias in the conductance. This study also provided further evidence on the length-dependence of the CISS effect, the fact that longer molecules exhibit stronger spin-filtering. In [29] the dependence between molecule length and CISS is explained as a consequence of length-dependency of the molecule's spin-polarizability and transport properties, and not because spin-selectivity of the conduction is an extensive property of chiral molecules.

A point which the interface approach fails to address is the fact that photoemission experiments using helicenes [26] did not display any significant relation between substrate SOC and the spin-polarisation of the transmission. Specifically, the experiment concerns photoelectrons ejected from substrates of Cu(332), Ag(110) and Au(111) passing through a layer of (enantiopure) helicene. Despite the varying SOC strengths in the substrates, the spin-polarisation of the transmission was measured to be around 8% in all cases. In conclusion, interface considerations may be an important part of a comprehensive theory of CISS but are not sufficient to explain the entire effect.

Some researchers have suggested the disregard for many-body effects between electrons, such as the Coulomb interaction, or the application of the Born-Oppenheimer approximation are the cause of the low reported

values of spin-polarisation in the early theoretical models, directing theoretical efforts beyond the single-electron picture. Fransson [33] investigated a model of interacting electrons, implementing the spin-orbit interaction through the use of a Kane-Mele model, adapted for chiral structures. The electrons interacted with each other through an on-site Coulomb potential with interaction strength comparable to the nearest-neighbour hopping terms. Non-local Coulomb interactions were assumed to be negligible as a consequence of electric field screening. An increase in spin polarisation was demonstrated of up to 2 orders of magnitude compared to a system without electron-electron interactions, for short chains. However, using realistic model parameters the calculated magnitude of the CISS effect remained orders of magnitude below experimental values [34]. Other studies allowed a coupling between the travelling electrons and the vibrations in the molecular lattice (electron-phonon coupling), both by considering electrons and phonons separately [35, 36] or together, as a travelling polaron [37, 38]. These works investigate the possibility of a vibrationally-assisted increase of the effective SOC and have demonstrated significant enhancements in the magnitude of spin-selectivity of the current.

Although it has been shown that inclusion of electron correlations or molecule vibrations can reduce the quantitative discrepancy to some extent, all aforementioned studies are still unable to fully reproduce experimental degrees of CISS with realistic values for the SOC.

The quantitative discrepancy in the degree of spin-filtering between theory and experiment has been studied extensively and is well documented as a result. However, theoretical works have also reported qualitative behaviour that differs from experimentally observed characteristics. Specifically, in section 1.1 it was stated that the magnetocurrent has been measured to be dominantly odd in bias voltage. Consequently, the magnetoresistance is dominantly even. This is a result that multiple theoretical calculations have failed to reproduce, for example the studies by Yang et al. [39], Huisman [6] and Fransson [40].

A study performed by Huisman et al. [41] specifically addressed this matter, reporting the $\Delta I/V$ characteristics of transport calculations in different parameter regimes. The work concerns transport calculations of a single-stranded helical molecule described by a tight-binding Hamiltonian. The model, originally proposed by Fransson [33], includes local Coulomb interactions and next-nearest neighbour spin-orbit interactions, and is also the model of focus in this thesis. The specific Hamiltonian will be treated in more detail in the next section. Huisman and coworkers calculated the current through the molecule using the nonequilibrium Green's function formalism through the Hubbard One and Hartree-Fock approximations. The study found expected behaviour of the magnetocurrent for most cases, except for the case of weak Coulomb interactions and asymmetric chemical potential in the driving leads, where an even magnetocurrent characteristic was reported in the Hartree-Fock approximation. However, despite (mostly) recovering expected qualitative behaviour, the magnitude of the magnetoresistance remained far below experimental values, with reported values of less than 1% for strong spin-orbit coupling.

The formulation of a comprehensive theory of spin-selective effects of chiral molecules remains an open matter. The efforts of many scientists have brought numerous mechanisms into focus which may play a part in this complex effect. The field of CISS in condensed matter physics and quantum chemistry is growing fast, and even though there is no complete theoretical framework, the CISS effect is being applied in various areas of technology. The CISS effect allows for efficient generation of spin currents using organic filters of molecular scale that can be applied in the field of spintronics [42]. It has also been demonstrated that CISS-based spin-filters can be leveraged in electrochemistry, for example to increase the efficiency of splitting water into hydrogen and oxygen [43], as well as in other applications [9]. It has even been linked to homochirality in nature and the origin of life [44]. These topics, while interesting, are beyond the scope of this thesis.

1.3   The Purpose of this Thesis

1.3.1   Method

In this work we will apply the matrix product states framework to simulate electron transport through a chiral molecule described with a tight-binding Hamiltonian. In our model we will include electron-electron interactions in the form of the Coulomb interaction and a next-nearest neighbour spin-orbit coupling that is inspired by the Kane-Mele model and was first put forward by Fransson [33] and has also been studied in [11]. References [11, 33] both calculate the electron transport through this model using the nonequilibrium Green's function (NEGF) method, and simplify the Hamiltonian using the Hartree-Fock ([11]) and Hubbard One ([11, 33]) approximations. The matrix product states formalism allows us to efficiently describe states which are locally entangled. By design, the matrix product state decomposition writes the state vector in such that the application of local actions does not scale with the system size. In combination with the Suzuki-Trotter decomposition this allows for an efficient time-evolution algorithm called time-evolving block decimation. The specifics of matrix product states will be discussed in section 3.

The one-dimensional system will be coupled to Markovian baths at both ends, causing a nonequilibrium situation. The actions of these couplings will be formulated using the Lindblad equation. Consequently, we will describe our system using the extension of matrix product states to density matrices: the matrix product density operator formalism.

Combining matrix product density operators and time-evolving block decimation allows us to calculate time evolution without requiring any systematic approximations to be made on the Hamiltonian, as opposed to the approaches mentioned above. Instead, this approach is restricted in the class of states that can be efficiently described using matrix product states: states which are only lightly entangled. As it turns out, the MPS ansatz for solving nonequilibrium steady states can be justified in many cases, as they tend to be lightly entangled even for strong interactions [45, 46]. In other words, even though the Hamiltonian dynamics of the system would be unsuitable for matrix product states-based time evolution methods, the inclusion of dissipation at the boundary will cause the system to converge to a state which *can* be effectively described using matrix product states.

The aim of this thesis is primarily to investigate the viability of the matrix product states ansatz for solving tight-binding models in the context of spin-selective transport, and whether matrix product states can be used as a tool for studying the influence of different system parameters on the overall effect. To this end, emphasis will be placed on investigating whether the tensor-network approach reproduces theoretically expected behaviour in the linear and non-interacting regimes, and whether the model reproduces the expected characteristics of CISS on a qualitative level. The model that will be used in this study has been studied previously in different approaches, which all concluded that it exhibited low degrees of CISS in realistic parameter regimes. It is therefore not expected that this study will recover experimental degrees of spin-selective transport.

1.3.2 The Spin-Orbit Interaction and Model Hamiltonian

A mentioned in the previous section, the spin-orbit coupling is widely believed to be the root cause of the CISS effect. The spin-orbit coupling is a relativistic effect that can be derived from the Dirac equation. As the name implies, the spin-orbit coupling refers to an interaction between an electron's spin and its orbital angular momentum that causes an energy splitting. Simply put, the spin-orbit coupling (SOC), or spin-orbit interaction (SOI), is the coupling between the electron's spin magnetic moment and the magnetic field it experiences as it moves through the electric field of the nucleus. In mathematical terms the spin-orbit interaction is written as follows:

$$\hat{H}_{SO} = \frac{e\hbar}{4m^2c^2}\boldsymbol{\sigma} \cdot (\boldsymbol{E} \times \boldsymbol{p}), \tag{1.12}$$

with e the elementary charge, m the electron mass, $\boldsymbol{\sigma}$ the vector of Pauli matrices and $\boldsymbol{p}$ the momentum of the electron. This equation holds for any electrostatic field $\mathbf{E}$ in the nonrelativistic limit [47]. The illustration in the paragraph above is an example of the atomic spin-orbit coupling, but the SOC can also be present in solid state systems as a consequence of, for example, lattice impurities or asymmetric lattice potentials [48]. An important example of the latter is the Rashba SOC, which is present in helical molecules. In helical structures of positively charged nuclei the electrostatic potential displays a helical symmetry. An electron moving along the axial direction through this helix will experience an energy splitting dependent on whether its spin is aligned parallel or anti-parallel to the helical axis. As mentioned, the Rashba SOC has been used as a basis in a number of theoretical studies in CISS [14, 17, 18, 47], which were all unable to reproduce experimental values of CISS for realistic SOC parameters.

In 2019, Fransson [33] performed a study on CISS using a tight-binding model with a spin-orbit interaction between next-nearest neighbours inspired by the quantum spin Hall effect (QSE). The Hamiltonian used in this work a generalization of the model introduced by Kane and Mele [49], which was in turn derived from the Haldane model [50]. The Haldane model is a quantum Hall effect (QHE) model which considers the hexagonal unit cell of graphene through which a magnetic field flows such that the total magnetic flux through the unit cell is 0. In this case, the vector potential $\mathbf{A}$ on the boundary of the hexagon must be 0, but is not necessarily zero in the enclosed area. Haldane studied the movement of electrons around the six sites of such a unit cell. Electrons moving along a curve C through a magnetic vector potential acquire a phase factor $\exp\left(\frac{\mathrm{i}e}{\hbar}\int_C \mathbf{A} \cdot d\mathbf{r}\right)$. In the case of graphene, electrons hopping between nearest neighbours move along a path where the vector potential is zero (the boundary), but those hopping between next-nearest neighbours will pass through an area with a finite vector potential and will therefore acquire a phase. Inclusion of electron spin to this model without any other alterations gave rise to an additional Zeeman term due to coupling with the magnetic field. Kane and Mele used the Haldane model as a basis to demonstrate the quantum spin Hall effect. The Kane-Mele model is a double Haldane model for spin-1/2 electrons in graphene, that does not assume the presence of external magnetic fields but instead includes a spin-orbit interaction between next-nearest neighbouring sites, which

gives rise to the QSE. Specifically, the tight-binding spin-orbit term used in the Kane-Mele model is given by

$$\hat{H}_{\mathrm{SO}} = \mathrm{i}\lambda \sum_{\langle\langle ij \rangle\rangle} \sum_{ss'} \hat{c}_{is}^{\dagger} v_{ij} \hat{\sigma}_{ss'}^{z} \hat{c}_{js'}, \tag{1.13}$$

where the parameter $v_{ij} = +1\,(-1)$ if the electron moves (counter)clockwise, $\hat{\sigma}^z$ is the third Pauli matrix and $\sum_{\langle\langle ij \rangle\rangle}$ denotes a sum over all next-nearest neighbour pairs. The parameter λ is the interaction strength.

Fransson adapted the Kane-Mele spin-orbit term to be applicable to three-dimensional helical models, although it can be applied to arbitrary geometrical structures. Fransson's spin-orbit interaction is given by

$$\hat{H}_{\mathrm{SO}} = \lambda \sum_{i} \sum_{ss'} \left(\mathrm{i}\, \hat{c}_{is}^{\dagger} (\mathbf{v}_i \cdot \boldsymbol{\sigma})_{ss'} \hat{c}_{i+2s'} + \mathrm{H.c.} \right), \tag{1.14}$$

where the vector $\boldsymbol{\sigma}$ is the vector of Pauli matrices and the variable v_{ij} has been replaced by a vector $\mathbf{v}_i$ that captures the system geometry between sites i and $i+2$. The vector is defined as the outer product between the normalised vectors connecting sites $i, i+1$ and $i+1, i+2$, $\mathbf{v}_i = \mathbf{d}_{i,i+1} \times \mathbf{d}_{i+1,i+2}$. The geometrical significance of the vectors $\mathbf{v}_i$ is shown in figure 1.3a.

The Hamiltonian proposed by Fransson allows for spin-symmetry breaking for systems of 4 or more lattice sites. Specifically, for a system with 3 lattice sites the spin-orbit interactions necessarily involve parallel geometrical paths and the contributions are therefore equivalent and opposite. However, a system of 4 or more sites allows for scattering paths involving non-parallel vectors $\mathbf{v}$, meaning these contributions do not necessarily vanish. The relevant scattering paths in the case of a system of 4 sites are presented in figure 1.3. Consequently, we only expect spin-dependent effects to occur for systems comprised of 4 or more sites.

| (a) | (b) |
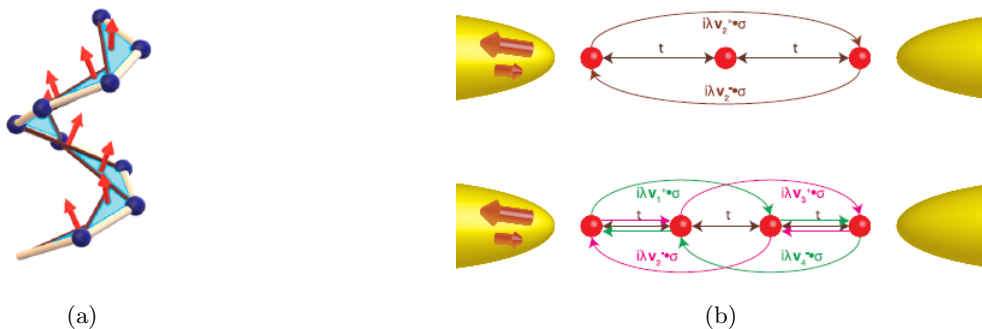
Figure 1.3: (a) Geometrical significance of the vectors $\mathbf{v}$, shown in red, in the spin-orbit Hamiltonian as depicted by Heinisch in [11]. (b) The illustration by Fransson [33] indicating the electron paths in which spin-orbit contributions are non-vanishing (lower half), which are not present for a chain of $L = 3$ sites (upper half).

We add the spin-orbit Hamiltonian of equation (1.14) to the Hamiltonian of the standard Hubbard model with on-site Coulomb interactions, resulting in the complete Hamiltonian:

$$\hat{H} = -t \sum_{j=1}^{L-1} \sum_{s} (\hat{c}_{j,s}^{\dagger} \hat{c}_{j+1,s} + \mathrm{H.c.}) + \sum_{j=1}^{L} U \hat{n}_{j,\uparrow} \hat{n}_{j,\downarrow} + \lambda \sum_{j=1}^{L-2} \sum_{ss'} \left(\mathrm{i}\, \hat{c}_{j,s}^{\dagger} (\mathbf{v}_j \cdot \boldsymbol{\sigma})_{ss'} \hat{c}_{j+2,s'} + \mathrm{H.c.} \right). \tag{1.15}$$

The length of our molecule is defined as L. In transport setups, the chiral molecule is connected to electrodes at either end, after which a voltage difference is applied to induce a current through the molecule. Traditionally, one of these electrodes is ferromagnetic and magnetised in order to split the density of states of the electrons depending on its spin, illustrated in figure 1.2. The coupling of the molecule to the electron baths is modeled with a Lindblad equation, which will be addressed in section 2.1. The nonequilibrium situation and magnetisation of the induced current is controlled through the bath-model coupling strengths. In total, 8 Lindblad operators will act on the system (4 at either end of the chain) which are given by

$$\begin{aligned} \hat{L}_1 &= \sqrt{\gamma_{\uparrow}(1+\nu)}\hat{c}_{1\uparrow}^{\dagger} & \hat{L}_2 &= \sqrt{\gamma_{\uparrow}(1-\nu)}\hat{c}_{1\uparrow} & \hat{L}_3 &= \sqrt{\gamma_{\downarrow}(1+\nu)}\hat{c}_{1\downarrow}^{\dagger} & \hat{L}_4 &= \sqrt{\gamma_{\downarrow}(1-\nu)}\hat{c}_{1\downarrow} \\ \hat{L}_5 &= \sqrt{\gamma(1-\nu)}\hat{c}_{L\uparrow}^{\dagger} & \hat{L}_6 &= \sqrt{\gamma(1+\nu)}\hat{c}_{L\uparrow} & \hat{L}_7 &= \sqrt{\gamma(1-\nu)}\hat{c}_{L\downarrow}^{\dagger} & \hat{L}_8 &= \sqrt{\gamma(1+\nu)}\hat{c}_{L\downarrow}. \end{aligned} \tag{1.16}$$

The parameter ν characterises the occupation levels in the baths, while the parameters $\gamma_{\uparrow}$, $\gamma_{\downarrow}$ control the magnetisation of the left bath.

2 Transport in 1D Systems

2.1 Open Quantum Systems

All quantum mechanical systems can be divided in two groups, *open systems* and *closed systems*. A system is called open when it interacts with an external system, often called an *environment* or *bath*. Conversely, a system is open if it is not closed. The state of a closed quantum system can be completely described by a state vector $|\psi\rangle$ in the Hilbert space of the system, $|\psi\rangle \in \mathcal{H}_S$. The dynamics of a closed quantum system is described deterministically by the famous Schrödinger equation. In general, open quantum systems cannot be described by state vectors because interactions between the system and the environment cause them to become *entangled*. If a system is entangled with an environment, no single vector in the system Hilbert space can adequately describe the state of the system. Instead, we must make use of a *density matrix* or *density operator* to describe the state of our system. Moreover, the Schrödinger equation is insufficient to describe the time-evolution of open quantum systems as they often evolve in a non-unitary fashion. Therefore the dynamics of open quantum systems are instead governed by a *master equation*. In this section we will summarize the fundamentals of open quantum systems and consider a specific master equation, the Lindblad master equation.

Consider a system governed by a Hamiltonian $\hat{H}$ with eigenstates $|\psi_i\rangle$ which form an orthonormal basis for the system Hilbert space $\mathcal{H}_S$. The density matrix describing the system is given by

$$\rho = \sum_{ij} p_{ij} |\psi_i\rangle \langle\psi_j| . \tag{2.1}$$

The coefficients p_{ii} are the probability amplitudes of finding the system in state $|\psi_i\rangle$ and therefore add up to 1, yielding the normalisation condition $\text{Tr}(\rho) = 1$, with $\text{Tr}()$ denoting the trace. The density matrices describing physical systems are always Hermitian and positive semi-definite. Moreover, the density matrix of a pure state has the property that it is idempotent, $\rho^2 = \rho$, and hence has purity 1, $\text{Tr}(\rho^2) = 1$. Density matrices with purity less than 1, $\text{Tr}(\rho) < 1$ describe systems which are entangled with an environment, which are referred to as *mixed states*. Mixed states can only be described by density matrices. Let us therefore state the analogue of the Schrödinger equation for density matrices, the *Liouville-Von Neumann equation*:

$$\frac{d}{dt}\rho(t) = -\frac{\mathrm{i}}{\hbar}[\hat{H}(t), \rho(t)], \tag{2.2}$$

which describes the time evolution of closed systems. The Liouville-von Neumman equation can also be written as

$$\frac{d}{dt}\rho(t) = \hat{\mathcal{L}}(t)\rho(t), \tag{2.3}$$

where $\hat{\mathcal{L}}(t)$ is the *Liouville superoperator* that is defined through the condition that the action of $\hat{\mathcal{L}}(t)$ on $\rho(t)$ is equal to $-\frac{\mathrm{i}}{\hbar}[\hat{H}(t), \rho(t)]$. $\hat{\mathcal{L}}$ is called a superoperator since it maps operators to operators [51].

In general, the solution to the Liouville-von Neuman equation for closed systems is of the form $\rho(t) = \hat{U}(t)\rho(0)\hat{U}^\dagger(t)$ with $\hat{U}(t)$ a unitary operator. For time-independent Hamiltonians we have $\hat{U}(t) = \exp(-\mathrm{i}\hat{H}t/\hbar)$. Even though this equation describes the time-evolution of an operator, this equation assumes the Schrödinger picture, as a time-evolved density matrix is the product of time-evolved state vectors: $\rho(t) = \hat{U}(t)|\psi(0)\rangle\langle\psi(0)|\hat{U}^\dagger(t) = |\psi(t)\rangle\langle\psi(t)|$. As mentioned, the time-evolution operator $U(t)$ is unitary and therefore describes coherent time-evolution.

Let us now discuss the dynamics of open quantum systems. As before, we start with a total system or 'universe' U comprised of system S and environment E, with respective Hilbert spaces $\mathcal{H}_U$, $\mathcal{H}_S$ and $\mathcal{H}_E$. The universe is governed by a Hamiltonian $\hat{H}_U = \hat{H}_S + \hat{H}_E + \hat{H}_{SE}$ with $\hat{H}_S$, $\hat{H}_E$ the Hamiltonians of the system and environment and $\hat{H}_{SE}$ the interaction Hamiltonian. The time-evolution of the universe is unitary following the Liouville-von Neumann equation ((2.2)). Therefore, we know the state of system S at any given time to be

$$\rho_S(t) = \text{Tr}_E\big(\hat{U}(t)\rho_U(0)\hat{U}^\dagger(t)\big). \tag{2.4}$$

This is method of calculating the time-evolution of S is completely valid but in general not practical, as $\mathcal{H}_E$ often is too large to describe. The preferred method of calculating time-evolution is to find a *dynamical map* $\rho_S(0) \to \rho_S(t)$ that is completely characterised by operators acting on system S. Finding closed-form expressions of such a map is only possible for simple systems. Usually, the dynamics are given in the form of a differential equation for the density matrix, also called a master equation. In this research we make use of the Gorini-Kossakowski-Sudarshan-Lindblad (GKSL) master equation (also called the *Lindblad master equation*), which is the most general form of a *Markovian* quantum master equation [51]. A short derivation of this master equation

is provided in appendix A, the full derivation and proof can be found in chapter 3 of the book by Breuer and Petruccione [51].

Following the steps outlined in appendix A we eventually arrive at the Lindblad equation (2.5), which resembles the Von Neumann equation (2.2) with additional dissipative terms. The dissipative terms are sometimes grouped together and abbreviated as the *dissipation superoperator* $\hat{\mathcal{D}}$, equation (2.6),

$$\hat{\mathcal{L}}\rho_S = -\frac{i}{\hbar}[\hat{H}, \rho_S] + \hat{\mathcal{D}}(\rho_S), \tag{2.5}$$

$$\hat{\mathcal{D}}(\rho_S) = \sum_k \gamma_k \big(\hat{L}_k \rho_S \hat{L}_k^\dagger - \frac{1}{2}\{\hat{L}_k^\dagger \hat{L}_k, \rho_S\}\big). \tag{2.6}$$

It is important to note that we have incorporated the coupling strengths γ_k in the definitions of the Lindblad operators $\hat{L}_k$ in equation (1.16).

2.2 The Hubbard Model

As discussed in section 1.3.2, we will make use of the Hubbard Hamiltonian to describe our three-dimensional helical molecule. The Hubbard model was originally introduced in the 1960s to describe interacting electrons in solids. It is a highly simplified model which assumes atomic sites only have one orbital, which can be occupied by up to two electrons due to spin degeneracy. Thus, each site has a local Hilbert space of dimension 4, with basis states $\{|0\rangle, |\uparrow\rangle, |\downarrow\rangle, |\uparrow\downarrow\rangle\}$. The basic Hubbard model contains two terms which describe the movement of and interactions between electrons. Electrons can move between sites which are spatially close together through a non-zero hopping term. The electrons interact through local Coulomb interactions, meaning interactions between electrons located on different sites in the model are assumed to be negligible. The Hubbard model assumes the atoms located at each site to be static relative to the electrons as a consequence of their much higher mass. This allows us to separate their wavefunctions and therefore neglect the nuclear degrees of freedom (the Born-Oppenheimer approximation). The Hubbard Hamiltonian thus takes the form

$$\hat{H} = -\sum_{i,j}\sum_s t_{ij}\hat{c}_{i,s}^\dagger \hat{c}_{j,s} + U\sum_i \hat{n}_{i,\uparrow}\hat{n}_{i,\downarrow}. \tag{2.7}$$

with $t_{ij} = t_{ji}^*$ since the Hamiltonian is Hermitian.

In spite of the fact that our system is defined in three-dimensional space, it can be modeled by a one-dimensional Hubbard model, because the order of the lattice sites in the molecule is defined up to the choice of a starting point, allowing us to number the sites with a single parameter i. In our system, we assume the hopping terms are only nonzero between nearest-neighbours.

The Hubbard model is symmetric for particle-hole transformations. That is, if we redefine the absence of an electron as the presence of a hole, with opposite charge and identical spin, the Hamiltonian remains invariant up to a sign change of t and a shift in energy. In mathematical terms this corresponds to replacing $\hat{c}_{i,s_i} \leftrightarrow (-1)^i \hat{d}_{i,s_i}^\dagger$ and $\hat{c}_{i,s_i}^\dagger \leftrightarrow (-1)^i \hat{d}_{i,s_i}$, where $\hat{d}$ denotes the hole annihilation operator. Because of the particle-hole symmetry one only needs to consider cases up to half band-filling when studying the Hubbard Hamiltonian.

Let us briefly discuss the behaviour of the Hubbard model for different parameter limits. For a vanishing U the Hubbard model describes a free Fermi-gas, whereas for a vanishing t the Hubbard Hamiltonian is diagonal in physical space and the system (obviously) describes amore tricky. If we consider $U \to \infty$ and half band-filling the system is insulating for all $U > 0$, since any electron excitations will have a finite energy gap. Thus, we can infer that there is a metal-insulator transition at $U_c = 0^+$ for half-filled systems. For less-than-half band-filling the system will also be conducting, as there exist gapless electron excitations for all U. The system is gapless for spin excitations in both cases. In the situations that will be simulated in this thesis, we will either take vanishing U or U comparable to t. For a vanishing U the electrons in the system are non-interacting and we will therefore expect the dynamics to adhere to the Büttiker reciprocity principle discussed in section 1.2.1.

In this work we are specifically interested in the (steady state) current through the Hubbard model, which we will obtain by examining the Heisenberg equation of motion of the number operator $\hat{n}_{i,s}$. To make this derivation applicable to the Hamiltonian of equation (1.15) we will write the Hamiltonian as

$$\hat{H} = \sum_{i,j}\big(J_{ij}\hat{c}_i^\dagger \hat{c}_j + \text{H.c.}\big) + U\sum_{i \text{ even}} \hat{n}_i\hat{n}_{i+1}. \tag{2.8}$$

This expression generalises equation (1.15) by mapping $(i,\uparrow) \to 2i$, $(i,\downarrow) \to 2i+1$ and by grouping the hopping and spin-orbit terms with a generalized parameter J_{ij}.

Now, the Heisenberg equation of motion for the occupation of site i, provided there is no dissipative action on this site, is given by

$$\frac{d\hat{n}_i}{dt} = i[\hat{H}, \hat{n}_i]. \tag{2.9}$$

Let us also state the fermionic anticommutation relations:

$$\{\hat{c}_i^\dagger, \hat{c}_j\} = \delta_{ij} \tag{2.10}$$

$$\{\hat{c}_i^\dagger, \hat{c}_j^\dagger\} = \{\hat{c}_i, \hat{c}_j\} = 0. \tag{2.11}$$

From these relations it follows that the number operator commutes with fermionic creation/annihilation operators that act on different sites and hence it follows that number operators for different sites also commute. We can therefore disregard any terms in equation (2.8) that do not involve site i and we may also disregard the Coulomb interaction terms.

We are left with

$$\frac{d\hat{n}_i}{dt} = i\sum_j [J_{ij}\hat{c}_i^\dagger \hat{c}_j + J_{ji}^*\hat{c}_j^\dagger \hat{c}_i, \ \hat{n}_i] = i\sum_j \left(J_{ij}[\hat{c}_i^\dagger \hat{c}_j, \hat{n}_i] + J_{ji}^*[\hat{c}_j^\dagger \hat{c}_i, \hat{n}_i]\right)$$

$$= i\sum_j \left(J_{ij}(\hat{c}_i^\dagger \hat{c}_j \hat{n}_i - \hat{n}_i \hat{c}_i^\dagger \hat{c}_j) + J_{ji}^*(\hat{c}_j^\dagger \hat{c}_i \hat{n}_i - \hat{n}_i \hat{c}_j^\dagger \hat{c}_i)\right)$$

$$= i\sum_j \left(J_{ij}(\hat{c}_i^\dagger \hat{n}_i - \hat{n}_i \hat{c}_i^\dagger)\hat{c}_j + J_{ji}^*\hat{c}_j^\dagger(\hat{c}_i \hat{n}_i - \hat{n}_i \hat{c}_i)\right)$$

From the fermionic anticommutation relations it can be inferred that

$$[\hat{c}_i^\dagger, \hat{n}_i] = -\hat{c}_i^\dagger, \qquad [\hat{c}_i, \hat{n}_i] = \hat{c}_i, \tag{2.12}$$

substituting these relations gets us the general expression for the change in occupation of site i,

$$\frac{d\hat{n}_i}{dt} = i\sum_j \left(-J_{ij}\hat{c}_i^\dagger \hat{c}_j + J_{ji}^*\hat{c}_j^\dagger \hat{c}_i\right). \tag{2.13}$$

We can identify the terms on the right hand side of this equation as currents flowing from site j to site i and vice versa. Using equation 2.13 we can define the operator for the total current through a bond in the system, $\hat{J}_k$, where k labels the bond index. We define the current through a bond as the sum of all currents across this bond,

$$\hat{J}_k = i\sum_{i>k}\sum_{j\leq k} \left(-J_{ij}\hat{c}_i^\dagger \hat{c}_j + J_{ji}^*\hat{c}_j^\dagger \hat{c}_i\right). \tag{2.14}$$

Using equations (2.13) and (2.14) and the fact that the number of particles must be conserved for non-dissipative dynamics, we can formulate the continuity equation for the current between bonds k and l:

$$\hat{J}_k - \hat{J}_l = \sum_{k<i\leq l} \frac{d\hat{n}_i}{dt}. \tag{2.15}$$

It should be noted that expression (2.13) is valid only for sites on which there is no dissipative action. Intuitively, only if a site is coupled to a source or drain we must take into account the current into this source or drain. The general form of equation (2.9), predictably, includes the dissipative part of the Lindblad equation and is given as [52]

$$\frac{d\hat{n}_i}{dt} = i[\hat{H}, \hat{n}_i] + \text{Tr}(\hat{n}_i \hat{\mathcal{D}}(\rho_S)). \tag{2.16}$$

An analytical analysis of this equation is found in appendix A. This yields the expected result that the dissipative term can be disregarded for sites to which no Lindblad operators are coupled. For a site i that is coupled with a strength γ_S to a source and γ_D to a drain, the total current is given by

$$\frac{d\hat{n}_i}{dt} = i\sum_j \left(-J_{ij}\hat{c}_i^\dagger \hat{c}_j + J_{ji}^*\hat{c}_j^\dagger \hat{c}_i\right) + \gamma_S\langle 1 - \hat{n}_i\rangle - \gamma_D\langle \hat{n}_i\rangle. \tag{2.17}$$

In this work, we exclusively work with Lindblad operators that act on a single physical site. Therefore, the additional terms in (2.17) do not change expression (2.14), since it concerns current across bonds. Moreover, if no dissipative action is present on any site between sites k and l, the continuity equation (2.15) remains true as well.

2.3 The Jordan-Wigner Transformation

In this work we will make use of the matrix products states formalism to simulate electron transport through molecules described by a Hubbard Hamiltonian. Matrix product states were originally developed for the investigation of spin systems, and much work on MPS has been in this context. It is possible to simulate particle systems such as the Hubbard model directly with matrix product states [53]. However, in the case of fermionic systems it is possible to relate the particle system to an equivalent spin system through the Jordan-Wigner transformation, which can be simulated using conventional matrix product states methods. This approach was taken for simulating the Hubbard model by Prosen and Žnidarič in 2012 [54] and will also be taken in this thesis. The Jordan-Wigner transformation, developed by Pascual Jordan and Eugene Wigner, is a transformation that maps spin operators to fermionic creation/annihilation operators. However, the transformation is easily inverted to allow us to map the Hubbard Hamiltonian of equation (2.7) to a spin-ladder system.

We will first address the transformation from a spin system to a particle system. Consider a 1D system of N ordered spins that can be in the up ($|\uparrow\rangle$) or down ($|\downarrow\rangle$) states, which are eigenstates of the third Pauli matrix. The Pauli matrices are defined as

$$\hat{\sigma}^x \equiv \begin{bmatrix} 0 & 1 \\ 1 & 0 \end{bmatrix} \qquad \hat{\sigma}^y_j \equiv \begin{bmatrix} 0 & -\mathrm{i} \\ \mathrm{i} & 0 \end{bmatrix} \qquad \hat{\sigma}^z \equiv \begin{bmatrix} 1 & 0 \\ 0 & -1 \end{bmatrix}, \tag{2.18}$$

Additionally, we define the raising and lowering operators as

$$\hat{\sigma}^+_j \equiv \begin{bmatrix} 0 & 1 \\ 0 & 0 \end{bmatrix} = \frac{\hat{\sigma}^x_j + \mathrm{i}\hat{\sigma}^y_j}{2} \qquad \hat{\sigma}^-_j \equiv \begin{bmatrix} 0 & 0 \\ 1 & 0 \end{bmatrix} = \frac{\hat{\sigma}^x_j - \mathrm{i}\hat{\sigma}^y_j}{2}, \tag{2.19}$$

that map an up-spin to a down-spin and vice versa.

The Pauli operators satisfy (anti-)commutations relations ($\alpha, \beta, \gamma \in \{x, y, z\}$)

$$[\hat{\sigma}^\alpha_j, \hat{\sigma}^\beta_j] = 2\mathrm{i}\hat{\sigma}^\gamma_j \, \epsilon_{\alpha\beta\gamma}, \tag{2.20}$$

$$\{\hat{\sigma}^+_j, \hat{\sigma}^-_j\} = 1. \tag{2.21}$$

The $\epsilon_{\alpha\beta\gamma}$ in equation (2.20) is the Levi-Civita symbol. Pauli operators on different sites commute.

We map each qubit to a particle state that can either be empty or hold a single particle, which we associate with the 'down' and 'up' states respectively ($|0\rangle \leftrightarrow |\downarrow\rangle$, $|1\rangle \leftrightarrow |\uparrow\rangle$). Seeing as each qubit can only be in two states, it would seem intuitive to map our qubit to fermions as the single-particle limit per site is enforced by the Pauli exclusion principle. Now, we could naively try to relate the spin operators and the fermionic creation-annihilation operators by

$$\begin{aligned} \hat{\sigma}^+_j &\leftrightarrow \hat{c}^\dagger_j \\ \hat{\sigma}^-_j &\leftrightarrow \hat{c}_j \\ \hat{\sigma}^z_j &\leftrightarrow 2\hat{n}_j - 1, \end{aligned} \qquad\qquad \begin{aligned} \hat{\sigma}^x_j &\leftrightarrow \hat{c}_j + \hat{c}^\dagger_j \\ \hat{\sigma}^y_j &\leftrightarrow \mathrm{i}(\hat{c}_j - \hat{c}^\dagger_j) \end{aligned} \tag{2.22}$$

with $\hat{n}_j \equiv \hat{c}^\dagger_j \hat{c}_j$.

In equation (2.22) we have disregarded the fact that independent spin-raising and spin-lowering operators commute, whereas independent fermionic operators anti-commute. To reconcile this and come to a well-defined transformation we must include these minus signs in equation (2.22). Here we also make use of the crucial point that our spins are ordered, which allows for a natural handling of the minus signs that emerge in the fermionic system upon exchanging indices. This brings us to the map between spin operators and fermionic operators:

$$\begin{aligned} \hat{\sigma}^+_j &\leftrightarrow e^{+\mathrm{i}\pi \sum_{k=1}^{j-1} \hat{n}_k} \hat{c}^\dagger_j \\ \hat{\sigma}^-_j &\leftrightarrow e^{-\mathrm{i}\pi \sum_{k=1}^{j-1} \hat{n}_k} \hat{c}_j \\ \hat{\sigma}^z_j &\leftrightarrow 2\hat{n}_j - 1, \end{aligned} \tag{2.23}$$

The exponential term in equation (2.23) equals 1 if the number of occupied sites with index less than j is even, and -1 if it is odd. Equations (2.23) are known as the *Jordan-Wigner transformation* [55]. We can invert this transformation to map a system of spinless fermions to an ordered set of spins [56],

$$\hat{c}_j^\dagger \leftrightarrow e^{-i\pi \sum_{k=1}^{j-1} \frac{(\hat{\sigma}_k^z+1)}{2}} \hat{\sigma}_j^+ = \prod_{k=1}^{j-1} \left(-\hat{\sigma}_k^z \right) \hat{\sigma}_j^+ \equiv \hat{P}^{[j-1]} \hat{\sigma}_j^+$$

$$\hat{c}_j \leftrightarrow e^{+i\pi \sum_{k=1}^{j-1} \frac{(\hat{\sigma}_k^z+1)}{2}} \hat{\sigma}_j^- = \prod_{k=1}^{j-1} \left(-\hat{\sigma}_k^z \right) \hat{\sigma}_j^- \equiv \hat{P}^{[j-1]} \hat{\sigma}_j^- \qquad (2.24)$$

$$\hat{n}_j \leftrightarrow \frac{\hat{\sigma}_j^z + 1}{2}.$$

As a final remark: the exponentials and spin operators on the right hand side commute since they act on different sites.

Fermions with Spin

Mapping spin-1/2 fermions to a spin chain is a largely identical procedure, which we accomplish by arranging the spins in a ladder-like configuration as in figure 2.1. Let us consider a system of N (ordered) sites which can hold spin-$\frac{1}{2}$ fermions (electrons). We map the presence or absence of an electron on a specific site to the state of a qubit as in the previous section. However, we distinguish between spin-up and spin-down electrons. Thus, each fermionic site is mapped to 2 spins, which form a rung on our ladder. Repeating this procedure for each site in our fermionic chain results in a ladder system where rungs represent sites and legs represent the spin of the fermions. We then define an ordering in our ladder and transform the Hamiltonian accordingly using inverse Jordan-Wigner transform in equation (2.24).
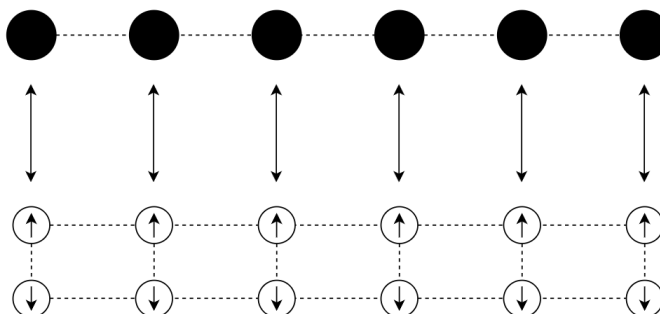
Figure 2.1: Jordan-Wigner transformation of a system of fermionic sites (upper part) to a double chain, or ladder, of spins (lower part).

The method of ordering the spins of the ladder is *subjective*; we are allowed to choose how to flatten the ladder to a 1-dimensional chain. The results is independent of this choice if the Jordan-Wigner transformation is applied consistently. Let us discuss the two most straightforward orderings, which are visualized in figure 2.2. Assume we have a total of L ordered sites which can hold an up fermion and a down fermion. We label the corresponding sites in the ladder by (j, s), with $j \in 1, ..., L$ and $s \in \uparrow, \downarrow$. Consider then the following two bijections to flatten the ladder:

$$\text{Method A: } (j, \uparrow) \rightarrow j \qquad (j, \downarrow) \rightarrow L + j, \qquad (2.25)$$

$$\text{Method B: } (j, \uparrow) \rightarrow 2j \qquad (j, \downarrow) \rightarrow 2j + 1. \qquad (2.26)$$

The choice of ordering will affect the form of the Jordan-Wigner transformed Hamiltonian of the system. However, since both systems model the same fermionic system, irrespective of our subjective choice of ordering the physics of the system remains the same.

Let us now describe the Jordan-Wigner transformation for the above two cases. For convenience we will not follow the notation of equations (2.25) and (2.26) but instead use the notation of [54], where Pauli operators acting on spins related to spin-up electrons on Hubbard site j are denoted by $\hat{\sigma}_j$ and those acting on spins related to spin-down electrons on Hubbard site j by $\hat{\tau}_j$. The index j therefore runs from 1 to L.
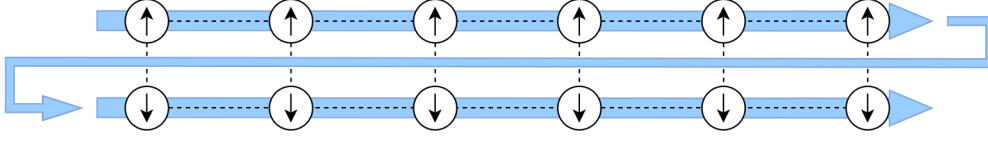
(a) The flattening method used by Prosen and Žnidarič in [54], presented in equation (2.25).
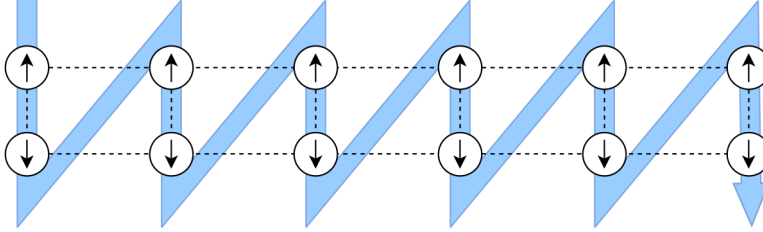
(b) The ordering presented in equation (2.26).

Figure 2.2: Two different methods to flatten a ladder system to a straight line.

We obtain Jordan-Winger transformations

$$
\hat{c}_{j,\uparrow}^{\dagger} \leftrightarrow \prod_{k=1}^{j-1}(-\hat{\sigma}_k^z)\,\hat{\sigma}_j^+ \equiv \hat{P}_{\hat{\sigma}}^{[j-1]}\,\hat{\sigma}_j^+ \qquad \hat{c}_{j,\downarrow}^{\dagger} \leftrightarrow \prod_{k=1}^{L}(-\hat{\sigma}_k^z)\prod_{k=1}^{j-1}(-\hat{\tau}_k^z)\,\hat{\tau}_j^+ \equiv \hat{P}_{\hat{\sigma}}^{[L]}\hat{P}_{\hat{\tau}}^{[j-1]}\,\hat{\tau}_j^+
$$

$$
\hat{c}_{j,\uparrow} \leftrightarrow \prod_{k=1}^{j-1}(-\hat{\sigma}_k^z)\,\hat{\sigma}_j^- \equiv \hat{P}_{\hat{\sigma}}^{[j-1]}\,\hat{\sigma}_j^+ \qquad \hat{c}_{j,\downarrow} \leftrightarrow \prod_{k=1}^{L}(-\hat{\sigma}_k^z)\prod_{k=1}^{j-1}(-\hat{\tau}_k^z)\,\hat{\tau}_j^- \equiv \hat{P}_{\hat{\sigma}}^{[L]}\hat{P}_{\hat{\tau}}^{[j-1]}\,\hat{\tau}_j^- \qquad (2.27)
$$

$$
\hat{n}_{j,\uparrow} \leftrightarrow \frac{\hat{\sigma}_j^z+1}{2} \qquad\qquad\qquad \hat{n}_{j,\downarrow} \leftrightarrow \frac{\hat{\tau}_j^z+1}{2}.
$$

for transformation A (bijection (2.25)) and

$$
\hat{c}_{j,\uparrow}^{\dagger} \leftrightarrow \prod_{k=1}^{j-1}(-\hat{\sigma}_k^z)\prod_{k=1}^{j-1}(-\hat{\tau}_k^z)\,\hat{\sigma}_j^+ \equiv \hat{P}_{\hat{\sigma}}^{[j-1]}\hat{P}_{\hat{\tau}}^{[j-1]}\hat{\sigma}_j^+ \qquad \hat{c}_{j,\downarrow}^{\dagger} \leftrightarrow \prod_{k=1}^{j}(-\hat{\sigma}_k^z)\prod_{k=1}^{j-1}(-\hat{\tau}_k^z)\,\hat{\tau}_j^+ \equiv \hat{P}_{\hat{\sigma}}^{[j]}\hat{P}_{\hat{\tau}}^{[j-1]}\hat{\tau}_j^+
$$

$$
\hat{c}_{j,\uparrow} \leftrightarrow \prod_{k=1}^{j-1}(-\hat{\sigma}_k^z)\prod_{k=1}^{j-1}(-\hat{\tau}_k^z)\,\hat{\sigma}_j^- \equiv \hat{P}_{\hat{\sigma}}^{[j-1]}\hat{P}_{\hat{\tau}}^{[j-1]}\hat{\sigma}_j^- \qquad \hat{c}_{j,\downarrow} \leftrightarrow \prod_{k=1}^{j}(-\hat{\sigma}_k^z)\prod_{k=1}^{j-1}(-\hat{\tau}_k^z)\,\hat{\tau}_j^- \equiv \hat{P}_{\hat{\sigma}}^{[j]}\hat{P}_{\hat{\tau}}^{[j-1]}\hat{\tau}_j^- \qquad (2.28)
$$

$$
\hat{n}_{j,\uparrow} \leftrightarrow \frac{\hat{\sigma}_j^z+1}{2} \qquad\qquad\qquad \hat{n}_{j,\downarrow} \leftrightarrow \frac{\hat{\tau}_j^z+1}{2}.
$$

for transformation B (bijection (2.26)). The transformation of the number operator is not affected by the choice of ordering.

One might raise the question why we would bother with defining two different transformations, especially since they describe the same physical system and result in the same dynamics. To answer this, let us state the general form that the hopping terms in Hamiltonian (1.15) will assume using the two different methods. These terms are of the form $\hat{c}_{i,s}^{\dagger}\hat{c}_{j,s'} + \text{H.c.}$, with $i < j$.

Using transformation A (equation (2.25)) and the relation $-\hat{\sigma}_i^+\hat{\sigma}_i^z = \hat{\sigma}_i^+$ we obtain,

$$\hat{c}^\dagger_{i,\uparrow}\hat{c}_{j,\uparrow} + \text{H.c.} \leftrightarrow \hat{\sigma}^+_i \hat{\sigma}^-_j \prod_{k=i+1}^{j-1} (-\hat{\sigma}^z_k) + \text{H.c.}$$

$$\hat{c}^\dagger_{i,\uparrow}\hat{c}_{j,\downarrow} + \text{H.c.} \leftrightarrow \hat{\sigma}^+_i \hat{\tau}^-_j \prod_{k=i+1}^{L} (-\hat{\sigma}^z_k) \prod_{k=1}^{j-1}(-\hat{\tau}^z_k) + \text{H.c.}$$

$$\hat{c}^\dagger_{i,\downarrow}\hat{c}_{j,\uparrow} + \text{H.c.} \leftrightarrow \hat{\tau}^+_i \hat{\sigma}^-_j \prod_{k=j+1}^{L} (-\hat{\sigma}^z_k) \prod_{k=1}^{i-1}(-\hat{\tau}^z_k) + \text{H.c.}$$

$$\hat{c}^\dagger_{i,\downarrow}\hat{c}_{j,\downarrow} + \text{H.c.} \leftrightarrow \hat{\tau}^+_i \hat{\tau}^-_j \prod_{k=i+1}^{j-1} (-\hat{\tau}^z_k) + \text{H.c..}$$

(2.29)

Similarly, using transformation B (equation (2.26)) we obtain

$$\hat{c}^\dagger_{i,\uparrow}\hat{c}_{j,\uparrow} + \text{H.c.} \leftrightarrow \hat{\sigma}^+_i \hat{\sigma}^-_j \prod_{k=i+1}^{j-1} (-\hat{\sigma}^z_k) \prod_{k=i}^{j-1}(-\hat{\tau}^z_k) + \text{H.c.}$$

$$\hat{c}^\dagger_{i,\uparrow}\hat{c}_{j,\downarrow} + \text{H.c.} \leftrightarrow \hat{\sigma}^+_i \hat{\tau}^-_j \prod_{k=i+1}^{j-1} (-\hat{\sigma}^z_k) \prod_{k=i}^{j-1}(-\hat{\tau}^z_k) + \text{H.c.}$$

$$\hat{c}^\dagger_{i,\downarrow}\hat{c}_{j,\uparrow} + \text{H.c.} \leftrightarrow \hat{\tau}^+_i \hat{\sigma}^-_j \prod_{k=i+1}^{j-1} (-\hat{\sigma}^z_k) \prod_{k=i+1}^{j-1} (-\hat{\tau}^z_k) + \text{H.c.}$$

$$\hat{c}^\dagger_{i,\downarrow}\hat{c}_{j,\downarrow} + \text{H.c.} \leftrightarrow \hat{\tau}^+_i \hat{\tau}^-_j \prod_{k=i+1}^{j} (-\hat{\sigma}^z_k) \prod_{k=i+1}^{j-1} (-\hat{\tau}^z_k) + \text{H.c.}$$

(2.30)

for bijection B. The differences between equations (2.29) and (2.30) are seen in the bounds of the products of Pauli matrices resulting from the fermionic anticommutation relations. In method A, the number of $\hat{\sigma}^z$ matrices involved in a hopping process from one leg of the ladder to the other, i.e. a spin-flip process, scales proportionally to the *total number of fermionic sites L*. As will be discussed in chapter 3, the matrix product states formalism is optimised for systems with local interactions and hence benefits from transforming the system via method B, which preserves locality of interactions. An illustration of this point is provided in figure 2.3.
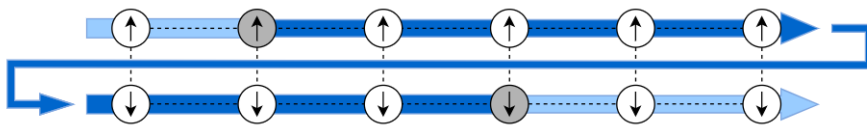
(a) Tranformation A.
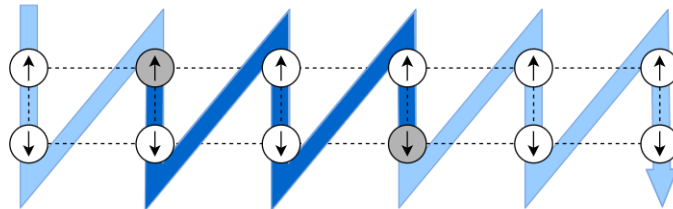
(b) Transformation B.

Figure 2.3: The choice of ordering determines which sites are involved in a hopping process of the form $\hat{c}^\dagger_{j\uparrow}\hat{c}_{j+2\downarrow}$. The number of involved sites scales with the system length in transformation A, while it is independent of system length for transformation B.

While transformation B is preferable in the presence of spin-flip processes, in the case that the Hamiltonian does not allow for spin flip processes conversely makes transformation A preferable, as this transformation involves less $\hat{\sigma}^z$ operators for hopping terms which remain on the same leg. This is the reason it is the method of choice in [54]. In this work we will use both methods. For the standard Hubbard model we use transformation A as in [54] while for the Hubbard model with spin-orbit coupling we use transformation B.

The last point to address is the Jordan-Wigner transformation of Lindblad operators. This might seem trivial, since, in this work, these are all single creation or annihilation operators with a specific coupling strength, which we can already transform using equations (2.27) and (2.28). Transforming the Lindblad operators this way is completely valid, however it will leave us with quite lengthy operators; the Lindblad operators on the last site of our flattened ladder is in this case a product of $2L$ spin matrices. In Prosen and Žnidarič' equations (5) and (6) we see that the products of spin matrices resulting from the Jordan-Wigner transformation are omitted for an undisclosed reason. To the best of the author's knowledge there is no literature specifically addressing this matter, except for a short footnote found in [57] on page 9, and the fact that these operators *are* explicitly included in [58].

The footnote in [57] mentions that the product of $\hat{\sigma}^z$ and $\hat{\tau}^z$ matrices, referred to as a Casimir operator, do not affect the dynamics of the system and are therefore neglected. As will become apparent in the next chapter, the matrix product states ansatz is only effective for systems where interactions involve at most a few sites, and not the entire system. It is crucial to the viability of our method that we are not required to apply operators which act on all sites of the system simultaneously.

Let us therefore comment on the footnote in [57]. We can see from the form of equations (2.29), (2.30) that the Jordan-Wigner transformation is invariant for reversal of the ordering of our bijection (i.e. interchanging the start and end of our ordering). Additionally, we know that the action of a single Lindblad operator acting on a particular site depends on the location of that site, but not on the subjectively chosen ordering. Consider now a Lindblad operator acting on site L of the lower leg of our ladder. For both ordering A and B this means it should act with $-\hat{\sigma}^z$ or $-\hat{\tau}^z$ on all other sites in the ladder, as can be seen in figure 2.2. If we reverse the ordering, there are no spin-matrices acting on these sites. Since the result *must* be identical in both cases, this implies that the product of spin-z matrices does not affect the dynamics and hence can be neglected, explaining the comment in [57]. This result holds for all Lindblad operators acting on arbitrary sites in the system, allowing us to choose the most advantageous transformation (i.e. the one with the least amount of sites involved) for each operator individually.

What is not explained by this reasoning, is the the omission of the products of spin-z matrices for operators $\hat{L}_{3,4,5,6}$ in [54]. If we refer to figure 2.3a it is clear that the form of the Jordan-Wigner transformation is not invariant for setting the first site of the 'down' leg or the last site of the 'up' leg as our starting point, and hence our previous argument does not in this case. However, the Hamiltonian of [54] does not include interactions of the form presented in figure 2.3a. Consequently, the Hamiltonian in [54] is invariant for choosing either of the 4 corners of the ladder system as a starting point. Given the fact that we have found no further literature addressing this matter, we are left to speculation. Given that [54] implicitly assumes the product of spin-z matrices to be irrelevant, it appears to be that if the Jordan-Wigner transformation of the Hamiltonian of a system is invariant for two different orderings, the action of a Jordan-Wigner transformed Lindblad operator acting on a single site is also invariant for these same two orderings. In any case, we will not have to assume this conjecture to be true for the Jordan-Wigner transformation of the Hubbard model with spin-orbit coupling, since we will employ transformation B.

2.4 Transport Through One-Dimensional Models

The aim of this work is to simulate boundary-driven transport through a Hubbard model modeling a chiral structure, with Coulomb and spin-orbit interactions present. We will approach this problem by simulating three steps from the simplest transport along a chain to a chain with SOC. The first two models were studied in literature [54, 59] using similar approaches as in this thesis and therefore allow us to verify the accuracy of our method, acting as stepping stones before we attempt to simulate the full model with SOC. The three models are

- A boundary-driven spin-1/2 XXZ-Heisenberg model.

- A boundary-driven Hubbard model with on-site Coulomb interactions mapped to a spin system using the Jordan-Wigner transformation.

- A boundary-driven Hubbard model with on-site Coulomb interactions and next-nearest neighbour spin-orbit coupling, mapped to a spin system using the Jordan-Wigner transformation.

As stated, the non-equilibrium situation in the systems will be induced by introducing dissipative couplings at either ends of the models, which are described using the Lindblad equation.

2.4.1 The Spin-1/2 XXZ-Heisenberg Chain

The first model of interest is the XXZ model, which describes a (one-dimensional) spin system with nearest neighbour couplings that is isotropic in the XY plane but is anisotropic for general rotations. Specifically, the XXZ Hamiltonian takes the form

$$\hat{H}_{XXZ} = \sum_{j=1}^{N-1} (\hat{\sigma}_j^x \hat{\sigma}_{j+1}^x + \hat{\sigma}_j^y \hat{\sigma}_{j+1}^y + \Delta \hat{\sigma}_j^z \hat{\sigma}_{j+1}^z). \tag{2.31}$$

The parameter Δ is a free parameter describing the anisotropy. For $\Delta = 0$ the model reduces to the XY model and for $\Delta = 1$ it reduces to the standard Heisenberg model, which are both completely isotropic. The XXZ model in equilibrium is exactly solvable in a number of specific cases, including the ones previously mentioned and the weakly and strongly isotropic cases, see [60].

In order to induce spin-transport in the chain we introduce two Lindblad operators which act on either end,

$$\hat{L}_1 = \sqrt{2\gamma}\hat{\sigma}_1^+ \qquad\qquad \hat{L}_2 = \sqrt{2\gamma}\hat{\sigma}_N^-, \tag{2.32}$$

with $\hat{L}_1$ acting on the leftmost spin and $\hat{L}_2$ acting on the rightmost spin. These couplings model a spin-source and a spin-drain, respectively, and will induce transport through the chain that converges to a nonequilibrium steady state. This model has been solved analytically by Prosen and Žnidarič in 2011 using the matrix product states ansatz [61]. The model has also been used as a performance benchmark for an MPS method related to the one employed in this thesis [59].

The boundary-driven XXZ model is one of the simplest spin-transport models available to us, as it includes exclusively nearest-neighbour interactions and is driven by a single Lindblad operator at either end. As the exact steady state transport spin profile and spin current of the steady state have been documented in [61] it serves as an ideal benchmark for verifying whether our method works for simple transport simulations.

2.4.2 The Hubbard Chain

After verifying that the method can effectively simulate boundary-driven transport in spin systems, the next step is to verify whether it can simulate boundary-driven transport in the Hubbard model without spin-orbit coupling. The Hubbard model we will simulate is of the form of equation (2.7) with exclusively nearest neighbour hopping terms and a uniform parameter t:

$$\hat{H}_{\text{Hubbard}} = -t \sum_{j=1}^{N-1} \sum_s \left(\hat{c}_{j,s}^\dagger \hat{c}_{j+1,s} + \text{H.c.} \right) + U \sum_{j=1}^{N} \hat{n}_{j,\uparrow} \hat{n}_{j,\downarrow}.$$

As discussed in section 2.3, using ordering A (bijection (2.25)), this Hamiltonian is equivalent to the following spin model via the Jordan-Wigner transformation (2.27):

$$\begin{aligned}
\hat{H} &= -t \sum_{j=1}^{N-1} (\hat{\sigma}_j^+ \hat{\sigma}_{j+1}^- + \hat{\tau}_j^+ \hat{\tau}_{j+1}^- + \text{H.c.}) + U \sum_{j=1}^{N} \frac{(\hat{\sigma}_j^z + 1)(\hat{\tau}_j^z + 1)}{4} \\
&= -\frac{t}{2} \sum_{j=1}^{N-1} (\hat{\sigma}_j^x \hat{\sigma}_{j+1}^x + \hat{\sigma}_j^y \hat{\sigma}_{j+1}^y + \hat{\tau}_j^x \hat{\tau}_{j+1}^x + \hat{\tau}_j^y \hat{\tau}_{j+1}^y) + U \sum_{j=1}^{N} \frac{(\hat{\sigma}_j^z + 1)(\hat{\tau}_j^z + 1)}{4}.
\end{aligned} \tag{2.33}$$

The second line highlights the similarities with the previous Hamiltonian for $\Delta = 0$ (the XY model). This model has been studied in-depth in the context of boundary-driven transport by Prosen and Žnidarič in 2012 using the method also used in this thesis [54]. It therefore serves as a useful accuracy benchmark before the spin-orbit interaction is included. The main difficulty with this model is the presence of next-nearest neighbour terms in the spin model. This requires additional considerations in the MPS framework which we will discuss in section 3.2.3. In [54] and in this work, the nonequilibrium situation is induced by a total of 8 Lindblad operators acting on either ends of both legs of the ladder,

$$\begin{aligned}
\hat{L}_{1,2} &= \sqrt{\gamma(1 \mp \nu)}\hat{\sigma}_1^\pm \quad \hat{L}_{3,4} = \sqrt{\gamma(1 \pm \nu)}\hat{\sigma}_N^\pm, \\
\hat{L}_{5,6} &= \sqrt{\gamma(1 \mp \nu)}\hat{\tau}_1^\pm \quad \hat{L}_{7,8} = \sqrt{\gamma(1 \pm \nu)}\hat{\tau}_N^\pm.
\end{aligned} \tag{2.34}$$

$\hat{L}_{1,2}$ and $\hat{L}_{3,4}$ act on the left and right sides of the upper leg of the ladder in figure 2.1, respectively, and similarly $\hat{L}_{5,6}$ and $\hat{L}_{7,8}$ act on the left and right sides of the the lower leg of the ladder in figure 2.1. For the transformation of the Lindblad operators, we operate under the assumption stated that, if the Jordan-Wigner transformation of the Hamiltonian of a system is invariant for two different orderings, the action of a Jordan-Wigner transformed Lindblad operator acting on a single site is also invariant for these same two orderings. For more information, see the discussion at the end of section 2.3.

2.4.3 The Hubbard Chain with Next-Nearest Neighbour Spin-Orbit Interactions

The final model we shall simulate is the one studied by Fransson in [33]. Essentially, this model is identical to the previous one with two additional terms. Fransson includes an on-site energy term,

$$\sum_{j=1}^{N} \epsilon(\hat{n}_{j,\uparrow} + \hat{n}_{j,\downarrow}). \tag{2.35}$$

Since the on-site energy ϵ is equal for all sites we will choose $\epsilon = 0$ for convenience. We add a spin-orbit interaction as described in section 1.3.2 between each pair of next-nearest neighbours,

$$\lambda \sum_{j=1}^{N-2} \sum_{ss'} \left(\mathrm{i}\, \hat{c}_{j,s}^{\dagger} (\mathbf{v}_j \cdot \boldsymbol{\sigma})_{ss'} \hat{c}_{j+2,s'} + \text{H.c.} \right). \tag{2.36}$$

This gives us our final Hamiltonian, that was also presented in equation (1.15),

$$\hat{H} = -t \sum_{j=1}^{N-1} \sum_{s} (\hat{c}_{j,s}^{\dagger} \hat{c}_{j+1,s} + \text{H.c.}) + \sum_{j=1}^{N} U \hat{n}_{j,\uparrow} \hat{n}_{j,\downarrow} + \lambda \sum_{j=1}^{N-2} \sum_{ss'} \left(\mathrm{i}\, \hat{c}_{j,s}^{\dagger} (\mathbf{v}_j \cdot \boldsymbol{\sigma})_{ss'} \hat{c}_{j+2,s'} + \text{H.c.} \right). \tag{2.37}$$

As discussed in section 2.3, the presence of spin-flip processes in this Hamiltonian means that using transformation A does not preserve locality in the system of spins; the number of spin-z matrices involved in the spin-orbit terms scales proportional to the length of the Hubbard model. Hence, transformation B is preferred in this case. This has no consequences for the Coulomb interaction term, but the hopping term changes to

$$-t \sum_{j=1}^{N-1} \sum_{s} (\hat{c}_{j,s}^{\dagger} \hat{c}_{j+1,s} + \text{H.c.}) \quad \leftrightarrow \quad -t \sum_{j=1}^{N-1} (\hat{\sigma}_j^+ \hat{\sigma}_{j+1}^- (-\hat{\tau}_j^z) + \hat{\tau}_j^+ \hat{\tau}_{j+1}^- (-\hat{\sigma}_{j+1}^z) + \text{H.c.}). \tag{2.38}$$

Let us similarly transform the four terms per next-nearest neighbour pair resulting from equation (2.36). We omit the factor λ in front, define $\mathbf{v}_j = \text{vec}(v_x, v_y, v_z)$ and transform the four terms separately,

$$
\begin{aligned}
\mathrm{i} v_z\, \hat{c}_{j,\uparrow}^{\dagger} \hat{c}_{j+2,\uparrow} &\leftrightarrow & \mathrm{i} v_z\, \hat{\sigma}_j^+ \hat{\sigma}_{j+2}^- & \; (-\hat{\tau}_j^z)(-\hat{\sigma}_{j+1}^z)(-\hat{\tau}_{j+1}^z) \\
\mathrm{i}(v_x - \mathrm{i} v_y)\, \hat{c}_{j,\uparrow}^{\dagger} \hat{c}_{j+2,\downarrow} &\leftrightarrow & \mathrm{i}(v_x - \mathrm{i} v_y)\, \hat{\sigma}_j^+ \hat{\tau}_{j+2}^- & \; (-\hat{\tau}_j^z)(-\hat{\sigma}_{j+1}^z)(-\hat{\tau}_{j+1}^z)(-\hat{\sigma}_{j+}^z) \\
\mathrm{i}(v_x + \mathrm{i} v_y)\, \hat{c}_{j,\downarrow}^{\dagger} \hat{c}_{j+2,\uparrow} &\leftrightarrow & \mathrm{i}(v_x + \mathrm{i} v_y)\, \hat{\tau}_j^+ \hat{\sigma}_{j+2}^- & \; (-\hat{\sigma}_{j+1}^z)(-\hat{\tau}_{j+1}^z) \\
-\mathrm{i} v_z\, \hat{c}_{j,\downarrow}^{\dagger} \hat{c}_{j+2,\downarrow} &\leftrightarrow & -\mathrm{i} v_z\, \hat{\tau}_j^+ \hat{\tau}_{j+2}^- & \; (-\hat{\sigma}_{j+1}^z)(-\hat{\tau}_{j+1}^z)(-\hat{\sigma}_{j+2}^z)
\end{aligned}
\tag{2.39}
$$

The dissipation at the edges of the system is described using the 8 Lindblad operators given in equation (1.16). Given the fact that we use a different Jordan-Wigner transformation than in [54], the transformed operators will also be slightly different. However, for the transformation of these operators we *do not* have to make use of the assumption stated at the end of section 2.3. We obtain the Jordan-Wigner transformed Lindblad operators:

$$
\begin{aligned}
\hat{L}_{1,2} &= \sqrt{\gamma_{\uparrow}(1 \pm \nu)}\, \hat{\sigma}_1^{\pm} & \hat{L}_{3,4} &= \sqrt{\gamma(1 \mp \nu)}\, \hat{\sigma}_N^{\pm}(-\hat{\tau}_N^z), \\
\hat{L}_{5,6} &= \sqrt{\gamma_{\downarrow}(1 \pm \nu)}\, \hat{\tau}_1^{\pm}(-\hat{\sigma}_1^z) & \hat{L}_{7,8} &= \sqrt{\gamma(1 \mp \nu)}\, \hat{\tau}_N^{\pm}.
\end{aligned}
\tag{2.40}
$$

3 Matrix Product States for Transport

The main problem in the study of interacting quantum many body systems is the exponential scaling of the size of the system Hilbert space with the particle number N, limiting the reachable system size in simulations. Many efforts have been made to increase the maximum reachable number of particles, through systematic approximation methods such as mean-field theory and perturbation theory or numerically with Monte Carlo approaches. For (quasi-)one-dimensional systems, one of the most powerful tools available is the matrix products states (MPS) formalism, which makes use of the low entanglement of low-lying excited states in systems with local interactions. By making use of consecutive Schmidt decompositions the quantum state is written as a product of matrices. The size of these matrices is truncated by removing the lowest Schmidt values, thereby reducing the complexity of the simulation from exponential with system size to linear with system size. This, in combination with an efficient time-evolution method called Time-Evolving Block Decimation (TEBD), allows us to simulate 1D quantum systems of considerable length efficiently and accurately without requiring any approximations to the Hamiltonian. The method has grown out of the Density Matrix Renormalisation Group (DMRG) method invented by Steven R. White in 1992 [62] and has been used in the study of quantum many-body physics for well over 20 years. The formalism has been extended to allow for the simulation of 2D systems and the study of thermal states, among other uses. For an excellent review of MPS and its precursor DMRG I refer to the work of Schöllwock [63], on which most this chapter is based. This chapter contains a brief overview of the basic concepts of MPS and a more detailed look into simulating mixed states and transport in the MPS framework.

3.1 Basic Principles of Matrix Product States

3.1.1 The Matrix Product State Decomposition

At the root of the matrix product state formalism lies the *Schmidt decomposition*, an important tool to study the entanglement within bipartite systems. Consider a bipartite system consisting of subsystems labeled A and B, with the total system Hilbert space defined as $\mathcal{H} = \mathcal{H}_A \otimes \mathcal{H}_B$. Let the state be in an arbitrary state $|\psi\rangle \in \mathcal{H}$. Each such state can be written as a weighted sum of product states of the subsystem (basis) states:

$$|\psi\rangle = \sum_\alpha \lambda_\alpha |\alpha\rangle_A \otimes |\alpha\rangle_B, \tag{3.1}$$

$$|\alpha\rangle_A \in \mathcal{H}_A \qquad |\alpha\rangle_B \in \mathcal{H}_B.$$

This is the Schmidt decomposition of $|\psi\rangle$. From this point on, the notations $|\alpha\rangle_A \otimes |\alpha\rangle_B$ and $|\alpha\rangle_A |\alpha\rangle_B$ are defined to be equivalent. The coefficients λ_α are the Schmidt coefficients, which can be shown to be positive definite and are unique up to reordering. We use the common convention to order the Schmidt values by decreasing value. Moreover, as a consequence of the normalisation of $|\psi\rangle$ we also have $\sum_\alpha \lambda_\alpha^2 = 1$. The Schmidt values give a characterization of the entanglement between the two subsystems for a given quantum state. The *Von Neumann entanglement entropy* (VNEE) gives a quantification of that entanglement. It is defined as

$$S = -\text{Tr}\big(\rho \log_2(\rho)\big). \tag{3.2}$$

It is easy to infer the reduced density matrices (see section 2.1) of subsystems A and B from the Schmidt decomposition in equation (3.1). Substituting these in equation (3.2) then gives the relation between the entanglement entropy and the Schmidt values:

$$S = -\sum_\alpha \lambda_\alpha^2 \log_2(\lambda_\alpha^2). \tag{3.3}$$

If only one Schmidt value is nonzero, it must have value 1. The system is then in a product state of the two subsystems and hence a pure state. Equation (3.3) gives us an entanglement entropy of 0, as we would expect.

The Schmidt decomposition is closely related to the *singular value decomposition* (SVD), an important tool in linear algebra. Given an abitrary $(N_1 \times N_2)$ matrix M of rank R, the singular value decomposition guarantees that this matrix can be written as

$$M = U\Lambda V^\dagger, \tag{3.4}$$

with U a $(N_1 \times R)$ matrix of orthonormal columns, Λ a $(R \times R)$ diagonal matrix containing the *singular values*, which are ranked in decreasing order, and $V^\dagger$ is a matrix of size $(R \times N_2)$ with orthonormal rows. Matrices U and $V^\dagger$ are are left and right orthogonal ($U^\dagger U = V^\dagger V = \mathbb{I}$), respectively, and are unitary if M is square. The

orthonormal columns of U are the *left singular vectors* and the orthonormal rows of $V^\dagger$ are the *right singular vectors*.

The singular value decomposition can be used to obtain the Schmidt decomposition of a state $|\psi\rangle$. Any pure state in $\mathcal{H}$ can be written as

$$|\psi\rangle = \sum_{ij} c_{ij} |i\rangle_A |j\rangle_B, \tag{3.5}$$

with c_{ij} a matrix of coefficients. We define the rank of this matrix as R. Let us perform a singular value decomposition on the matrix c,

$$\sum_{ij} c_{ij} |i\rangle_A |j\rangle_B = \sum_{ij} \sum_{\alpha=1}^{R} U_{i\alpha} \Lambda_\alpha V^\dagger_{\alpha j} |i\rangle_A |j\rangle_B. \tag{3.6}$$

To obtain the Schmidt decomposition we define $|\alpha\rangle_A = \sum_i U_{i\alpha} |i\rangle_A$ and $|\alpha\rangle_B = \sum_j V^\dagger_{\alpha j} |j\rangle_B$. These sets of states can be extended to form a new orthonormal basis for $\mathcal{H}_A$ and $\mathcal{H}_B$.

In this section, we defined the Schmidt decomposition for bipartite systems. However, it is not difficult to see that this concept is straightforwardly generalized to any composite system. Let us consider a system composted of multiple d-level systems numbered 1 to N. We will assume our system is a one-dimensional lattice, and each subsystem corresponds to a single lattice site, with subsystem 1 corresponding to the leftmost site and subsystem N corresponding to the rightmost site. We will perform consecutive Schmidt decompositions between each neighbouring pair of sites in this system. The state of our system is described by a tensor $c_{i_1 i_2 \dots i_N}$ of size d^N. We perform the first Schmidt decomposition between subsystem 1 and the rest of the subsystems by reshaping tensor $c_{i_1 i_2 \dots i_N}$ to a matrix $c_{i_1 j}$ and performing a singular value decomposition

$$c_{i_1 j} = \sum_{\alpha_1}^{R_1} U_{i_1 \alpha_1} \Lambda^{[1]}_{\alpha_1} V^\dagger_{\alpha_1 j}.$$

We now relabel $U_{i_1 \alpha_1} \to A^{[1]}_{i_1 \alpha_1}$ and contract the diagonal matrix of singular values with $V^\dagger$, which we reshape back to a tensor $c_{\alpha_1 i_2 \dots i_N}$. Now, on this smaller composite system we perform a Schmidt decomposition between subsystem 2 and the other subsystems. We take indices α_1 and i_2 together as an index i'_2 and get a matrix $c_{i'_2 j'}$. We perform the same procedure as before obtain a matrix $A^{[2]}_{i_2 \alpha_1 \alpha_2}$.

Repeating this process for all subsystems recursively decomposes the tensor c into a product of matrices. If we denote the basis of the Hilbert space $\mathcal{H}_j$ of subsystem j as $\{|i_j\rangle\}_{i=1}^{d}$ we can write the state $|\psi\rangle$ of our system as

$$|\psi\rangle = \sum_{i_1 i_2 \dots i_N}^{d} c_{i_1 i_2 \dots i_N} |i_1 i_2 \dots i_N\rangle = \sum_{i_1 i_2 \dots i_N}^{d} \sum_{\alpha_1 \alpha_2 \dots \alpha_N = 1}^{R_1 \dots R_{N-1}} A^{[1]}_{i_1 \alpha_1} A^{[2]}_{i_2 \alpha_1 \alpha_2} \dots A^{[N]}_{i_N \alpha_{N-1}} |i_1 i_2 \dots i_N\rangle. \tag{3.7}$$

This is the *left canonical matrix product state decomposition* of $|\psi\rangle$. The indices α_j are the *bond indices* and the dimensions R_j of matrices $A^{[j]}$ are called the *bond dimensions*. The i_j index the states of site j and are called the *physical indices*. Due to our definitions of the matrices $A^{[j]}$ from the singular value decomposition, we have for each j that $A^{[j]}$ is left-normalised: $(A^{[j]})^\dagger A^{[j]} = \mathbb{I}$.

The notation in equation (3.7), while informative, is a bit unwieldy. Therefore, we will neglect to explicitly write the sum over the bond indices α_j. We will also leave out the index in square brackets that labels which subsystem a matrix governs and replace it with the index i_j. This gives us the condensed MPS notation

$$|\psi\rangle = \sum_{i_1 i_2 \dots i_N}^{d} A^{i_1} A^{i_2} \dots A^{i_N} |i_1 i_2 \dots i_N\rangle. \tag{3.8}$$

We can also begin our matrix product state decomposition from the right side of the chain, starting at the bond between sites N and $N-1$, defining $B^{[i_N]} = V^\dagger$ and contracting the singular values into U. We then obtain a decomposition

$$|\psi\rangle = \sum_{i_1 i_2 \dots i_N}^{d} B^{i_1} B^{i_2} \dots B^{i_N} |i_1 i_2 \dots i_N\rangle, \tag{3.9}$$

with $B^{[j]}$ being right-normalised for all j, $B^{[j]}(B^{[j]})^\dagger = \mathbb{I}$. This is known as the right canonical decomposition. We obtain the mixed canonical description by decomposing from the right up to a site j and from the left up to site $j+1$, leaving the singular values between j and $j+1$ explicit between the two halves,

$$|\psi\rangle = \sum_{i_1 i_2 \dots i_N}^{d} A^{i_1} \dots A^{i_j} \Lambda^{[j]} B^{i_{j+1}} \dots B^{i_N} |i_1 i_2 \dots i_N\rangle, \tag{3.10}$$

As a last note, it is possible to explicitly include the singular values in the notation by substituting $\mathbb{I} = \Lambda^{[j]}\Lambda^{[j]-1}$ between A^{i_j} and $A^{i_{j+1}}$ ($B^{i_{j-1}}$ and B^{i_j}). Defining

$$\Gamma^{i_j} \equiv (\Lambda^{[j-1]})^{-1} A^{i_j} \qquad \left(\Gamma^{i_j} \equiv B^{i_j} (\Lambda^{[j]})^{-1} \right) \tag{3.11}$$

for $j \in \{2, ..., N-1\}$ gives us the decomposition

$$|\psi\rangle = \sum_{i_1 i_2 ... i_N}^{d} \Gamma^{i_1} \Lambda^{[1]} \Gamma^{i_2} \Lambda^{[2]} ... \Lambda^{[N-1]} \Gamma^{i_N} |i_1 i_2 ... i_N\rangle . \tag{3.12}$$

This is the Vidal decomposition or Vidal notation of matrix product states, named after Giuffré Vidal, who first introduced it [64]. As we will see in the following subsection, this way of writing quantum states will gives us a number of advantages over the conventional state vector formulation of quantum states.

While on the topic of notations, it is a good time to introduce a commonly adopted graphical representation of matrix product states. The notation is based on the Penrose tensor diagram notation, where tensors are represented by a block such as a square, diamond or circle. Out of the block extend lines which represent the tensor indices. Lines which connect two different blocks represent contracted indices between two tensors. Blocks without any free lines extending from them represent scalars. We will use diamonds to denote diagonal tensors. In figure 3.1 a number of examples of Penrose graphical notation are presented. The procedure of decomposing a state into an MPS as is described in this section can also be represented graphically, see figure 3.2.

(a) A tensor with 4 indices.

(b) Two different representations of tensors with 2 indices (matrices).

(c) A diagonal matrix.

(d) Two different examples of scalars.
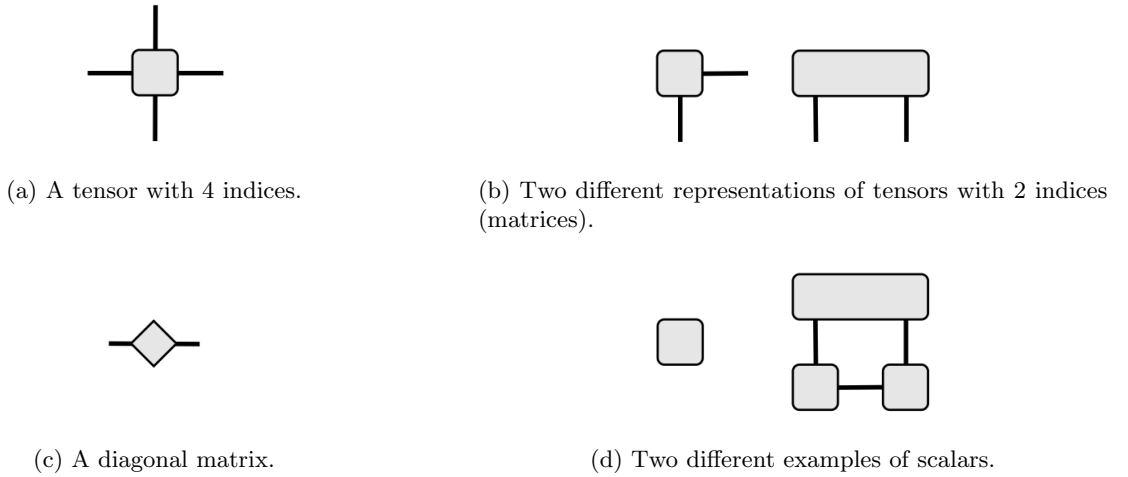
Figure 3.1: Examples of Penrose diagrams of various tensors and scalars.
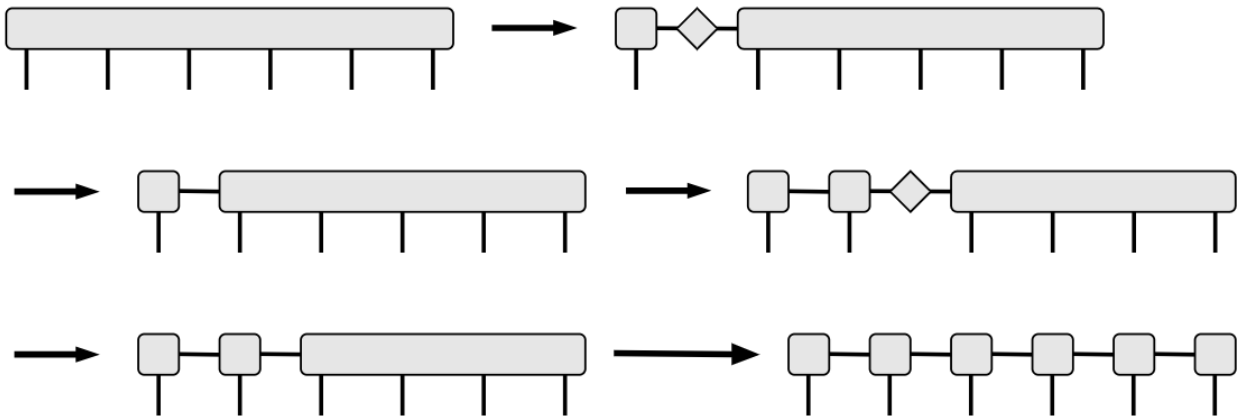
Figure 3.2: The matrix product state decomposition from the left of a state with 6 indices. The final result is of the form of equation (3.8).

3.1.2 Complexity and Area Law States

One of the main difficulties in the field of many-body quantum theory is the exponential scaling of the computational complexity with the number of particles. As mentioned, a state $|\psi\rangle$ composed of N subsystems each of dimension d exists in a d^N dimensional Hilbert space. Using consecutive singular value decompositions we have rewritten the state vector $|\psi\rangle$ as a product of matrices (equations (3.8) and (3.12)), but this has so far only increased the complexity of our description. However, this way of writing our states has exposed the Schmidt values of our state. We can leverage this to our advantage by reducing the complexity of our description from exponential to *linear* in system length, for a certain class of states.

Consider a Schmidt decomposition of a system composed of two particles as in equation (3.1), where the Hilbert spaces $\mathcal{H}_{A(B)}$ both have dimension d. As mentioned, if only a single Schmidt value is nonzero, the system is in a product state between the two subsystems, $|\psi\rangle = |\alpha_A\rangle |\alpha_B\rangle$. The left hand side has a complexity d^2, while the right hand side has a complexity $2d$, a drastic reduction in case $d \gg 2$. As a next step we consider a state where subsystems A and B are weakly entangled, in the sense that the Schmidt values decay rapidly. In this situation, the entanglement entropy as defined in equation (3.3) will be small, hence we call such states weakly entangled. In the Schmidt decomposition, most of the information about our state will be contained in the terms with high singular values, while the terms with low singular values represent minor corrections that can be neglected at the costs of a small error. Suppose we have a composite system of N particles that has been decomposed into the form of equation (3.12). If all singular values in (3.12) decay sufficiently quickly to justify truncating all $\Lambda^{[j]}$ beyond the first χ singular values, we are left with a relatively accurate description of our state $|\psi\rangle$ while reducing the complexity from d^N to $\mathcal{O}(Nd\chi^2)$.

The accuracy of this approximation crucially depends on the entanglement between the different subsystems and it is best suited for states with weak entanglement over short distances. This is usually not the case for arbitrary states of composite systems, for which the entanglement entropy of a bipartition usually scales proportional to the volume of the subsystems, i.e. it follows a *volume law*. For an intuitive understanding, consider a 1-dimensional lattice of particles in a general state that is bipartitioned into a left- and right side. As the system is in a general state, there is relatively strong entanglement even for distant particles. Thus there is entanglement between all the particles in each subsystem, meaning the amount of entanglement depends on the volume of the subsystems.

However, ground states and low-lying excited states of gapped Hamiltonians with local interactions do not follow the volume law, but instead follow an *area law*. Area law states are composite states for which the entanglement entropy scales proportional to the surface area between the subsystems. Conveniently, for 1-dimensional systems the surface area of any (connected) subsystem is constant, which means that the entanglement entropy does not scale with the size of a subsystem. Intuitively, an energy gap is indicative of a finite correlation length, so that entanglement between subsystems only concerns particles close to the boundary and hence weakly excited states will have entanglement entropy proportional to the area of the subsystem boundaries. Because states satisfying an area law have rapidly decaying Schmidt values [65], it is these states that are best suited for matrix product state simulations. Thus, when using matrix product states we restrict ourselves to the subset of states for which the area law holds.

The aim of this work is to use matrix product states to simulate nonequilibrium steady states of various models that are driven by couplings to a reservoir. This naturally raises the question whether the states we are aiming to find are even suited for matrix product states simulations; whether they fall within the subset of the Hilbert space which satisfies the area law. There is evidence that suggests this to be true. There have been multiple studies where matrix product states have successfully been applied to find the steady state of nonequilibrium systems, for example [54, 59, 66]. Other works have specifically studied the entanglement structure of steady states of driven systems [45, 46] and found that the steady states were only lightly entangled, even for strongly-interacting systems. However, to the author's best knowledge, there exists no guarantee that the NESS of a specific system will be lightly entangled or that the entanglement structure follows an area law. Moreover, as of yet no studies have investigated the entanglement structure of the NESS of the boundary-driven Hubbard model with (adapted) Kane-Mele spin-orbit interactions, which will therefore be done in this thesis.

We can make some qualitative predictions on the behaviour of the entanglement entropy in a driven system over time, with some assumptions. Let us consider a strongly interacting system that is connected at the ends to dissipative reservoirs, with a NESS that is lightly entangled. Assuming the system is initially in a product state, we expect the entanglement entropy of the system to increase in the short-time regime, as the dynamics in the bulk of the system will be dominated by the Hamiltonian. Eventually, the time evolution will reach a transient regime in which the nonequilibrium dynamics start to dominate over the Hamiltonian, meaning the entanglement entropy starts to decrease. In the long-time regime the system converges to the NESS and hence the entanglement entropy stabilizes at a low value. This behaviour has been observed in a study performed by Panda et al. [46]. In practical terms this means that the truncation parameter χ should be sufficiently large

to account for the (relatively) high entanglement in the system in the transient regime of the time evolution, assuming that the degree of entanglement of the NESS we are attempting to reach is low enough to justify the matrix product state ansatz.

3.2 Calculations using MPS

We have seen how we obtain the MPS form of an arbitrary quantum state by applying consecutive singular value decompositions, and how they can be used to efficiently describe weakly entangled quantum states. In this section we will see that the MPS formalism also allows for efficient calculation of expectation values and allows for a powerful algorithm for calculating time evolution. The methods reviewed in this section are extensively discussed in [63]. This section will provide only a brief overview of these methods.

3.2.1 Overlaps, Operator Application and Expectation Values

Let us begin with the inner product between two states $|\psi\rangle \in \mathcal{H}$ and $|\phi\rangle \in \mathcal{H}$. We can naively calculate the overlap by contracting all bond indices and then calculate the inner product in the standard way, but this is inefficient as it requires d^N operations. If we instead use the 'zip-up' method pictured in figure 3.3b we can reduce the number of operations required to $\mathcal{O}(Nd\chi^3)$, which is far more efficient.
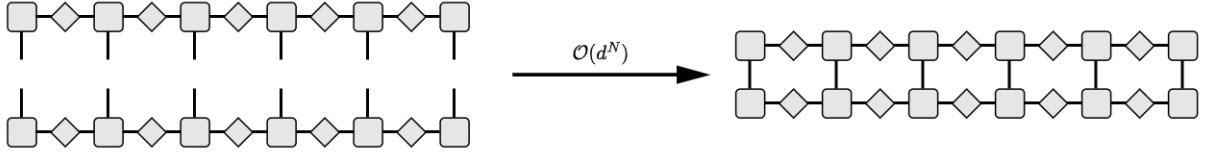
(a) Regular method of calculating overlaps between two states, which takes d^N operations.
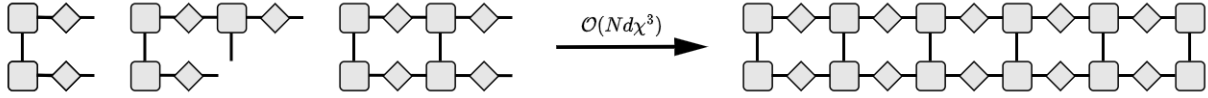
(b) The 'zip-up' method of calculating the overlap between two matrices, which takes $\mathcal{O}(Nd\chi^3)$ operations.

Figure 3.3: Two different methods of calculating the dot product between two states.

Next, let us consider the application of operators to a matrix product state. A useful property of the MPS formalism is that operators acting on a single-site j will only transform the Γ^{i_j} matrices. The operator $\hat{O}^{[j]}$ is a direct product of identities on the parts to the left and right of site j and hence leave these unchanged, and act with an operator $\hat{O}$ on site j. We denote the left and right parts as

$$\left|\eta_{\alpha_{j-1}}\right\rangle_{L_j} \equiv \sum_{i_1...i_{j-1}}^{d} \sum_{\alpha_1...\alpha_{j-2}} \Gamma^{i_1}_{\alpha_1} \Lambda^{[1]}_{\alpha_1} ... \Gamma^{i_{j-1}}_{\alpha_{j-2}\alpha_{j-1}} |i_1...i_{j-1}\rangle,$$

$$\left|\eta_{\alpha_j}\right\rangle_{R_j} \equiv \sum_{i_{j+1}...i_N}^{d} \sum_{\alpha_{j+1}...\alpha_{N-1}} \Gamma^{i_{j+1}}_{\alpha_j\alpha_{j+1}} \Lambda^{[j+1]}_{\alpha_{j+1}} ... \Gamma^{i_N}_{\alpha_{N-1}} |i_{j+1}...i_N\rangle,$$

and thus write our MPS as

$$|\psi\rangle = \sum_{i_j=1}^{d} \sum_{\alpha_{j-1}\alpha_j} \Lambda^{[j-1]}_{\alpha_{j-1}} \Gamma^{i_j}_{\alpha_{j-1}\alpha_j} \Lambda^{[j]}_{\alpha_j} \left|\eta_{\alpha_{j-1}}\right\rangle_{L_j} |i_j\rangle \left|\eta_{\alpha_j}\right\rangle_{R_j} \equiv \sum_{i_j=1}^{d} \sum_{\alpha_{j-1}\alpha_j} \Theta^{i_j}_{\alpha_{j-1}\alpha_j} \left|\eta_{\alpha_{j-1}}\right\rangle_{L_j} |i_j\rangle \left|\eta_{\alpha_j}\right\rangle_{R_j}. \quad (3.13)$$

The action of matrix elements $\langle i_j|\hat{O}_{i_j i'_j}|i'_j\rangle$ on this state yield

$$|\psi'\rangle = \sum_{i_j=1}^{d} \sum_{\alpha_{j-1}\alpha_j} \sum_{i'_j=1}^{d} \Theta^{i_j}_{\alpha_{j-1}\alpha_j} \langle i_j|\hat{O}_{i_j i'_j}|i'_j\rangle \left|\eta_{\alpha_{j-1}}\right\rangle_{L_j} |i_j\rangle \left|\eta_{\alpha_j}\right\rangle_{R_j} \equiv$$

$$\sum_{i'_j=1}^{d} \sum_{\alpha_{j-1}\alpha_j} \tilde{\Theta}^{i'_j}_{\alpha_{j-1}\alpha_j} \left|\eta_{\alpha_{j-1}}\right\rangle_{L_j} |i'_j\rangle \left|\eta_{\alpha_j}\right\rangle_{R_j}. \quad (3.14)$$

This new tensor $\tilde{\Theta}$ can be decomposed back into the familiar Γ, Λ matrices by inserting the identities $\Lambda^{[i-1]}(\Lambda^{[i-1]})^{-1}$ and $(\Lambda^{[i]})^{-1}\Lambda^{[i]}$ to its left and right, respectively, and defining

$$\tilde{\Gamma}^{i_j} \equiv (\Lambda^{[i-1]}_{\alpha_{j-1}})^{-1}\tilde{\Theta}^{i_j}_{\alpha_{j-1}\alpha_j}(\Lambda^{[i]}_{\alpha_j})^{-1}. \tag{3.15}$$

The application of a two-site operator acting on neighbouring sites is similar, but requires an additional operation to obtain the updated Γ and Λ matrices. After application of a two-site operator $\hat{O}^{[j,j+1]}$ we are left with a tensor $\tilde{\Theta}^{i_j i_{j+1}}_{\alpha_{j-1}\alpha^{j+1}}$ which we decompose using a singular value decomposition:

$$\tilde{\Theta}^{i_j i_{j+1}}_{\alpha_{j-1}\alpha^{j+1}} = U^{i_j}_{\alpha_{j-1}\alpha_j}\tilde{\Lambda}^{[j]}_{\alpha_j}(V^{i_{j+1}}_{\alpha_j\alpha_{j+1}})^{\dagger}. \tag{3.16}$$

After decomposing, we again insert the identities $\Lambda^{[i-1]}(\Lambda^{[i-1]})^{-1}$ and $(\Lambda^{[i+1]})^{-1}\Lambda^{[i+1]}$ to the left and right of sites j and $j+1$, which we contract into U and $V^{\dagger}$ respectively to obtain our new MPS,

$$\tilde{\Gamma}^{i_j} \equiv (\Lambda^{[i-1]}_{\alpha_{j-1}})^{-1}U^{i_j}_{\alpha_{j-1}\alpha_j} \qquad \tilde{\Gamma}^{i_{j+1}} \equiv (V^{i_j}_{\alpha_j\alpha_{j+1}})^{\dagger}(\Lambda^{[i+1]}_{\alpha_{j+1}})^{-1}. \tag{3.17}$$

The new Schmidt values on bond $[j]$ are given by the singular values in equation (3.16). Note that the number of nonzero Schmidt values on bond j can increase upon application of an operator, and thus an additional truncation step may be required. to maintain state normalisation one must then rescale the singular values by dividing them by the (Frobenius) norm of the truncated $\tilde{\Theta}$. The application of a two-site operator is represented graphically in figure 3.4. The contraction of the operator in equation (3.14) amounts to $\mathcal{O}(\chi^2 d^4)$ operations and the subsequent SVD requires $\mathcal{O}(\chi^2 d^3)$ operations.
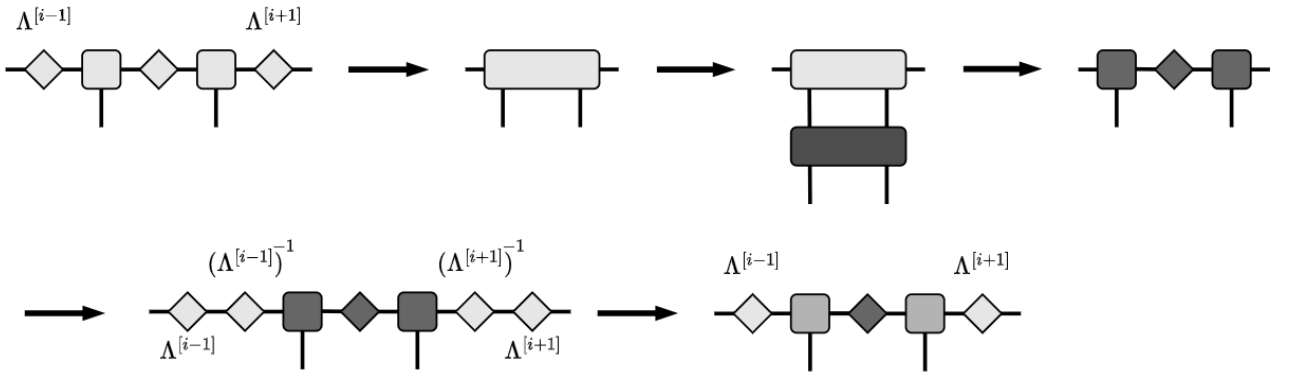
Figure 3.4: The procedure of applying a two-site operator to sites i and $i+1$ of an MPS. Shading of the tensors is used to show the difference between the initial and final Γ and Λ matrices.

Just as the application of single-site and two-site operators only involves the matrices related to those sites, the expectation values for the single-site and two-site operators are also only related to these matrices. Specifically, the expectation values are calculated as

$$\langle\psi|\hat{O}^{[j]}|\psi\rangle = \sum_{\alpha_{j-1}\alpha_j}\sum_{n_j}(\Theta^{\alpha_{j-1}\alpha_j}_{n_j})^{\dagger}\tilde{\Theta}^{\alpha_{j-1}\alpha_j}_{n_j} \tag{3.18}$$

$$\langle\psi|\hat{O}^{[j,j+1]}|\psi\rangle = \sum_{\alpha_{j-1}\alpha_{j+1}}\sum_{n_j n_{j+1}}(\Theta^{\alpha_{j-1}\alpha_{j+1}}_{n_j n_{j+1}})^{\dagger}\tilde{\Theta}^{\alpha_{j-1}\alpha_{j+1}}_{n_j n_{j+1}}. \tag{3.19}$$

3.2.2 Time-Evolving Block Decimation

Naturally, we are interested in how systems governed by particular Hamiltonians behave themselves as time progresses. We can construct the time-evolution operator from the Hamiltonian $\hat{H}$ as $\hat{U}(t) = \exp(-it\hat{H}/\hbar)$, which requires diagonalizing the Hamiltonian. This task becomes increasingly difficult for large system sizes, requiring the use of sparse-matrix diagonalization methods or exploitation of system symmetries. For matrix product states an efficient time integration algorithm was developed by Vidal in 2003 [64] for time-independent Hamiltonians with nearest neighbour interactions. This method was later called the *Time-Evolving Block Decimation* (TEBD) algorithm.

To start, let us review two facts about matrix exponentials. For a Hamiltonian consisting of two parts, $\hat{H} = \hat{H}_A + \hat{H}_B$, the time-evolution operator of this Hamiltonian can be written as ($\hbar = 1$):

$$e^{-it(\hat{H}_A+\hat{H}_B)} = e^{-it\hat{H}_A}e^{-it\hat{H}_B}, \qquad\qquad [\hat{H}_A, \hat{H}_B] = 0, \qquad\qquad (3.20)$$

$$e^{-it(\hat{H}_A+\hat{H}_B)} = e^{-it\hat{H}_A}e^{-it\hat{H}_B} + \mathcal{O}(t^2), \qquad\qquad [\hat{H}_A, \hat{H}_B] \neq 0. \qquad\qquad (3.21)$$

Equation (3.21) is called the (first order) *Suzuki-Trotter* approximation. Higher order approximations exist but will not be listed here. Now, consider a Hamiltonian that is a sum of single-site and nearest neighbour terms. This Hamiltonian can be written as a sum of exclusively nearest neighbour terms

$$\hat{H} = \sum_{j=1}^{N-1} \hat{H}^{[j,j+1]}, \qquad\qquad (3.22)$$

where single-site terms on site j are equally divided between $\hat{H}^{[j-1,j]}$ and $\hat{H}^{[j,j+1]}$. Overlapping terms, i.e. terms acting on a common site, generally do not commute:

$$[\hat{H}^{[j-1,j]}, \hat{H}^{[j,j+1]}] \neq 0, \qquad\qquad (3.23)$$

while terms that do not share sites always commute. Keeping this in mind, we see that grouping the terms on the right hand side of equation (3.22) into parts with even j and odd j divides it into two non-commuting parts that are individually comprised of commuting elements, $\hat{H} = \hat{H}_{\text{even}} + \hat{H}_{\text{odd}}$. Thus we can write the time-evolution operator of our Hamiltonian (3.22) as

$$\hat{U}(t) = \prod_{\substack{j=2 \\ j \text{ even}}}^{N-1} e^{-it\hat{H}^{[j,j+1]}} \prod_{\substack{j=1 \\ j \text{ odd}}}^{N-1} e^{-it\hat{H}^{[j,j+1]}} + \mathcal{O}(t^2), \qquad\qquad (3.24)$$

using only a single Suzuki-Trotter expansion. Thus, instead of having to diagonalize our full ($d^N \times d^N$) Hamiltonian, we can instead perform time evolution by consecutively applying $d-1$ two-site operators to our MPS. To reduce the integration error, it is prudent to numerically integrate the MPS by consecutively applying $\hat{U}(\Delta t)$ for small timesteps Δt. This time integration scheme is called time-evolving block decimation and is visualized in figure 3.5. Again, it is important to note that the number of Schmidt values may have increased after a TEBD sweep, meaning the matrices may have to be truncated back to dimension χ to keep calculations manageable, resulting in an additional error. Similar schemes can be devised for higher order Suzuki-Trotter approximations.
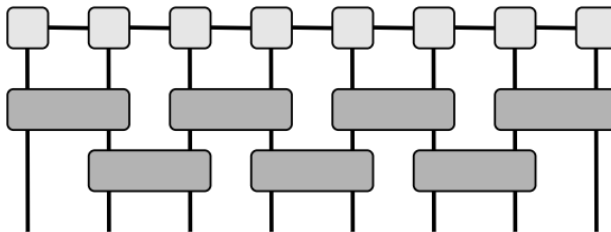
Figure 3.5: Schematic of a single TEBD sweep of a chain of 8 sites. Terms acting on a single-site are divided evenly between the even and odd operators acting on that specific site. The Λ matrices are omitted for convenience.

3.2.3 Longer-Range Interactions and Swap Gates

The TEBD scheme can be extended to accommodate longer-range interactions. In this subsection we will treat the application of a next-nearest neighbour coupling in the Hamiltonian, but the idea can be generalized to interactions over any distance. However, it is important to keep in mind that matrix product states are rely on rapidly decaying Schmidt values to remain efficient. Introducing long-range interactions to the model will naturally lead to higher correlation lengths during time evolution, meaning higher truncation parameters are required to accommodate for the greater degree of entanglement in the system.

With this in mind, let us turn to the implementation of next-nearest neighbour interactions between sites j and $j+2$. The most straightforward way to do this is by contracting sites j, $j+1$ and $j+2$ and adapting the

method described in subsection 3.2.1. However, this method becomes exponentially more expensive for longer distances. A different approach is through the use of SWAP-gates. A SWAP-gate is a two-site operator that flips the positions of sites j and $j+1$,

$$\hat{O}_{\mathbf{SWAP}}^{[j,j+1]} |i_j i_{j+1}\rangle = |i_{j+1} i_j\rangle. \tag{3.25}$$

Note that a SWAP-gate requires a singular value decomposition, since it is a two-site operator. To implement a next-nearest neighbour interaction between sites j and $j+2$, we can exchange the positions of sites j and $j+1$, implement the interaction as a nearest neighbour operator between the now-adjacent sites j and $j+2$ and perform another swap between $j+1$ and j to bring our MPS back to the correct ordering.

In situations where all sites are coupled to their next-nearest neighbours it is preferable to instead swap sites $j+1$ and $j+2$, since this allows us to apply the interactions between sites j and $j+2$ and sites $j+1$ and $j+3$ simultaneously, before swapping the sites back to their original positions. In figure 3.6 a TEBD-like scheme is presented for time-evolving a spin chain of 8 sites with nearest neighbour and next-nearest neighbour interactions.

The implementation of interactions over an arbitrary distance L is possible by performing $L-1$ swap operations to place the sites next to each other, performing the desired operation and moving the site back to its original position with another $L-1$ swap operations. Over longer distances this method can be desirable over simply contracting L MPS sites into a $\chi^2 d^L$ sized block, at a tradeoff of having to perform twice as many singular value decompositions.

3.2.4   TEBD Schemes for Jordan-Wigner Transformed Hubbard Models

The Jordan-Wigner transformed Hubbard model and spin-orbit terms given in equations (2.33) and (2.39) require a more involved TEBD scheme than the one presented in figure 3.5. These schemes are presented visually in figures 3.6 and 3.7. Note that in these figures each consecutive pair of sites maps to the up- and down spin occupations of the corresponding site in the Hubbard chain. Coloring of the physical indices is used to distinguish the physical site each index belongs to, spins with identically colored indices originate from the same site in the Hubbard chain. Thus, first the Coulomb interactions are applied, then the hopping terms and lastly the spin-orbit interactions. The dissipative terms are single-site and two-site operators which are applied after the TEBD sweep has been completed, but are not included in the diagram, where these would be on the very bottom. The schemes presented here use the lowest-order Suzuki-Trotter approximations. Higher order Suzuki-Trotter schemes exist and can be straightforwardly implemented at a computational cost. In this work, we have split the Lindbladian superoperator into a purely Hamiltonian part and a purely dissipative part which are applied separately. It turns out that this method does not guarantee the preservation of the positive semi-definiteness of the density matrix. A different operator-splitting method of the Lindbladian is proposed in [67], which preserves positive semi-definiteness for Suzuki-Trotter decompositions of first and second order. The method has been applied for simulating the Heisenberg-XXZ chain in [68], using the code created for this thesis. However, due to time constraints it has not been used in this work.

3.3   Matrix Product Density Operators

Entanglement discussed in the context of matrix product states is purely *internal*, that is, between the spins or particles of the system under consideration. Matrix product states in their regular form are restricted to describe pure states, but the formalism can be extended to allow for describing mixed states. A simple method to achieve this is by using purifications [69], which means to simply define the mixed state of the system as a pure state of a larger Hilbert space. It is also possible to simulate the density matrix of a system directly as a matrix product operator (MPO), the extension of the MPS formalism to operator space. The MPO of a density matrix is also called a matrix product density operator, or MPDO. Since we will be working with the Lindblad equation, which is a master equation for the density matrix, it is a natural choice to work with the MPDO formalism instead of using purification. We refer to [59] for further reading on simulating Lindbladian dynamics using the purification approach.

Let us start by creating a MPDO from a MPS. The density matrix of a pure state is given as $\rho = |\psi\rangle \langle\psi| = |\psi\rangle \otimes \langle\psi|$. Let $|\psi\rangle$ be described by a MPS in Vidal notation with matrices $\{\Gamma_{\alpha_{j-1}\alpha_j}^{i_j}, \Lambda_{\alpha_j}^{[j]}\}$. Obtaining the MPDO of this state is straightforward: we take the outer product of each matrix with the complex conjugate of itself and define those to be our new Γ and Λ matrices,

$$\tilde{\Gamma}_{(\alpha_{j-1}\alpha'_{j-1})(\alpha_j\alpha'_j)}^{i_j i'_j} \equiv \Gamma_{\alpha_{j-1}\alpha_j}^{i_j} \otimes (\Gamma_{\alpha'_{j-1}\alpha'_j}^{i'_j})^* \tag{3.26}$$

$$\tilde{\Lambda}_{(\alpha_j\alpha'_j)}^{[j]} \equiv \Lambda_{\alpha_j}^{[j]} \otimes \Lambda_{\alpha'_j}^{[j]}. \tag{3.27}$$
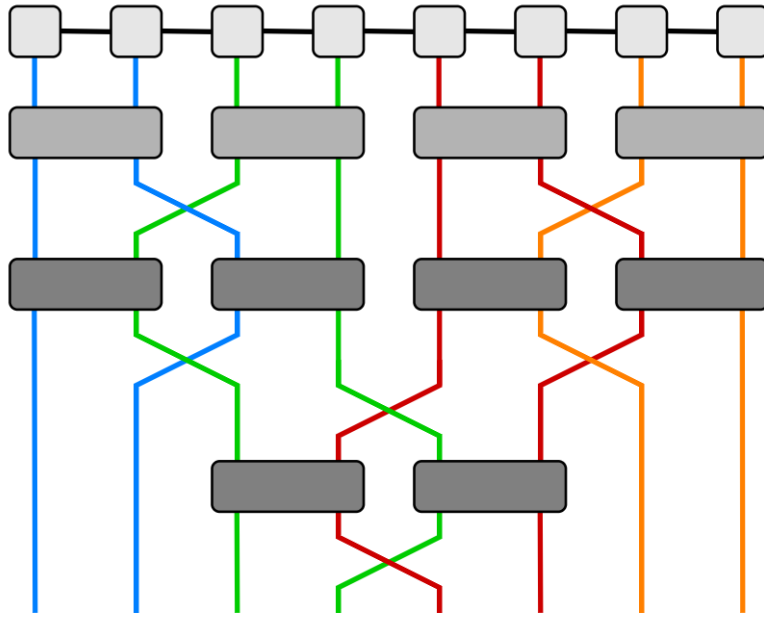
Figure 3.6: TEBD scheme for the Jordan-Wigner transformed Hubbard model, which involves the application of next-nearest neighbour interaction by making use of SWAP-gates. First the Coulomb interactions between spins on the same Hubbard site are applied, then the hopping terms between the Hubbard sites are applied by making use of SWAP-gates. The color of the physical indices denotes the site on the Hubbard chain. The single-site operators that apply the dissipative part of the Lindblad equation are not included in this figure. The shorter MPS notation of figure 3.2 is used for convenience.
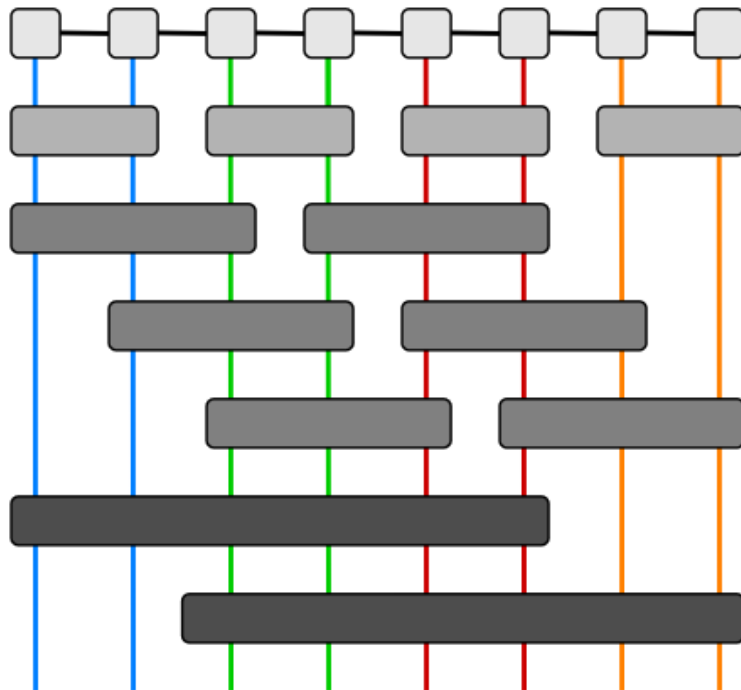
Figure 3.7: TEBD scheme for the Jordan-Wigner transformed Hubbard model with spin-orbit interactions. Due to the fermionic anticommutation relations, the Jordan-Wigner transformed interactions between distant sites cannot be implemented using SWAP operations, as nontrivial operators act on the sites in between the sites involved in the hopping and spin-orbit coupling terms. Refer to sections 2.3 and 2.4 for details.

This procedure is mathematically equivalent to giving each tensor an additional 'auxiliary index' of dimension 1 and contracting each pair of matrices over this index [70]. The bond indices inside the parentheses are grouped together as a single index, leaving us with the expression of our matrix product operator. However, as pointed out by Zwolak and Vidal [71], it is possible to create a one-to-one map from a $d \times d$ density matrix to a d^2 vector, which is formally known as Choi-Jamialkowski's isomorphism [72]. We can treat this vector as a state vector, dubbed a 'superket' by Zwolak and Vidal. Simply put, we can group together the upper indices $i_j i'_j$ in equation (3.26) as a single index [70] (although this will have consequences which we will discuss in section 3.3.2). Importantly, vectorising the density matrix allows us to write the MPDO of the density matrix $\rho = |\psi\rangle \langle\psi|$ as a regular MPS. We will denote the superket of ρ as $|\rho\rangle\rangle$, which has the form

$$\rho = \sum_{i,j} p_{ij} |i\rangle \langle j| \quad \leftrightarrow \quad |\rho\rangle\rangle = \sum_{i,j} p_{ij} |i\rangle \otimes |j\rangle. \tag{3.28}$$

For a graphical representation of the construction of $|\rho\rangle\rangle$ see figure 3.8. We will drop the tildes over the Γ and Λ matrices for the sake of readability. As a final remark, it should be noted that by construction the singular values in the new Λ matrix are not necessarily ranked in decreasing order, which is the convention we adopted. We will therefore reorder the singular values in each Λ matrix to decreasing order and rearrange the rows and columns in the corresponding Γ matrices to the left and right accordingly.
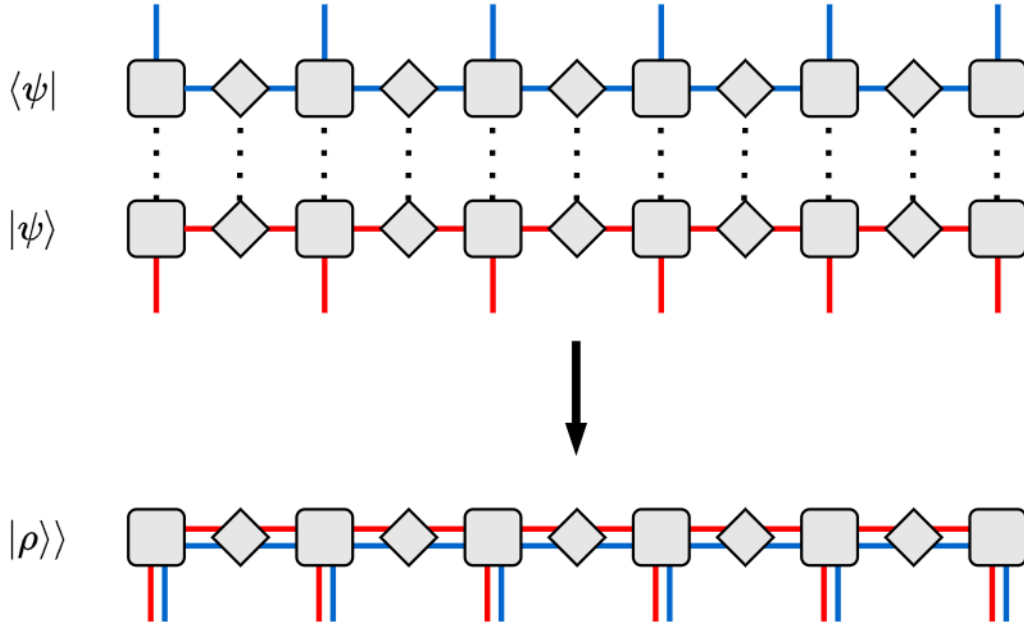
Figure 3.8: Schematic representation of the creation of the vectorised MPDO through the contraction of each site tensor with its own complex conjugate over a one-dimensional auxiliary index. The corresponding Schmidt indices and physical indices are grouped together such that the tensors are of the same order as a regular MPS. This procedure is equivalent to taking the tensor product of each tensor with its own complex conjugate.

3.3.1 The Lindblad Equation for vectorised Density Matrices

vectorising the density matrix comes with a few implications to the calculation of expectation values and the application of operators. For the calculation of expectation values we make use of the vectorised form of the Hilbert-Schmidt inner product for operators $\hat{A}$ and $\hat{B}$:

$$\langle \hat{A}, \hat{B} \rangle_{\mathrm{HS}} \equiv \mathrm{Tr}(\hat{A}^\dagger \hat{B}) = \langle\langle \hat{A} | \hat{B} \rangle\rangle. \tag{3.29}$$

We can use this relation to calculate the trace of ρ and the expectation of operators:

$$\mathrm{Tr}(\rho) = \mathrm{Tr}(\mathbb{I}\rho) = \langle\langle \mathbb{I} | \rho \rangle\rangle \qquad \qquad \langle \hat{A} \rangle = \mathrm{Tr}(\hat{A}\rho) = \mathrm{Tr}(\rho \hat{A}) = \langle\langle \rho | \hat{A} \rangle\rangle, \tag{3.30}$$

which are essentially equivalent operations. For the right equation we make use of the fact that ρ is Hermitian and that the trace is cyclical.

In order to obtain the Lindblad equation for $|\rho\rangle\rangle$ we need the vectorised forms of the left and right actions of matrices on each other, which are

$$|\hat{A}\hat{B}\rangle\rangle = (\hat{A} \otimes \mathbb{I})|\hat{B}\rangle\rangle = (\mathbb{I} \otimes \hat{B}^{\mathrm{T}})|\hat{A}\rangle\rangle. \tag{3.31}$$

The derivations of equations (3.29) and (3.31) are presented in [73].

Using equation (3.31) we find the vectorised Von Neumann equation:

$$\frac{d}{dt}\rho = -\frac{\mathrm{i}}{\hbar}(\hat{H}\rho - \rho\hat{H}) \quad \leftrightarrow \quad \frac{d}{dt}|\rho\rangle\rangle = -\frac{\mathrm{i}}{\hbar}(\hat{H} \otimes \mathbb{I} - \mathbb{I} \otimes \hat{H}^{\mathrm{T}})|\rho\rangle\rangle. \tag{3.32}$$

A convenient consequence of using vectorised density matrices is the fact that we have reduced the commutator between $\hat{H}$ and ρ to the action of an operator which acts from the left of ρ. We can do exactly the same for the dissipative part of the Lindblad equation (recall we had incorporated the coupling strengths γ_k in the definitions of $\hat{L}_k$ in equation (1.16), hence it is omitted here),

$$\hat{\mathcal{D}}(\rho) = \sum_k \left(\hat{L}_k \rho_S \hat{L}_k^\dagger - \frac{1}{2}\{\hat{L}_k^\dagger \hat{L}_k, \rho_S\}\right)$$

$$\leftrightarrow \tag{3.33}$$

$$\hat{\mathcal{D}}|\rho\rangle\rangle = \sum_k \left(\hat{L}_k \otimes (\hat{L}_k^\dagger)^{\mathrm{T}} - \frac{\hat{L}_k^\dagger \hat{L}_k \otimes \mathbb{I} + \mathbb{I} \otimes (\hat{L}_k^\dagger \hat{L}_k)^{\mathrm{T}}}{2}\right)|\rho\rangle\rangle,$$

where we used that the vectorised form of a product of three matrices $\hat{A}\hat{B}\hat{C}$ reads $(\hat{A} \otimes \mathbb{I})(\mathbb{I} \otimes \hat{C}^{\mathrm{T}})|\hat{B}\rangle\rangle = \hat{A} \otimes \hat{C}^{\mathrm{T}}|\hat{B}\rangle\rangle$.

By combining relations (3.32) and (3.33) we see that we have reduced the Lindblad equation, which involved actions on the left *and* right of ρ, to the left-action of a single superoperator on the superket $|\rho\rangle\rangle$. We can therefore write down a closed form solution for $|\rho\rangle\rangle$,

$$|\rho(t)\rangle\rangle = \exp\left(-\frac{\mathrm{i}t}{\hbar}(\hat{H} \otimes \mathbb{I} - \mathbb{I} \otimes \hat{H}^{\mathrm{T}}) + t\sum_k \left(\hat{L}_k \otimes (\hat{L}_k^\dagger)^{\mathrm{T}} - \frac{\hat{L}_k^\dagger \hat{L}_k \otimes \mathbb{I} + \mathbb{I} \otimes (\hat{L}_k^\dagger \hat{L}_k)^{\mathrm{T}}}{2}\right)\right)|\rho(0)\rangle\rangle. \tag{3.34}$$

3.3.2 Additional Considerations in the MPDO Formalism

There are some final issues for vectorised MDPOs that must be addressed. Chief among these is the preservation of the norm and the trace of our MPDO. Here we understand the term 'MPDO' as the MPS formulation of a vectorised density matrix. In the regular MPS formalism, the normalisation of a quantum state $|\psi\rangle$ must be maintained over time evolution, i.e. we have a normalisation condition $\langle\psi|\psi\rangle = 1$. For a density matrix we have instead the condition $\mathrm{Tr}(\rho) = 1$, which translates to $\langle\langle\mathbb{I}|\rho\rangle\rangle$ in the MPDO formulation. However, in literature there are conflicting notions on what the normalisation condition for $|\rho\rangle\rangle$ should be. Some mention the normalisation condition to simply be $\mathrm{Tr}(\rho) = \langle\langle\mathbb{I}|\rho\rangle\rangle = 1$ [66, 72], while others state that the normalisation condition should be $\langle\langle\rho|\rho\rangle\rangle = 1$ [74, 75]. In the latter case, the trace condition of the density matrix is no longer enforced; the situation can occur that $\mathrm{Tr}(\rho) = \langle\langle\mathbb{I}|\rho\rangle\rangle \neq 1$. In these works this is accounted for by rescaling the expectation values by the trace of the density matrix,

$$\langle\hat{A}\rangle = \frac{\mathrm{Tr}(\hat{A}\rho)}{\mathrm{Tr}(\rho)} = \frac{\langle\langle\mathbb{I}|\hat{A}|\rho\rangle\rangle}{\langle\langle\mathbb{I}|\rho\rangle\rangle}, \qquad \text{if the normalisation condition is } \langle\langle\rho|\rho\rangle\rangle = 1. \tag{3.35}$$

This effectively translates to taking

$$\langle\hat{A}\rangle = \mathrm{Tr}\left(\hat{A}\frac{\rho}{\mathrm{Tr}(\rho)}\right), \tag{3.36}$$

and hence is essentially equivalent to enforcing $\langle\langle\mathbb{I}|\rho\rangle\rangle = 1$. In this work we will enforce the normalisation condition $\langle\langle\rho|\rho\rangle\rangle = 1$.

A second important issue, and a rather unfortunate one, is the fact that MPDOs do not benefit from efficient method of calculating expectation values presented in equation (3.18). Let us treat this computation in a bit more detail. Consider the calculation of the expectation value of an operator $\hat{O}^{[j]}$ on site j. We can write our MPS in a combination of right-canonical, left-canonical and Vidal decompositions (neglecting the bond indices),

$$|\psi\rangle = \sum_{i_1...i_N}^{d} A^{i_1} ... A^{i_{j-1}} \Lambda^{[j]} \Gamma^{i_j} \Lambda^{[j+1]} B^{i_{j+1}} ... B^{i_N}. \tag{3.37}$$

We would normally contract $\Lambda^{[j]}\, \Gamma^{i_j}\, \Lambda^{[j+1]}$, apply our operator $\hat{O}^{[j]}$ and compute the overlap with the original state $|\psi\rangle$, as was described in equation (3.18). When computing the overlap, we make use of the fact that the A and B matrices are right- and left normalised respectively, meaning the parts to the left and right reduce to identity matrices. Thus, the expectation value $\langle \hat{O}^{[j]} \rangle$ only depends on the parts affected by the action of $\hat{O}^{[j]}$: $\Lambda^{[j]}\, \Gamma^{i_j}\, \Lambda^{[j+1]}$. In the MPDO formalism we instead take the trace, which translates into calculating the overlap with $|\mathbb{I}\rangle\rangle$. We therefore cannot make use of the fact that $A^\dagger A = B B^\dagger = \mathbb{I}$, and instead are forced to contract the entire chain to calculate $\langle \hat{O} \rangle$ [70].

As a final point we must adress the difference between MPDOs and purifications. State purification is the notion that a mixed state can be written as a pure state defined in a larger Hilbert space. Specifically, any mixed state of a system with a Hilbert space $\mathcal{H}_S$ of dimension d can be described as a pure state in a Hilbert space $\mathcal{H}_U = \mathcal{H}_S \otimes \mathcal{H}_A$ that is at most dimension d^2 [69]. The space $\mathcal{H}_A$ is called an *ancillary Hilbert space*, which serves to introduce additional degrees of freedom that represent the bath our system is entangled with. If the state is described by a density matrix ρ, then we can describe the system as a pure state with any ket $|\psi\rangle \in \mathcal{H}_U$ under the condition that $\rho = \text{Tr}_A(|\psi\rangle \langle \psi|)$. As long as this condition is met, we can take $\mathcal{H}_A$ to be any size, but it can be shown that taking $\dim(\mathcal{H}_A) = d$ is sufficient to purify any mixed state. As a proof, we take $\mathcal{H}_A$ to be a copy of $\mathcal{H}_S$ and take as our purification the superket $|\rho\rangle\rangle$ normalised under the Euclidean norm,

$$|\psi\rangle = \frac{|\rho\rangle\rangle}{\langle\langle\rho|\rho\rangle\rangle}. \tag{3.38}$$

This state satisfies $\text{Tr}_A(|\psi\rangle \langle \psi|) = \rho$ and hence is a valid purification, of size d^2. Since purifications are always pure states we can decompose the purification $|\psi\rangle$ into a regular MPS, which we will call a *locally purified tensor network*, or LPTN. This method of representing mixed states using tensor networks was first proposed by Verstraete et al. in [76].

We see that the purification of mixed states and vectorisation of density matrices are remarkably similar, but not identical. For one, the purification of ρ is not unique. Moreover, we may also find purifications with dimension *lower* than d^2, if the system is in a suitable state. Lastly, the Hamiltonian dynamics of purifications do not have to adhere to equation (3.32) as long as the physical part of the Hilbert space evolves according to $\hat{H}_S$, because the ancillary degrees of freedom are traced out when calculating expectation values.

In tensor network form there are some additional differences between purified states (LPTNs) and vectorised density matrices (MPDOs). Since LPTNs describe pure states, they benefit from some features that MPDOs do not, such as the gauge freedom when calculating expectation values, allowing fast calculation of expectation values such as in equation (3.18). Moreover, positivity of the state is ensured for LPTNs while this is not the case for MPDOs [59]. In 2018, Jaschke and coworkers compared different tensor-network based approaches for simulating open quantum systems, including the LPTN and MPDO methods [70]. In this study, it was concluded that the MPDO approach in combination with TEBD was the best method for studying the dissipative dynamics of an exciton, described by the Lindblad equation, despite the aforementioned computational advantages offered by LPTN over MPDO[1]. This assessment was based on the findings that the error of the LPTN method was higher, especially in the long-time limit (which is what we are interested in) and the fact that it required more numerical resources than the MPDO method. In this work, we have chosen to work with the MPDO method due to the easy implementation of the time evolution in this framework. The results obtained using the method of this thesis will be compared to results obtained with the LPTN method in section 4.1.

---

[1]LPTN was deemed the more effective method for finding thermal states, however.

4 Results

4.1 The Spin-1/2 XXZ-Heisenberg Chain

We will begin by studying the results of the anisotropic Heisenberg XXZ model. The nonequilibirum steady states (NESS) were achieved using the regular TEBD scheme of figure 3.5 with dissipative Lindblad terms at both ends of the chain. The results are compared to those of Prosen and Žnidarič [61] and of Werner et al. [59]. In figure 4.1a, the spin profiles of the NESS of a chain of 50 sites are shown for for anisotropy parameters $\Delta = 0.5, 1, 1.5$. The results show a clear correspondence with the results in figure 3 of [59], which show the spin profiles for chains of $N = 100$ and $\Delta = 1, 1.5$. The transition from the up-polarised to down-polarised parts of the chain is slightly sharper in the results of Werner et al., which can be a consequence of the shorter chain lengths used in this thesis. In the NESS of $\Delta = 0.5$ we see an alternating pattern where the nearest neighbours in the bulk of the system (far away from the edges) have not converged to the same magnetisation. Instead, next nearest neighbours of odd numbered sites (with counting starting from 0) converge to a small positive $\langle \hat{\sigma}_z \rangle$ while the even numbered sites converge to a negative $\langle \hat{\sigma}_z \rangle$, with approximately the same absolute value for both. The magnitude of the alternating polarisations decreases for lower dt indicating this to be a numerical error. The highest 75 singular values (Schmidt values) between sites 24 and 25 of the NESS for $\Delta = 1$ are shown in figure 4.1b. A clear exponential decay in singular values is visible, meaning the NESS can be efficiently described using matrix product states.

(a)   (b)
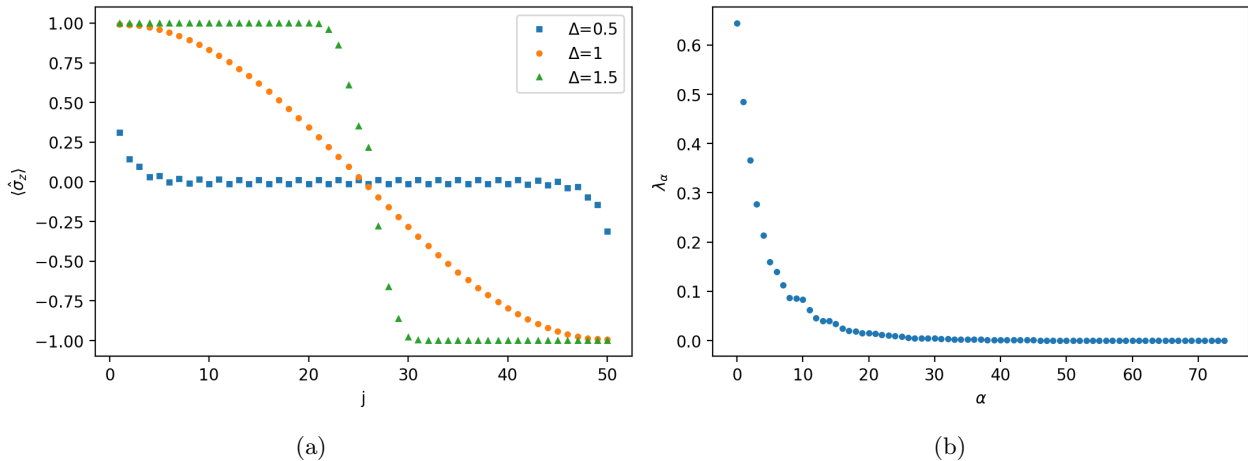
Figure 4.1: (a) Spin profile of the NESS of a chain of 50 sites for different anisotropy parameters. (b) Singular values between sites 24 and 25 of the NESS of an isotropic Heisenberg model ($\Delta = 1$) of 50 sites. A clear exponential decay is visible indicating this state can be efficiently described using matrix product states.

The spin current through the (middle site of the) chain in the steady state is shown for different chain lengths and for anisotropy parameters $\Delta = 0.5, 1$, together with the analytical results from [61], in figure 4.2a. The results closely follow the analytical value of the current. However, an important remark must be made here. It turns out that the current into the middle site is not equal to the spin current out of the middle site in the steady state, while the expected magnetisation of the site remains constant. Throughout the entire chain the currents through the bonds alternate: the current through bond i is equal to that through bond $i + 2$, while the current through bond $i + 1$ is lower, but equal to the current through bond $i + 3$. This result is, of course, not physical as it is in contradiction with the continuity equation for the spin current, and appears to be a numerical error resulting from the Suzuki-Trotter decomposition. Even though the currents into and out of a given site are not equal, it can be seen in figure 4.2b that the difference between these two currents decreases with timestep size. Similarly, the average of the in-current and out-current is independent of the timestep size dt and appears to be the point the in and out currents converge to. Thus, this discrepancy is assumed to be a consequence of finite size of our timesteps. The currents shown in figure 4.2a are the averages of the currents into and out of the middle site of the steady state for $dt = 0.02$. Furthermore, the average currents are equal for all sites, which is required by current continuity. The average currents correspond closely to the analytical solution. For $\Delta = 1$ the results of this work, obtained using the MPDO approach, are closer to the analytical solution than the numerical results found by Werner et al. [59] using the LPTN approach mentioned in section 3.3.2. For $\Delta = 0.5$ there is no discernible difference between the two methods.
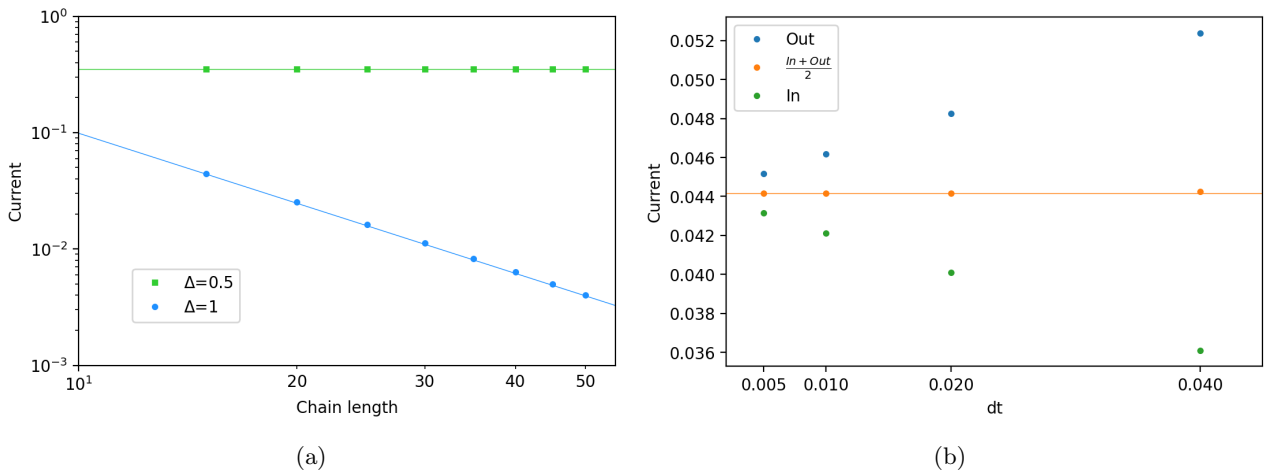
Figure 4.2: (a) The steady state spin current through spin chains of varying lengths for different anisotropy parameters. The plotted lines indicate the exact solution of the steady state current through the system as derived in [61]. The plotted currents are the average of the currents into and out of the middle site of the chain, which are not equal as is shown in the second figure. (b) The difference between the current into and out of the middle site of a chain of $N = 15$ sites for different timestep sizes. The difference decreases with smaller timesteps, and both currents appear to converge to the intermediate value, which is roughly same for all values of dt. The horizontal line denotes the intermediate value of the current for $dt = 0.005$.

4.2   The Hubbard Chain

Let us now discuss the results of the Jordan-Wigner transformed Hubbard model. In this section, we will compare our results with those of Prosen and Žnidarič [54], who have studied this exact model with the same approach used in this thesis. In figures 4.3a and 4.3c the average on-site occupations for chains comprising of 16 and 32 sites are shown for different Coulomb interaction strengths. In figures 4.3b and 4.3d the corresponding on-site correlations between spin-up and spin-down fermion occupations are presented, which is defined as $\langle n_{j\uparrow}n_{j\downarrow}\rangle_c = \langle n_{j\uparrow}n_{j\downarrow}\rangle - \langle n_{j\uparrow}\rangle\langle n_{j\downarrow}\rangle$. The occupation profiles of the Hubbard chains follow the same behaviour as the results in [54]: they are linear in the bulk with jumps at the boundaries, and get progressively more flat for lower Coulomb interaction strengths. The discontinuities of the occupation profiles at the boundaries are explained in [54] as the result of boundary resistances which are present due to 'over-simplified Lindblad operators'. The spin-up/spin-down density-density correlation profiles are relatively similar to, but less accurate than, the ones obtained in [54].

In [54] it is stated that truncation up to $\chi = 80$ was sufficient to obtain the results (see reference 18). The code developed for this work was not able to reproduce these results for similar χ. Simulations have been done for $L = 32$, $U = 0.5$ with truncation parameter up to $\chi = 150$, as simulations using lower χ values did not converge to the NESS. To better understand what exactly prevents us from obtaining the steady states for lower values of χ it is instructive to look at the entanglement in the chain over time.

As discussed in section 3.1.2, matrix product states require a state to be lightly entangled in order to be an effective approximation method. Entanglement is a property which we quantify using the von Neumann entanglement entropy (VNEE) defined in equation (3.3). In figure 4.4 the singular values between sites 4 and 5, the Schmidt values of a Schmidt decomposition through the middle of the system, are presented for both coherent and dissipative dynamics. It can be immediately seen that the NESS is lightly entangled and can be efficiently described using matrix product states, while this is not the case for the state obtained after an equally long time evolution governed exclusively by the Hubbard Hamiltonian. In figure 4.5a the von Neumann entanglement entropy of all possible bipartitions of the chain over time is presented. As was predicted in section 3.1.2, the system initially exhibits a steep increase in entanglement entropy caused by the fact that the bulk dynamics of the system is predominantly governed by the Hamiltonian. The entropy then decreases as the dissipation at the edges starts to dominate, and eventually stabilises at a low value. The entanglement entropy of the NESS is dependent on the bath parameter ν characterising the average bath filling, as seen in figure 4.5b.

In figure 4.6a a similar figure is presented for a Hubbard chain of $L = 24$ sites (48 spin sites) for selected bipartitions of the system. Here we see again an initial steep rise in entanglement which eventually plateaus and remains relatively constant with small, seemingly random, variations. Eventually, the entanglement entropy drops swiftly and stabilises at a low value, at which point the state has converged to the NESS. In simulations

(a)

(b)

(c)

(d)
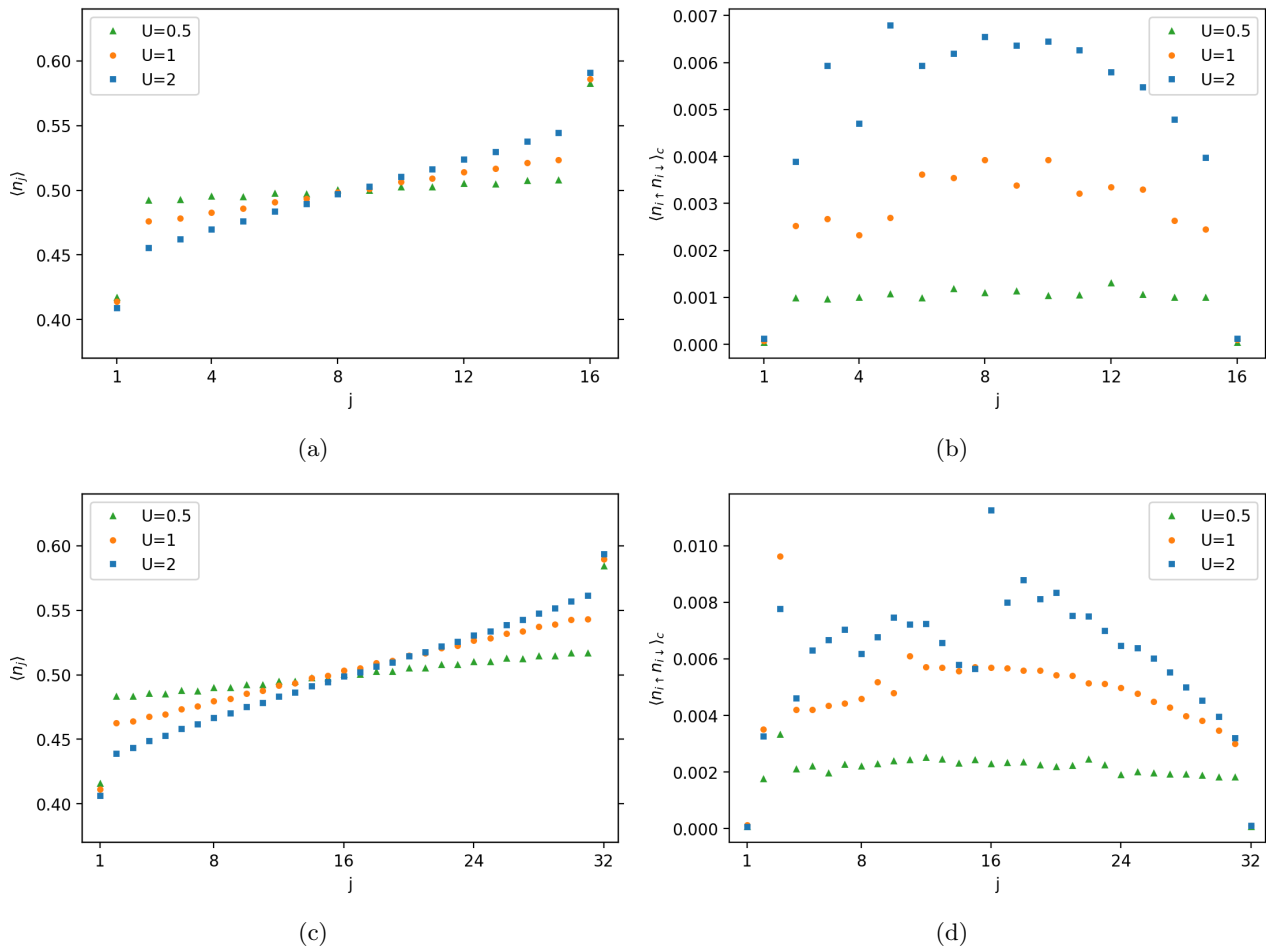
Figure 4.3: (a, c) Occupation and (b, d) corresponding spin-up/spin-down correlation profiles of a chain of length $L = 16$ and $L = 32$ for Coulomb interaction strengths $U = 0.5$, 1, 2, with $t = 1$ in all cases. The bath parameter was set to $\nu = 0.2$ (see equation (2.34)), which corresponds to equilibrium densities of 0.4 and 0.6 in the left and right reservoirs, respectively. Results were obtained with truncation parameter $\chi = 90$ for $L = 16$ and χ up to 150 for $L = 32$.

where the truncation parameter χ is not sufficiently large the entanglement structure remains in the plateau-phase; the system does not converge to a steady state with low entanglement. While the system is in this plateau phase the MPS does not describe a physical state since the expected occupations $\langle \hat{n}_i \rangle$ assume values outside the physically allowed $[0, 1]$ range. The difference between figures 4.6a and 4.6b demonstrates the importance of the truncation parameter to the simulation convergence. The high χ required for simulation convergence stands in stark contrast with the results of [54], obtained using $\chi \leq 80$. It is possible that the authors of [54] applied additional techniques to ensure convergence to the NESS with low χ which are not stated in the paper, for example by using specific initial states. The authors of [54] did not respond to attempts to make contact. Nevertheless, system sizes of $L < 16$ are already sufficient for the study of spin-selective transport and hence the method appears suitable for the purposes of this thesis.

(a)   (b)
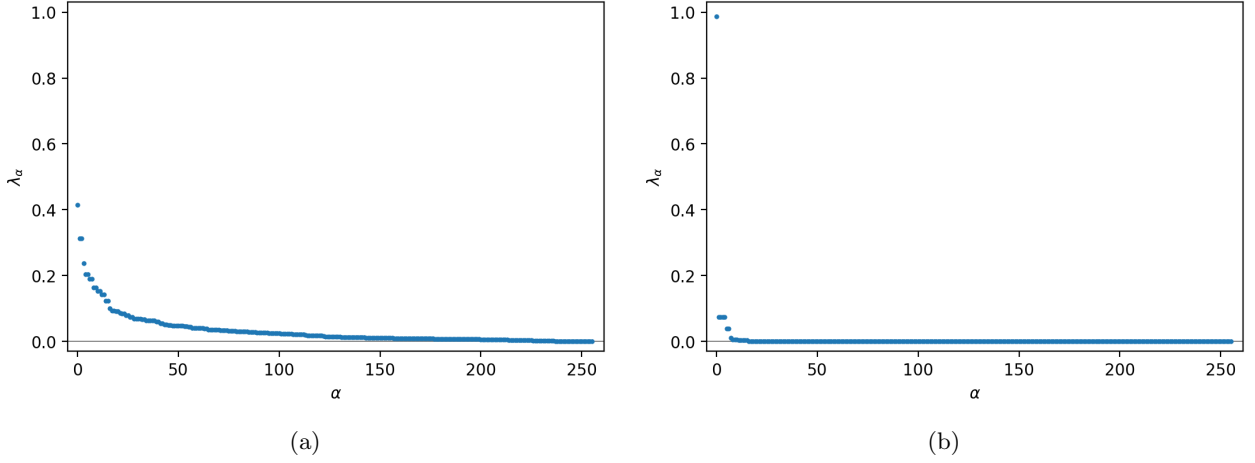
Figure 4.4: Singular values between sites 4 and 5 ($\Lambda^{[4]}$) of a chain of $N = 8$ sites at $t = 60$, for (a) coherent dynamics and (b) dissipative dynamics. In figure (b) the system has converged to the NESS.

(a)   (b)
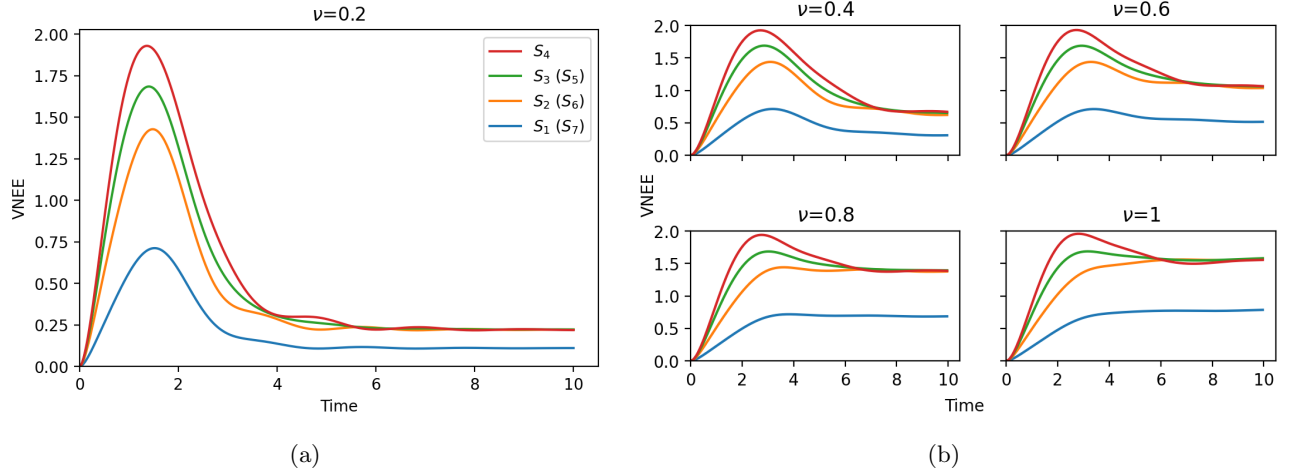
Figure 4.5: Von Neumann entanglement entropy (VNEE) over time for different bipartitions of a chain of $N = 8$ sites with dissipative time evolution. The entanglement entropy is symmetric with respect to the left and right parts of the chain. Steady state entanglement is seen to be dependent on the bath parameter ν.

(a) $\chi = 90$.   (b) $\chi = 60$.
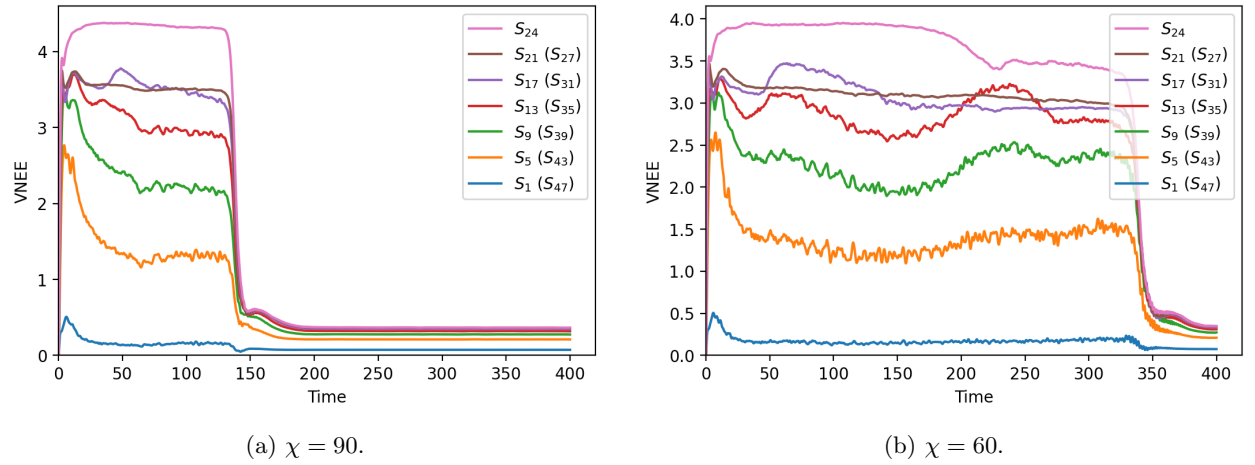
Figure 4.6: Von Neumann entanglement entropy (VNEE) over time for different bipartitions of a chain of $N = 24$ sites with dissipative time evolution. The steep drop coincides with the convergence of the state to the NESS. The convergence time is seen to be related to the truncation parameter χ.

(a)	(b)
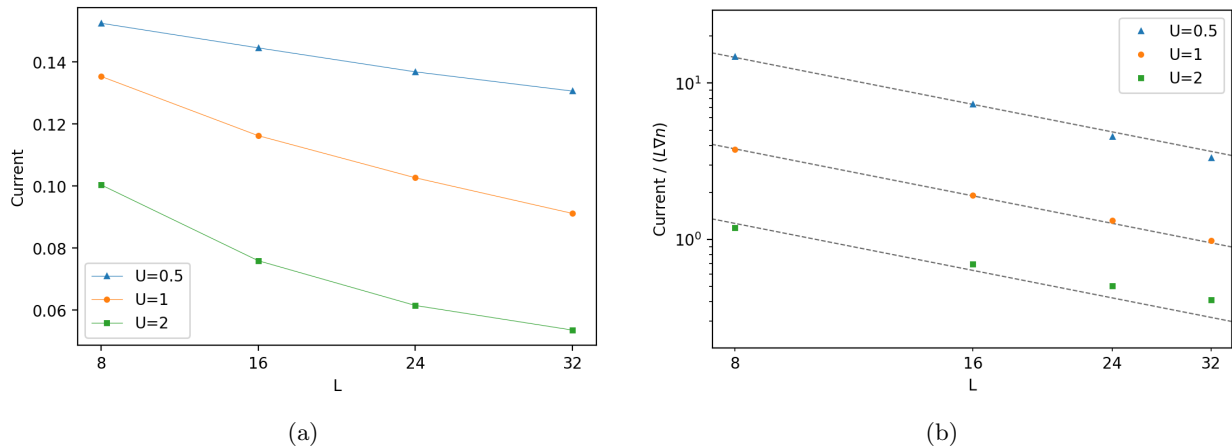
Figure 4.7: (a) Current through the middle bond of Hubbard model, as defined by equation (2.14), for Coulomb interaction strengths $U = 0.5, 1, 2$, with $t = 1$ and $\nu = 0.2$ in all cases. (b) Log-log plot of the currents divided by the extrapolated density drop $L\nabla n$. ∇n is defined as the linear coefficient of the bulk density profiles, see figure 4.3. Dashed lines indicate $\frac{a}{L}$ scaling. The constant a was found to be 30.4 for $U = 1$, identical to the value reported in [54].

To conclude this section, let us examine the current through the Hubbard model. In figure 4.7a the steady-state electron current through the system is presented for different values of U. Prosen and Žnidarič provide results for the current rescaled by the density drop $L\nabla n$ in figure 2, where ∇n is the linear coefficient of the density profile obtained by fitting a linear function to the bulk density profile (i.e. excluding the edge sites). This figure has been reconstructed and is shown in figure 4.7b. The dashed lines represent a scaling of $\frac{a}{L}$. For $U = 1$ we have $a = 30.4$, the same as found by Prosen and Žnidarič.

In the current calculations for the spin-1/2 Heisenberg chain we encountered a numerical error which resulted in an alternation of the currents for consecutive bonds, where the steady state current through the even bonds consistently differed from the current through the odd bonds, in contradiction with the continuity of the spin flow, see figure 4.2b. The current profile through each bond for $L = 8$, $U = 1$ is shown in figure 4.8a. The result of bond $j = 4$ is used in figure 4.7. The current through the bonds in the bulk of the system appear to be relatively, but not exactly, equal, while the currents through the bonds between the bulk and the boundary sites are significantly lower. Note that this figure only includes the currents inside the system, and not the currents between the system and the baths. In [54], it is stated that the current through the NESS is independent of the site, as is required by current continuity.

In figure 4.8b the steady-state current profile for $L = 4$, $U = 1$ is shown for different timestep sizes. The difference between the bulk current and the currents between bulk and edge sites is seen to decrease with the timestep, again indicating that the lack of of current continuity is due to a numerical error. We also observe that the spin-up and spin-down electron currents are not exactly equal, even though the system should be perfectly spin-symmetric. These differences are of the order 10^{-4} compared to the total currents, and do not appear to decrease with the timestep size.

(a)	(b)
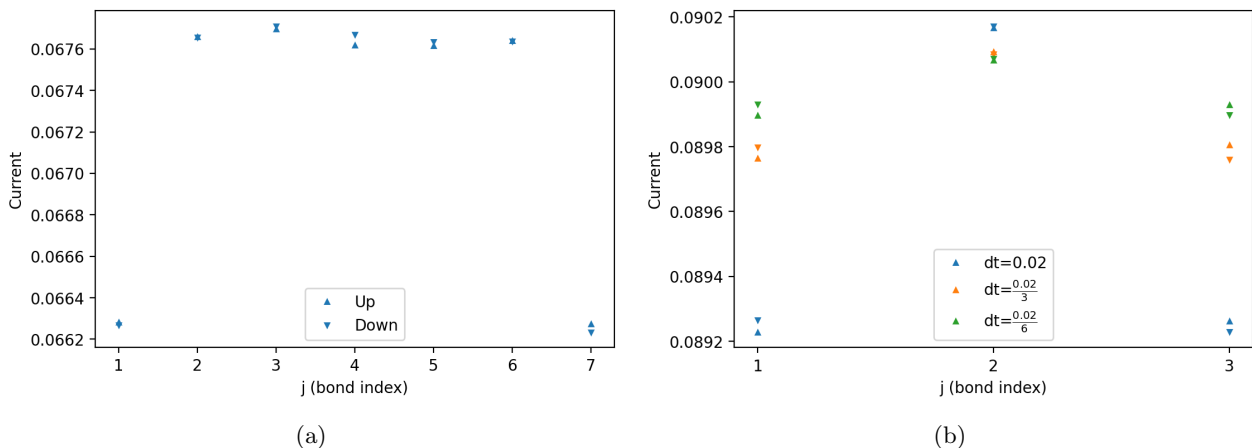
Figure 4.8: The steady-state current profile for each bond in the system for chain lengths $L = 8$ and $L = 4$. By continuity (see equation (2.15)), these should all be equal to preserve particle conservation. In figure (b), the discrepancy in the currents is seen to decrease for smaller timestep sizes dt.

35

4.3 The Hubbard Chain with Next-Nearest Neighbour Spin-Orbit Interactions

We have examined the capability of the MPS method to simulate the Hubbard model for chains of up to $L = 32$ sites by comparing the results to a previous study by Prosen and Žnidarič, that employs a similar method [54]. We have seen that our method reproduces the results of [54] with comparable accuracy. Despite the fact that our model requires a higher truncation parameter χ (in order to account for the high entanglement in the transient regime), this means that the minimum system size $L = 4$, for which our system should exhibit spin-selectivity in electron transport, is well within the method's capability.

In view of the limited time available for this thesis project, emphasis has been placed on verifying whether the model reproduces the CISS effect, that is, whether it exhibits a finite magnetocurrent, and whether the results follow the expected behaviour in the linear and in the non-interacting regimes. Further interesting topics which could be addressed in a future study include the behaviour of the model in different parameter regimes, the effect of molecular length and chemical potential on measured magnetoresistance, the dependence of the results on the two main numerical parameters χ and dt and the effect of different operator-splitting methods of the Lindblad equation on the quality of the results.

Let us first discuss the parameters which are important for our simulations, and how the magnetocurrent through the system will be presented in the results.

- **The helix:** The 4-site helical molecule used in the simulations is defined by the radius $R = 1$, the pitch $P = 2$, which is the vertical distance spanned by a single turn and the number of sites on a single helical turn, which is set to 3. This means that the fourth atom is placed at a distance P exactly above the first atom. The atomic sites are equidistantly spaced. Unless specified otherwise the helix will be right-handed.

- **The Hamiltonian:** Aside from the vector $\mathbf{v}$ that is dependent on the helix geometry, the Hamiltonian is characterized by the hopping, Coulomb and spin-orbit interaction strengths t, U and λ. We set $t = 1$ in all simulations. Unless specified otherwise we also set $U = 1$, $\lambda = 1$. This spin-orbit interaction strength is unrealistically high. We therefore also include results for $\lambda = 0.01$, which is a far more realistic value, in appendix B.

- **The leads:** As we discussed in section 1.1, transport experiments typically measure the magnetocurrent, which is the difference in current through the system for opposite magnetisations of the ferromagnetic lead. In our Lindblad equation the magnetisation manifests itself in the coupling strengths $\gamma_\uparrow$, $\gamma_\downarrow$ of the polarised-fermion baths to the system (equation (2.40)). We use the coupling parameter γ, which is set to 1, for the couplings to the unmagnetised lead. The couplings to the magnetised lead are then given as: $\gamma_\uparrow = \frac{\gamma}{\eta}$, $\gamma_\downarrow = \gamma$ for an up-magnetised lead and $\gamma_\uparrow = \gamma$, $\gamma_\downarrow = \frac{\gamma}{\eta}$ for a down-magnetised lead. The polarisation parameter η is set to 5 unless specified otherwise. The baths fillings are characterized by the parameter ν. For $\nu = \pm 1$ one of the baths is completely filled with electrons while the other is completely empty, while $\nu = 0$ represents half-filling on both sides. This parameter thus represents the voltage across the system.

- **On the representation of the results:** In the previous two sections we have seen a persistent error in the values of the current through the system that is seen to decrease with the timestep size dt. Nevertheless, the results of figure 4.7b appeared to be of comparable accuracy to the model of Prosen and Žnidarič [54] despite this numerical error. However, figure 4.8 revealed that this error is more significant for currents through the first and the last bond of the system. In this section, the results for the currents through each bond will be shown in each figure. The the current through a bond is defined in equation (2.14). The bonds are color-coded as shown in figure 4.9. The average of these three results will shown in red, and is plotted in a bolder line for distinguishability. All three magnetocurrents should be equal in the NESS as required by equation (2.15).
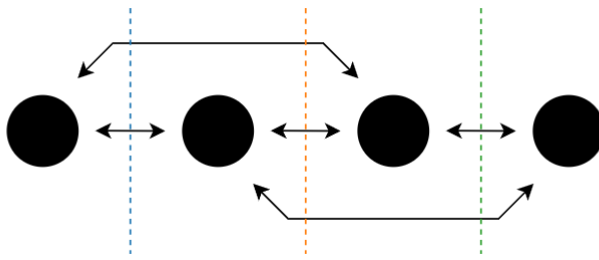
Figure 4.9: The currents through each bond of the 4-site Hubbard model with spin-orbit interactions. The colors indicating each bond correspond to the colors in the figures of the magnetocurrents and magnetoresistances in this section. The (thick) red line in the figures shows the average of these three currents.

As explained in Fransson [33], the net effect of the spin-orbit interaction can be shown to be exactly zero in a three-site chain. Our results in figure 4.10a are in agreement with this statement. The application of the spin-orbit coupling term in the TEBD sweep requires us to contract all tensors of the MPS on which the operator acts. For a chain of 3 sites this amounts to contracting the entire chain, rendering the MPS decomposition of our state redundant. Therefore, the results for the 3-site chain were obtained by exponentiating[2] the full Lindbladian instead of applying the Suzuki-Trotter decomposition. The results of 4-site chains were not obtained using exact calculations, as this requires diagonalizing a matrix of $(4^8 \times 4^8)$, but using the TEBD scheme presented in figure 3.7.

(a) $L = 3$, exact calculation.

(b) $L = 4$, $\lambda = 0$.
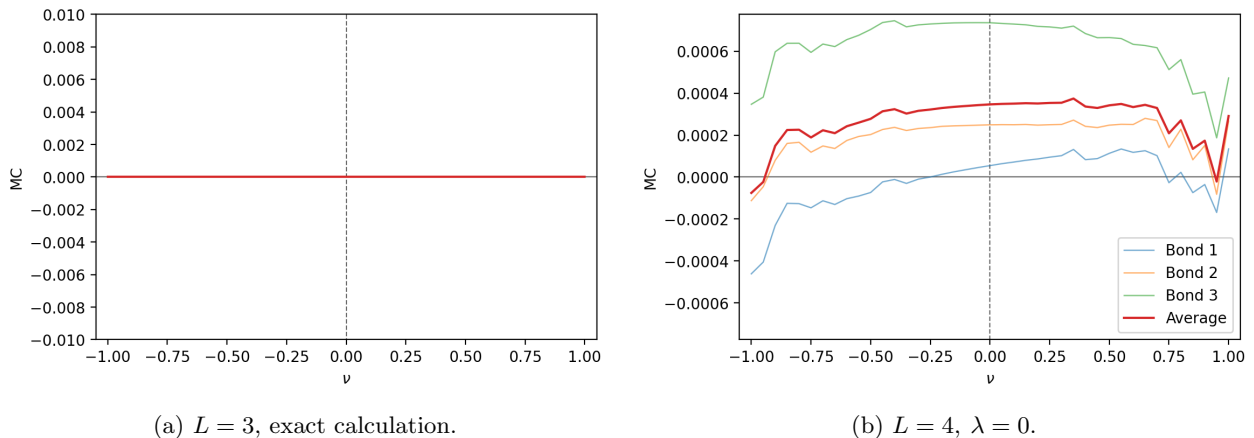
Figure 4.10: Calculated magnetocurrents for a 3-site helical molecule and a 4-site molecule without spin-orbit interactions. In both cases the magnetocurrent should be 0 due to the absence of symmetry-breaking processes. The results of figure (a) were obtained using an exact calculation.

The second important point to verify is the absence of magnetocurrent when no spin-orbit interactions are present. In figure 4.10b we see a nonzero magnetocurrent for all ν. Since the system is completely spin-symmetric in this case (the regular Hubbard Hamiltonian) and given the fact that exact calculations for $L = 3$ with *and* without spin-orbit coupling do not show a magnetocurrent, we assume this to be a numerical error resulting from the Suzuki-Trotter decomposition.

In figure 4.11 the magnetocurrent and magnetoresistance for a 4-site molecule with $t = U = \lambda = 1$ are presented. The magnetocurrent is seen to be an order of magnitude larger compared to the values found for $\lambda = 0$. Even so, the magnetocurrent is seen to be only about half a percent, which is the same order as the results of [11, 34] but orders of magnitude lower than experimentally measured values. The magnetocurrent vanishes for low bias in accordance with the Onsager-Casimir reciprocity. Upon close inspection of figure 4.11a, we find that the blue line, signifying the current through the first bond, does not vanish in the linear regime. Similarly, we see that the average magnetocurrent for $U = 2$ in figure 4.12b also does not vanish in the linear regime, meaning that deviations from Onsager-Casimir reciprocity are present in the results.

---

[2]The time-evolution operator calculated from the Hamiltonian was not strictly exact, as it was obtained using the *scipy.linalg.expm* function of the scipy library, which makes use of a Padé approximation.

(a)   (b)
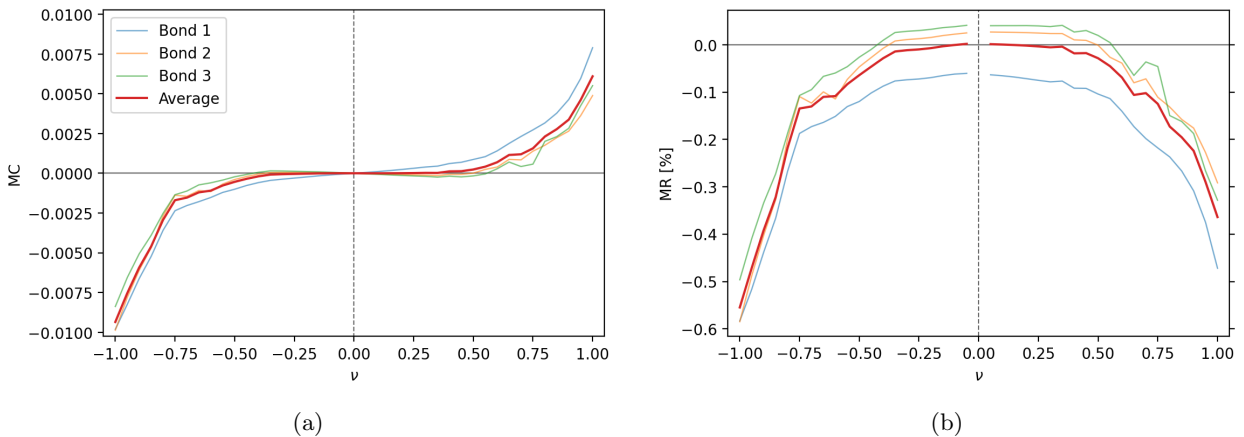
Figure 4.11: (a) Magnetocurrent and (b) associated magnetoresistance for a 4-site molecule with $t = \lambda = U = 1$. The magnetocurrent is seen to be an odd function of bias parameter ν and disappears for low bias. The magnetoresistance is less than a percent, orders of magnitude lower than experimentally measured values.

(a) $U = 0$ (b) $U = 2$
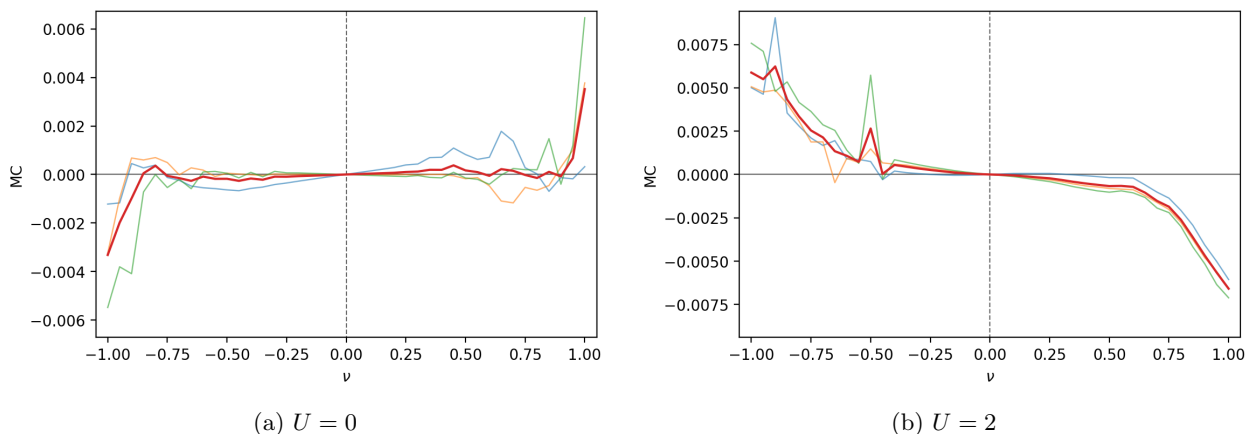
Figure 4.12: Magnetocurrents for a 4-site molecule with $t = \lambda = 1$ and $U = 0, 2$. (a) According to Büttiker reciprocity, the absence of Coulomb interactions ($U = 0$) should cause the magnetocurrent to vanish, which is not seen in this figure. (b) There appears to be a deviation from Onsager-Casimir reciprocity as there is a nonvanishing magnetocurrent at low driving. Interestingly, the magnetocurrent exhibits a sign-flip compared to the $U = 1$ case in figure 4.11a.

The second reciprocity principle that should be satisfied is the Büttiker reciprocity, which states that there should be no magnetocurrent for non-interacting electrons ($U = 0$). We see a clear deviation from expected behaviour in figure 4.12a, where a magnetocurrent can be seen which is odd in the bias ν and is of the same order of magnitude as for $U = 1$.

In figure 4.12b the magnetocurrent is shown for $U = 2$. Interestingly, the sign of the magnetocurrent appears to have flipped compared to $U = 1$. Due to time constraints this has not been investigated any further and thus we can not provide a critical value U_C at which this change occurs, nor what the reason behind this is. This behaviour is not impossible, however, it can for instance be seen in figures 3.1b and 3.1d of [34], for the same model as in this thesis under the Hubbard I approximation. As stated before, the results for $U = 2$ do not satisfy the Onsager-Cisimir reciprocity, since the magnetocurrent does not vanish in the linear regime.

To summarize, from the results we have just discussed we can conclude that the model does exhibit a finite magnetocurrent with the presence of SOC, that is an order of magnitude larger than the erroneous magnetocurrent found for the standard Hubbard model. The results of $U = 1, 2$ are odd in bias parameter ν, which is in accordance with most experimentally measured behaviour. For $U = 1$ Onsager-Casimir reciprocity is satisfied (on average), while this is not so for $U = 2$. In the additional results shown in appendix B we also observe that Onsager-Casimir reciprocity is not always satisfied. Moreover, Büttiker reciprocity is not completely satisfied for $U = 0$, as a nonzero magnetocurrent can be seen for high driving.

As stated, additional results are presented in appendix B for simulations with a molecule of opposite chirality,

low spin-orbit interaction strength and different lead magnetisation. For lower spin-orbit interaction strength, $\lambda = 0.01$, the magnitude of the mangetoresistance dropped by a factor 10, to the order of 0.1%.

Calculations have been repeated for selected points ($\nu = 0.1, 0.25, 0.5, 0.8, 0.9, 1$) with lower timestep size, $dt \to dt/3$. Due to time constraints we have been unable to recalculate all the presented results with this timestep. Even so, these calculations provide elucidation as to the possible cause of these errors. The results for $U = 0, 1$ are included in figures 4.13 and 4.14 in this section, for the other results we refer to appendix B. In figure 4.13, the influence of the timestep size on the magnetocurrent is shown in the low-to-medium driving regime. Most immediately apparent is the fact that for lower dt, the spread in the three magnetocurrents becomes smaller. Importantly, the deviation from the Büttiker reciprocity seems to become less severe, as all magnetocurrents in figure 4.13b become closer to 0. The improvement with regards to the deviation from the Onsager-Casimir reciprocity for $U = 2$ is less significant but can nonetheless be seen (figure B.1a).

In figure 4.14, similar results are presented for the high-driving regime. For $U = 1, 2$ the difference between the magnetocurrents decreases with the timestep similar to the previous results. For $U = 0$, this is only the case for $\nu = 1$, while the difference increases for $\nu = 0.8, 0.9$. However, for the smaller timestep the magnetocurrents do not switch their relative positions for different ν (the green line remains the highest for all ν, the blue line the lowest). Notably, the average of the magnetocurrents for $U = 0$ at $\nu = 1$ does not decrease for lower dt.

Our results are subject to two main numerical errors, which are the truncation of our state, parametrised by χ, and the time-integration error, defined by the timestep size dt. The results shown are obtained with a truncation parameter $\chi = 85$, which means that only the middle three tensors in our MPS representation were truncated. The results indicate that the finite timestep is of crucial importance to the accuracy of the current calculations, similar to the results for the previous models. We see that the deviation from current continuity and the deviation from the behaviour dictated by the reciprocity principles decrease with the timestep size. Aside from smaller timestep sizes, this error can be further reduced by applying higher-order Suzuki-Trotter schemes, and by implementing different operator-splitting methods (see reference [67]).

For longer molecular systems the truncation error may become more influential. In the previous section we have seen that the truncation parameter mostly influences the capability of the model to converge to a steady state, illustrated in figure 4.6. Figures of the Von Neumann entanglement entropy over time for different drivings ν with spin-orbit coupling present are shown in the appendix, figure B.2. It is seen that the entropy is highest for high-driving, indicating that deviations from expected behaviour at high driving may in part be caused by the truncation error. It is therefore suggested that future studies studying longer molecules investigate the importance of the truncation parameter in the high-driving regime.
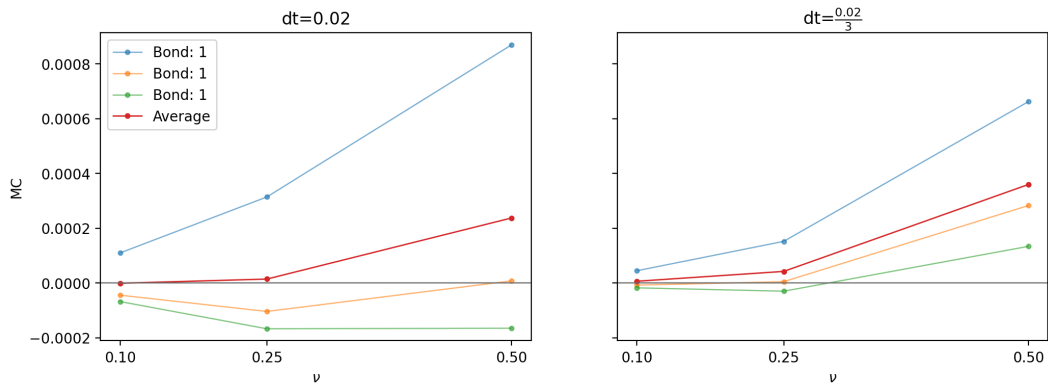
(a) U=1
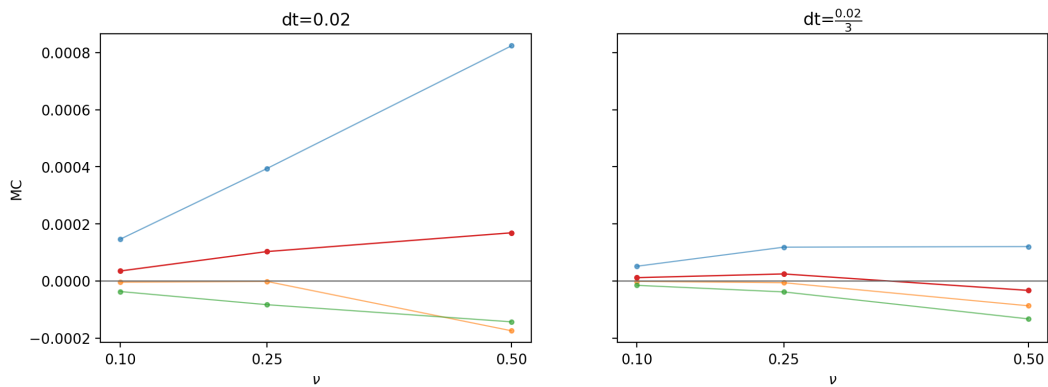
(b) U=0

Figure 4.13: Influence of a lower timestep size on the magnetocurrent profile of the NESS for different drivings in the low-to-medium driving regime.
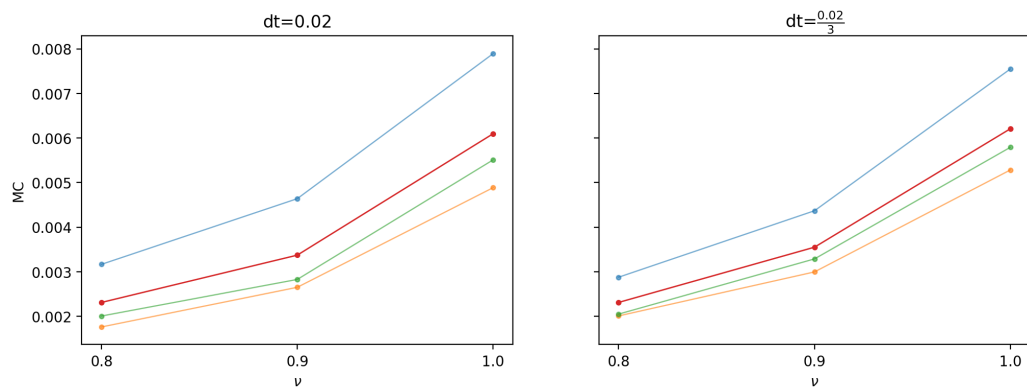
(a) U=1
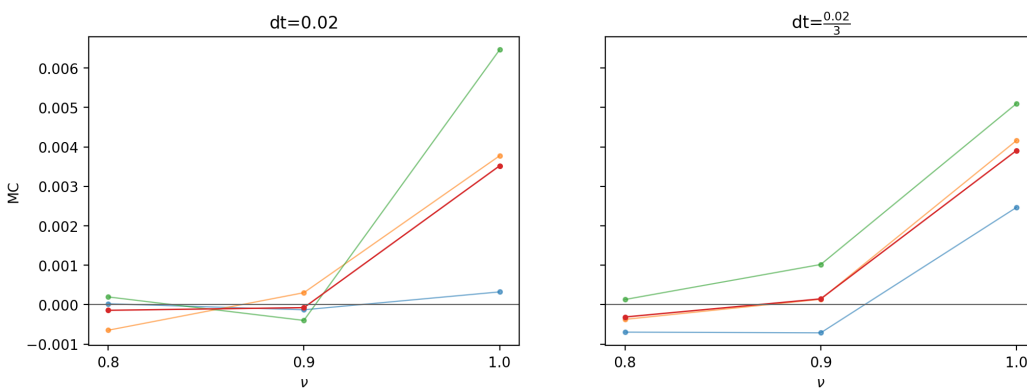
(b) U=0

Figure 4.14: Influence of a lower timestep size on the magnetocurrent profile of the NESS for different drivings in the high driving regime.

5   Conclusion

Summary of the results

In this work we have simulated boundary-driven transport through spin systems using the matrix product states formalism. We have used this formalism to simulate electron transport through a boundary-driven Hubbard model with and without spin-orbit interactions, by employing the Jordan-Wigner transformation to map the Hubbard model to a double spin chain, or spin ladder. The density operator describing the system was written as a vectorised matrix product density operator, the dynamics of which were described using a vectorised Lindblad equation. The aim of this thesis was to investigate the viability of matrix product states as a tool to study chirality-induced spin selectivity of electron transport through helical molecules. We applied this novel approach to a tight-binding model proposed by Fransson in 2019 [33], which considers electrons with local Coulomb interactions and a next-nearest neighbour spin-orbit coupling inspired by the Kane-Mele model. The advantage of this approach is that it does not require any systematic approximations in the current calculation, in contrast to previous studies of this model, which made use of the Hartree-Fock and Hubbard-I approximations.

To study the accuracy of the method used, we first studied the spin transport through a spin-1/2 Heisenberg-XXZ chain and the electron transport through the standard Hubbard model in the steady state. Both these models have been the subject of previous studies ([54, 59, 61]) using approaches similar to the one employed in this thesis. We used the results of these studies as a benchmark to verify the accuracy of our method. Our model was able to reproduce these results with a comparable accuracy. However, the maximal system sizes our method is capable of reaching are lower than what was achieved in those studies and it required a higher truncation parameter (i.e. more numerical resources) to reach the nonequilibrium steady state of the Hubbard model. It is possible that these studies employed additional techniques to facilitate convergence to the nonequilibrium steady state. In spite of these shortcomings, the method is capable of reaching system sizes of up to $L = 32$, far beyond the minimal system length for which spin-selective effects should occur ($L = 4$), and is therefore sufficient for the purposes of this thesis.

However, for both benchmark models it was found that the steady-state currents through each bond in the system were not identical, indicating a deviation from continuity. This deviation was confirmed to be a numerical error resulting from the Suzuki-Trotter decomposition of the time-evolution operator; for both benchmark models the discrepancy was seen to decrease with the timestep size. In this work we exclusively employed Suzuki-Trotter decompositions of the first order, which have an error of $\hat{\mathcal{O}}(dt^2)$.

We have studied the steady-state electron current through a 4-site helical molecule with spin-orbit interactions, which is the minimum system size for CISS to occur in this model. We have confirmed the presence of a finite magnetocurrent through the system that is odd in the bias, in accordance with most experiments. The associated magnetoresistance was found to be less than 1% in all performed simulations. This is two orders of magnitude below experimentally measured values and corresponds with the findings of previous theoretical studies of this model [11, 34]. Importantly, these results were obtained by using an unrealistically high value for the spin-orbit interaction strength, which was set equal to the hopping parameter.

Furthermore, we have investigated the qualitative behaviour of the magnetocurrent in different parameter regimes. We have specifically found that the Büttiker reciprocity is not satisfied; in the absence of electron interactions, the results showed the presence of a finite magnetocurrent at high driving. Moreover, in a number of cases the Onsager-Casimir reciprocity was not satisfied, as a linear magnetocurrent persisted in the low-driving regime.

The numerical error that was observed in the current calculations for the Heisenberg-XXZ and regular Hubbard models, persisted in the results for the Hubbard model with spin-orbit coupling. For a molecule of 4 sites, the magnetocurrents across each of the 3 system bonds should be equal in the steady state. This was not reflected in our results, where a different magnetocurrent was found for each bond. Similar to the current discrepancy observed for the benchmark models, these differences became decreased as the size of the timestep decreased. Moreover, for some results the decrease in timestep size resulted in a closer adherence to Onsager-Casimir reciprocity and Büttiker reciprocity, except at maximal driving. The entanglement present in the system was seen to increase with the driving strength, indicating that the truncation parameter may be an important consideration in this case.

Discussion and Recommendations

In this work we have shown that matrix product states can be used to study spin-selective electron transport in tight-binding models of chiral molecules. The results obtained in this work were roughly consistent with the two most important reciprocity principles in the context of CISS in transport: the Büttiker reciprocity

and the Onsager-Casimir reciprocity. A deviation from the expected behaviour was seen in multiple cases. Additionally, in all simulated models the current continuity was not satisfied. It has been confirmed that these deviations are dependent on the size of the numerical time-integration step, and we are therefore confident that these deviations are due to the numerical time step error. The time-integration error stems from the use of the Suzuki-Trotter decomposition of the time-evolution operator. In this work we have used the lowest-order Suzuki-Trotter decomposition, which has an error of $\hat{\mathcal{O}}(dt^2)$. We recommend that future studies using this approach attempt to reduce this error, for example by applying a higher order time-integration scheme. Furthermore, this work implemented the action of the Lindblad operators on the edge sites in a rather naive fashion, by splitting the Lindbladian superoperator into a purely Hamiltonian and a purely dissipative part. In this implementation, the preservation of the positive semi-definiteness of the density operator is not guaranteed. In [67], a different operator-splitting method for the Lindblad superoperator is outlined, which preserves positivity for up to second-order Suzuki-Trotter decompositions. A method to devise schemes of higher order is provided as well. This approach has recently been applied to the MPDO model used in this thesis for simulating the boundary-driven Heisenberg-XXZ chain [68]. A significant reduction in the trace error was reported, although the effect on the current seemed to be limited. We recommend [68] to be used as a foundational basis for future efforts to reduce the time-integration error present in this work.

A number of unforeseen complications that arose during this thesis work stem from the Jordan-Wigner transformation. Most significantly, as discussed in section 2.3, the fermionic anticommutation relations give rise to products of $\hat{\sigma}^z$ matrices in the hopping and spin-orbit coupling terms of the Hamiltonian. As a result, the spin-orbit coupling terms transformed into an operator acting on six sites in spin space, which had to be applied twice in each TEBD sweep. Repeatedly performing tensor contractions and decompositions of this magnitude is highly computationally demanding. This has limited, among other factors, our ability to thoroughly study the model due to the considerable time required for computations to complete, even when making use of high-performance computing clusters. It is recommended that future studies reconsider the use of the Jordan-Wigner transformation, and instead consider working directly in fermion space with basis states $\{|0\rangle, |\uparrow\rangle, |\downarrow\rangle, |\uparrow\downarrow\rangle\}$. This decreases the size of the computations and allows the spin-orbit interactions to be implemented using swap operations, which can be parallelized more efficiently to leverage high-performance computing capabilities. The simple reason that this work makes use of the Jordan-Wigner transformation, is because it is employed in previous works studying fermion transport using matrix product states. This may be due to the fact that most available software packages for MPS are designed for spin systems, making the use of the Jordan-Wigner transformation more convenient. However, given the fact that we built our model from the ground up, working in fermion space from the beginning may have been more advantageous.

To summarize, we recommend that future works employ more sophisticated time-integration methods to reduce the numerical errors present in this work, and work directly in fermion space instead of using the Jordan-Wigner transformation to map the Hubbard model to a spin system. In light of these two recommendations, future works may build upon this approach in order to make matrix product states a viable tool for studying spin-selective electron transport. Future studies should aim at reproducing the Onsager-Casimir reciprocity in the linear regime and Büttiker reciprocity in absence of electron interactions. The strength of the method of this thesis lies in the fact that it does not require any systematic approximations to be made on the Hamiltonian. By implementing realistic model parameters, the method can be used to study the importance of electron correlations to chirality-induced spin selectivity in helical molecular structures.

Bibliography

[1] K. Ray, S. P. Ananthavel, D. H. Waldeck, and R. Naaman, "Asymmetric scattering of polarized electrons by organized organic films of chiral molecules," *Science*, vol. 283, no. 5403, pp. 814–816, 1999.

[2] B. Göhler, V. Hamelbeck, T. Z. Markus, M. Kettner, G. F. Hanne, Z. Vager, R. Naaman, and H. Zacharias, "Spin selectivity in electron transmission through self-assembled monolayers of double-stranded dna," *Science*, vol. 331, no. 6019, pp. 894–897, 2011.

[3] R. Naaman and D. H. Waldeck, "Spintronics and chirality: Spin selectivity in electron transport through chiral molecules," *Annu. Rev. Phys. Chem.*, vol. 66, no. 1, pp. 263–281, 2015.

[4] F. Dunning, "Mott electron polarimetry," *Nucl. Instrum. Methods Phys. Res. A*, vol. 347, no. 1, pp. 152–160, 1994.

[5] Z. Xie, T. Z. Markus, S. R. Cohen, Z. Vager, R. Gutierrez, and R. Naaman, "Spin specific electron conduction through dna oligomers," *Nano Lett.*, vol. 11, no. 11, pp. 4652–4655, 2011.

[6] K. H. Huisman and J. M. Thijssen, "Ciss effect: A magnetoresistance through inelastic scattering," *J. Phys. Chem. C*, vol. 125, pp. 23364 – 23369, 2021.

[7] R. Naaman, D. H. Waldeck, and Y. Paltiel, "Chiral molecules-ferromagnetic interfaces, an approach towards spin controlled interactions," *Appl. Phys. Lett.*, vol. 115, no. 13, p. 133701, 2019.

[8] T. S. Metzger, S. Mishra, B. P. Bloom, N. Goren, A. Neubauer, G. Shmul, J. Wei, S. Yochelis, F. Tassinari, C. Fontanesi, D. H. Waldeck, Y. Paltiel, and R. Naaman, "The electron spin as a chiral reagent," *Angew. Chem. Int. Ed.*, vol. 59, no. 4, pp. 1653–1658, 2020.

[9] B. P. Bloom, Y. Paltiel, R. Naaman, and D. H. Waldeck, "Chiral induced spin selectivity," *Chem. Rev.*, vol. 124, no. 4, pp. 1950–1991, 2024.

[10] N. Hatano and G. Ordonez, "Time-reversal symmetry and arrow of time in quantum mechanics of open systems," *Entropy*, vol. 21, no. 4, p. 380, 2019.

[11] J. Heinisch, *Chiral Induced Spin Selectivity: The Effect of Coulomb Interactions and Spin-Orbit Couplings*. Master thesis, TU Delft, 2022.

[12] M. Buttiker, "Symmetry of electrical conduction," *IBM J. Res. Dev.*, vol. 32, no. 3, pp. 317–334, 1988.

[13] P. Mazur and S. de Groot, "On onsager's relations in a magnetic field," *Physica*, vol. 19, no. 1, pp. 961–970, 1953.

[14] S. Yeganeh, M. A. Ratner, E. Medina, and V. Mujica, "Chiral electron transport: Scattering through helical potentials," *J. Chem. Phys.*, vol. 131, no. 1, p. 014707, 2009.

[15] E. Medina, F. López, M. A. Ratner, and V. Mujica, "Chiral molecular films as electron polarizers and polarization modulators," *EPL*, vol. 99, no. 1, p. 17006, 2012.

[16] S. Varela, E. Medina Dagger, F. López, and V. Mujica, "Inelastic electron scattering from a helical potential: Transverse polarization and the structure factor in the single scattering approximation," *J. Phys. Condens. Matter*, vol. 26, p. 015008, 2013.

[17] R. Gutierrez, E. Díaz, R. Naaman, and G. Cuniberti, "Spin-selective transport through helical molecular systems," *Phys. Rev. B*, vol. 85, no. 8, p. 081404, 2012.

[18] A.-M. Guo and Q.-f. Sun, "Spin-selective transport of electrons in dna double helix," *Phys. Rev. Lett.*, vol. 108, p. 218102, 2012.

[19] R. Gutierrez, E. Díaz, C. Gaul, T. Brumme, F. Domínguez-Adame, and G. Cuniberti, "Modeling spin transport in helical fields: Derivation of an effective low-dimensional hamiltonian," *J. Phys. Chem. C*, vol. 117, no. 43, pp. 22276–22284, 2013.

[20] V. V. Maslyuk, R. Gutierrez, and G. Cuniberti, "Spin–orbit coupling in nearly metallic chiral carbon nanotubes: a density-functional based study," *Phys. Chem. Chem. Phys.*, vol. 19, pp. 8848–8853, 2017.

[21] M. Zöllner, S. Varela, E. Medina Dagger, V. Mujica, and C. Herrmann, "Insight into the origin of chiral-induced spin selectivity from a symmetry analysis of electronic transmission," *J. Chem. Theory Comput.*, vol. 16, 2020.

[22] A. Dianat, R. Gutierrez, H. Alpern, V. Mujica, A. Ziv, S. Yochelis, O. Millo, Y. Paltiel, and G. Cuniberti, "Role of exchange interactions in the magnetic response and intermolecular recognition of chiral molecules," *Nano Lett.*, vol. 20, no. 10, p. 7077–7086, 2020.

[23] F. Evers, A. Aharony, N. Bar-Gill, O. Entin-Wohlman, P. Hedegård, O. Hod, P. Jelinek, G. Kamieniarz, M. Lemeshko, K. Michaeli, V. Mujica, S. Refaely-Abramson, O. Tal, J. Thijssen, M. Thoss, J. van Ruiten-beek, L. Venkataraman, and L. Kronik, "Theory of chirality induced spin selectivity: Progress and challenges," *Adv. Mater.*, vol. 34, p. 2106629, 2022.

[24] J. Gersten, K. Kaasbjerg, and A. Nitzan, "Induced spin filtering in electron transmission through chiral molecular layers adsorbed on metals with strong spin-orbit coupling," *J. Chem. Phys.*, vol. 139, no. 11, p. 114111, 2013.

[25] D. Mishra, T. Z. Markus, R. Naaman, M. Kettner, B. Göhler, H. Zacharias, N. Friedman, M. Sheves, and C. Fontanesi, "Spin-dependent electron transmission through bacteriorhodopsin embedded in purple membrane," *Proc. Natl. Acad. Sci.*, vol. 110, no. 37, pp. 14872–14876, 2013.

[26] M. Kettner, V. V. Maslyuk, D. Nürenberg, J. Seibel, R. Gutierrez, G. Cuniberti, K.-H. Ernst, and H. Zacharias, "Chirality-dependent electron spin filtering by molecular monolayers of helicenes," *J. Phys. Chem. Lett.*, vol. 9, no. 8, pp. 2025–2030, 2018.

[27] Y. Liu, J. Xiao, J. Koo, and B. Yan, "Chirality-driven topological electronic structure of dna-like materials," *Nat. Mater.*, vol. 20, no. 5, p. 638–644, 2021.

[28] S. Alwan and Y. Dubi, "Spinterface origin for the chirality-induced spin-selectivity effect," *J. Am. Chem. Soc.*, vol. 143, no. 35, pp. 14235–14241, 2021.

[29] Y. Dubi, "Spinterface chirality-induced spin selectivity effect in bio-molecules," *Chem. Sci.*, vol. 13, pp. 10878–10883, 2022.

[30] S. Alwan, A. Sharoni, and Y. Dubi, "Role of electrode polarization in the electron transport chirality-induced spin-selectivity effect," *J. Phys. Chem. C*, vol. 128, no. 15, pp. 6438–6445, 2024.

[31] K.-W. Kim, B.-G. Park, and K.-J. Lee, "Spin current and spin-orbit torque induced by ferromagnets," *npj Spintronics*, vol. 2, no. 1, p. 8, 2024.

[32] Y. Adhikari, T. Liu, H. Wang, Z. Hua, H. Liu, E. Lochner, P. Schlottmann, B. Yan, J. Zhao, and P. Xiong, "Interplay of structural chirality, electron spin and topological orbital in chiral molecular spin valves," *Nat. Commun.*, vol. 14, p. 5163, 2023.

[33] J. Fransson, "Chirality-induced spin selectivity: The role of electron correlations," *J. Phys. Chem. Lett.*, vol. 10, no. 22, p. 7126–7132, 2019.

[34] K. H. Huisman, *Theory of Chirality Induced Spin Selectivity in Two Terminal Transport*. Phd thesis, TU Delft, 2023.

[35] J. Fransson, "Vibrational origin of exchange splitting and "chiral-induced spin selectivity"," *Phys. Rev. B*, vol. 102, no. 23, 2020.

[36] J. Fransson, "Chiral phonon induced spin polarization," *Phys. Rev. Res.*, vol. 5, p. L022039, 2023.

[37] L. Zhang, Y. Hao, W. Qin, S. Xie, and F. Qu, "Chiral-induced spin selectivity: A polaron transport model," *Phys. Rev. B*, vol. 102, p. 214303, 2020.

[38] M. Barroso, J. Balduque, F. Domínguez-Adame, and E. Díaz, "Spin-dependent polaron transport in helical molecules," *Appl. Phys. Lett.*, vol. 121, no. 14, p. 143505, 2022.

[39] X. Yang, C. H. van der Wal, and B. J. van Wees, "Detecting chirality in two-terminal electronic nanodevices," *Nano Lett.*, vol. 20, no. 8, pp. 6148–6154, 2020.

[40] J. Fransson, "The chiral induced spin selectivity effect what it is, what it is not, and why it matters," *Isr. J. Chem.*, vol. 62, no. 11-12, p. e202200046, 2022.

[41] K. H. Huisman, J.-B. M.-Y. Heinisch, and J. M. Thijssen, "Chirality-induced spin selectivity (ciss) effect: Magnetocurrent–voltage characteristics with coulomb interactions i," *J. Phys. Chem. C*, vol. 127, no. 14, pp. 6900–6905, 2023.

[42] K. Michaeli, V. Varade, R. Naaman, and D. H. Waldeck, "A new approach towards spintronics–spintronics with no magnets," *J. Phys.: Condens. Matter*, vol. 29, no. 10, p. 103002, 2017.

[43] W. Mtangi, V. Kiran, C. Fontanesi, and R. Naaman, "Role of the electron spin polarization in water splitting," *J. Phys. Chem. Lett.*, vol. 6, no. 24, pp. 4916–4922, 2015.

[44] B. Bloom, A. Waldeck, and D. Waldeck, "Homochirality and chiral-induced spin selectivity: A new spin on the origin of life," *Proc. Natl. Acad. Sci.*, vol. 119, p. e2210505119, 08 2022.

[45] R. Mahajan, C. D. Freeman, S. Mumford, N. Tubman, and B. Swingle, "Entanglement structure of non-equilibrium steady states," 2016.

[46] A. Panda and S. Banerjee, "Entanglement in nonequilibrium steady states and many-body localization breakdown in a current-driven system," *Phys. Rev. B*, vol. 101, no. 18, p. 184201, 2020.

[47] S. Dalum and P. Hedegård, *The CISS Effect.* Phd thesis, University of Copenhagen, 2019.

[48] F. Meijer, *Rashba spin-orbit interaction in mesoscopic systems.* Phd thesis, TU Delft, 2005.

[49] C. L. Kane and E. J. Mele, "Quantum spin hall effect in graphene," *Phys. Rev. Lett.*, vol. 95, p. 226801, 2005.

[50] F. D. M. Haldane, "Model for a quantum hall effect without landau levels: Condensed-matter realization of the "parity anomaly"," *Phys. Rev. Lett.*, vol. 61, pp. 2015–2018, 1988.

[51] H.-P. Breuer and F. Petruccione, *The Theory of Open Quantum Systems.* Oxford University Press, 2006.

[52] G. T. Landi, D. Poletti, and G. Schaller, "Nonequilibrium boundary-driven quantum systems: Models, methods, and properties," *Rev. Mod. Phys.*, vol. 94, p. 045006, 2022.

[53] Y. Shimizu, K. Matsuura, and H. Yahagi, "Application of matrix product states to the hubbard model in one spatial dimension," 2013. https://doi.org/10.48550/arXiv.1310.3340".

[54] T. Prosen and M. Žnidarič, "Diffusive high-temperature transport in the one-dimensional hubbard model," *Phys. Rev. B*, vol. 86, no. 12, p. 125118, 2012.

[55] G. B. Mbeng, A. Russomanno, and G. E. Santoro, "The quantum ising chain for beginners," 2020. https://doi.org/10.48550/arXiv.2009.09208.

[56] J.-M. Reiner, M. Marthaler, J. Braumüller, M. Weides, and G. Schön, "Emulating the one-dimensional fermi-hubbard model by a double chain of qubits," *Phys. Rev. A*, vol. 94, no. 3, p. 032338, 2016.

[57] B. Žunkovič and T. Prosen, "Explicit solution of the lindblad equation for nearly isotropic boundary driven xy spin 1/2 chain," *J. Stat. Mech: Theory Exp.*, vol. 2010, no. 08, p. P08016, 2010.

[58] K. Yamanaka and T. Sasamoto, "Exact solution for the Lindbladian dynamics for the open XX spin chain with boundary dissipation," *SciPost Phys.*, vol. 14, p. 112, 2023.

[59] A. Werner, D. Jaschke, P. Silvi, M. Kliesch, T. Calarco, J. Eisert, and S. Montangero, "Positive tensor network approach for simulating open quantum many-body systems," *Phys. Rev. Lett.*, vol. 116, no. 23, 2016.

[60] M. Takahashi, *Thermodynamics of One-Dimensional Solvable Models.* Cambridge University Press, 1999.

[61] T. Prosen, "Exact nonequilibrium steady state of a strongly driven open xxz chain," *Phys. Rev. Lett.*, vol. 107, no. 13, p. 137201, 2011.

[62] S. R. White, "Density matrix formulation for quantum renormalization groups," *Phys. Rev. Lett.*, vol. 69, pp. 2863–2866, 1992.

[63] U. Schollwöck, "The density-matrix renormalization group in the age of matrix product states," *Ann. Phys.*, vol. 326, no. 1, pp. 96–192, 2011.

[64] G. Vidal, "Efficient classical simulation of slightly entangled quantum computations," *Phys. Rev. Lett.*, vol. 91, no. 14, 2003.

[65] M. B. Hastings, "An area law for one-dimensional quantum systems," *J. Stat. Mech: Theory Exp.*, vol. 2007, no. 08, p. P08024–P08024, 2007.

[66] J. Cui, J. I. Cirac, and M. C. Bañuls, "Variational matrix product operators for the steady state of dissipative quantum systems," *Phys. Rev. Lett.*, vol. 114, no. 22, 2015.

[67] Y. Cao and J. Lu, "Structure-preserving numerical schemes for lindblad equations," 2021.

[68] A. J. de Bruyn, *Implementation of the Lindbladian in Matrix Product States*. Bachelor thesis, TU Delft, 2024.

[69] M. A. Nielsen and I. L. Chuang, *Quantum Computation and Quantum Information*. Cambridge University Press, 2000.

[70] D. Jaschke, S. Montangero, and L. D. Carr, "One-dimensional many-body entangled open quantum systems with tensor network methods," *Quantum Sci. Technol.*, vol. 4, no. 1, p. 013001, 2018.

[71] M. Zwolak and G. Vidal, "Mixed-state dynamics in one-dimensional quantum lattice systems: A time-dependent superoperator renormalization algorithm," *Phys. Rev. Lett.*, vol. 93, no. 20, 2004.

[72] H. P. Casagrande, D. Poletti, and G. T. Landi, "Analysis of a density matrix renormalization group approach for transport in open quantum systems," *Comput. Phys. Commun.*, vol. 267, p. 108060, 2021.

[73] A. Gilchrist, D. R. Terno, and C. J. Wood, "Vectorization of quantum operations and its use," 2011. https://doi.org/10.48550/arXiv.0911.2539, pages 1-4.

[74] E. Mascarenhas, H. Flayac, and V. Savona, "Matrix-product-operator approach to the nonequilibrium steady state of driven-dissipative quantum arrays," *Phys. Rev. A*, vol. 92, no. 2, p. 022116, 2015.

[75] Y. Yoo, C. D. White, and B. Swingle, "Open-system spin transport and operator weight dissipation in spin chains," *Phys. Rev. B*, vol. 107, no. 11, p. 115118, 2023.

[76] F. Verstraete, J. J. García-Ripoll, and J. I. Cirac, "Matrix product density operators: Simulation of finite-temperature and dissipative systems," *Phys. Rev. Lett.*, vol. 93, no. 20, p. 207204, 2004.

[77] G. Lindblad, "On the generators of quantum dynamical semigroups," *Commun. Math. Phys.*, vol. 48, no. 2, pp. 119 – 130, 1976.

[78] A. Kossakowski, "On quantum statistical mechanics of non-hamiltonian systems," *Rep. Math. Phys.*, vol. 3, no. 4, pp. 247–274, 1972.

A The Lindblad Equation

A.1 Outline of the Derivation

We begin by assuming that at $t = 0$ our universe is in a product state $\rho_U(0) = \rho_S(0) \otimes \rho_E(0)$. Let us denote $\rho(\mathcal{H}_S)$ the space of density matrices in the Hilbert space of S. We define our dynamical map $V(t) : \rho(\mathcal{H}_S) \to \rho(\mathcal{H}_S)$ for a fixed time $t \geq 0$ by

$$V(t)\rho_S(0) \equiv \mathrm{Tr}_E\big(U(t)\rho_U(0)U^\dagger(t)\big) = \rho_S(t). \tag{A.1}$$

We clearly have that $V(0)\rho_S(0) = \rho_S(0)$. Since density matrices are always positive semi-definite, we know $V(t)$ must be a completely positive map. Next, we assume a weak coupling between S and the environment and that the environment contains many degrees of freedom, such that the effect of S on the environment is negligible. This means that the environment can be assumed to be at equilibrium at all times, i.e. $\rho_E(t) = \rho_E$. This approximation is called the *Born approximation*. We expand ρ_E as

$$\rho_E = \sum_i p_i \, |\phi_i\rangle_E \, \langle\phi_i|_E \,, \tag{A.2}$$

where $\{|\phi_i\rangle_E\}$ form an orthonormal basis in $\mathcal{H}_E$. The p_i are non-negative, real coefficients satisfying $\sum_i p_i = \mathrm{Tr}_E(\rho_E) = 1$. We use this basis for $\mathcal{H}_E$ to write $V(t)$ in terms of operators acting on the Hilbert space of S:

$$V(t)\rho_S(0) = \sum_{ij} W_{ij}(t)\rho_S(0)W_{ij}^\dagger(t), \tag{A.3}$$

$$W_{ij}(t) = \sqrt{p_j} \, \langle\phi_i|_E \, U(t) \, |\phi_j\rangle_E \,. \tag{A.4}$$

$U(t)$ is an operator acting on the universe $\mathcal{H}_S \otimes \mathcal{H}_E$, so we see that the operators $W_{ij}(t)$ are operators acting on S.

Using equation (A.4) and the fact that $U(t)$ is a unitary operator we find

$$\sum_{ij} W_{ij}^\dagger(t)W_{ij}(t) = \mathbb{I}_S \tag{A.5}$$

and consequently

$$\mathrm{Tr}_S\big(V(t)\rho_S(0)\big) = 1. \tag{A.6}$$

Thus we have shown that the $V(t)$ is completely positive and trace-preserving (CPTP) with minimal loss of generality.

If we allow the parameter t to change continuously we obtain a one-parameter family of maps $\{V(t)|t \geq 0\}$. Now we make our second approximation, which is that the interaction between the system and the environment only depends on the current state of the system, i.e. the interaction is *Markovian*. In mathematical terms this reads

$$V(t)V(t')\rho_S(0) = V(t + t')\rho_S(0), \; t, t' \geq 0. \tag{A.7}$$

This assumption is called the *Markov approximation*. As a side note, a set $\{V(t)\}$ equipped with an associative internal operation (equation (A.7)) is called a semigroup [51], therefore the family of maps $\{V(t)|t \geq 0\}$ is called a quantum dynamical semigroup.

To summarize, by restricting ourselves to weak, Markovian interactions we have that the family of maps $\{V(t)|t \geq 0\}$ has a number of properties, namely $\forall t, t' \geq 0$:

- $V(t)$ is a completely positive map

- $V(t) + V(t') = V(t + t')$

- $V(0)\rho_S(0) = \rho_S(0)$

- $V(t)$ is continuous in t.

We assume a last condition:

- $V(t)\mathbb{I}_S = \mathbb{I}_S$.

As mentioned by Lindblad [77], it can be shown [78] that these conditions (in a more precise mathematical formulation) ensure that there exists a (bounded) map $\hat{\mathcal{L}} : \rho(\mathcal{H}_S) \to \rho(\mathcal{H}_S)$ such that

$$V(t) = \exp(\hat{\mathcal{L}}t). \tag{A.8}$$

Recall that we defined $\rho(\mathcal{H}_S)$ to be the set of density matrices of the Hilbert space $\mathcal{H}_S$. The map $\hat{\mathcal{L}}$ is called the *generator* of the quantum dynamical semigroup $\{V(t)|t \geq 0\}$. Combining result (A.8) with the definition of $V(t)$ in equation (A.1) and taking the derivative with respect to t results in the differential equation

$$\frac{d}{dt}\rho_S(t) = \hat{\mathcal{L}}\rho_S(t). \tag{A.9}$$

This equation is called the *quantum Markovian master equation* and is remarkably similar to the Liouville-von Neumann equation (equation (2.2)) if we see the generator $\hat{\mathcal{L}}$ as a Liouvillian. Finding a closed-form expression for the semigroup $\{V(t)|t \geq 0\}$ can become quite difficult, therefore the dynamics of open quantum systems are usually calculated by finding the expression of the generator $\hat{\mathcal{L}}$ and (numerically) integrating equation (A.9).

It remains to construct the general form of $\hat{\mathcal{L}}$, which was done by Lindblad in the aforementioned paper [77]. This derivation is a projection of the operators of $W_{ij}(t)$ of equation (A.3) on an orthonormal basis $\{F_\alpha\}$ of the operator space (of dimension N^2) on Hilbert space $\mathcal{H}_S$ (where orthonormality is understood as $\text{Tr}_S(F_\alpha F_\beta) = \delta_{\alpha\beta}$). The basis is chosen with $\text{Tr}_S(F_{N^2}) = 1$ such that all other operators in the basis have trace 0. Substituting the projection of the operators $W_{ij}(t)$ on this basis in equation (A.3) and applying the restriction that the map should be trace preserving yields the famous Lindblad equation:

$$\hat{\mathcal{L}}\rho_S = -\frac{i}{\hbar}[\hat{H}, \rho_S] + \sum_k \gamma_k \big(L_k \rho_S L_k^\dagger - \frac{1}{2}\{L_k^\dagger L_k, \rho_S\}\big). \tag{A.10}$$

Here, $\hat{H}$ is the system Hamiltonian and L_k are the Lindblad operators which govern unitary the non-unitary parts of the system dynamics, respectively. A step-by-step derivation is given in Breuer and Petruccione [51].

A.2 The Dissipative Continuity Equation

Here we will derive the currents in and out of the system using equation (2.16) as stated in [52], repeated here for convenience:

$$\frac{d\hat{n}_i}{dt} = i[\hat{H}, \hat{n}_i] + \text{Tr}(\hat{n}_i \hat{\mathcal{D}}(\rho_S)).$$

Let us focus on the dissipative part,

$$\text{Tr}(\hat{n}_i \hat{\mathcal{D}}(\rho_S)) = \text{Tr}\Big(\hat{n}_i \sum_k \gamma_k \big(\hat{L}_k \rho_S \hat{L}_k^\dagger - \frac{1}{2}\{\hat{L}_k^\dagger \hat{L}_k, \rho_S\}\big)\Big) = \sum_k \gamma_k \text{Tr}\Big(\hat{n}_i \big(\hat{L}_k \rho_S \hat{L}_k^\dagger - \frac{1}{2}\hat{n}_i\{\hat{L}_k^\dagger \hat{L}_k, \rho_S\}\big)\Big). \tag{A.11}$$

We will consider only a single term for convenience. First, we show that if $[\hat{n}_i, \hat{L}_k] = 0$ the contribution is 0, which is behaviour we would expect for operators acting on different sites for example. If $\hat{n}_i$ and $\hat{L}_k$ commute (and consequently also $\hat{n}_i$ and $\hat{L}_k^\dagger$ commute) we can use this in combination with the cyclic property of the trace to rewrite the right hand site of equation (A.11) to

$$\gamma_k \text{Tr}\Big(\hat{n}_i\big(\hat{L}_k \rho_S \hat{L}_k^\dagger - \frac{1}{2}\hat{n}_i\{\hat{L}_k^\dagger \hat{L}_k, \rho_S\}\big)\Big) = \gamma_k \text{Tr}\Big(\hat{n}_i \hat{L}_k^\dagger \hat{L}_k \rho_S - \hat{n}_i \hat{L}_k^\dagger \hat{L}_k \rho_S\Big) = 0. \tag{A.12}$$

Let us now consider $[\hat{n}_i, \hat{L}_k] \neq 0$. The Lindblad operators in equation (1.16) are of the form $\gamma \hat{c}_k$ or $\gamma \hat{c}_k^\dagger$, which means that for $[\hat{n}_i, \hat{L}_k] \neq 0$ to hold we must have $i = k$. Let us first consider $\hat{L}_k = \gamma \hat{c}_k$. Substituting in equation (A.11) and again applying the cyclic property gives

$$\gamma \text{Tr}\Big(\hat{n}_i \hat{c}_i \rho_S \hat{c}_i^\dagger - \frac{1}{2}\hat{n}_i(\hat{c}_i^\dagger \hat{c}_i \rho_S + \rho_S \hat{c}_i^\dagger \hat{c}_i)\Big) = \gamma \text{Tr}\Big(\hat{c}_i^\dagger \hat{n}_i \hat{c}_i \rho_S - \hat{n}_i \hat{n}_i \rho_S\Big) = -\gamma \text{Tr}\Big(\hat{n}_i \hat{n}_i \rho_S\Big) = -\gamma\langle\hat{n}_i^2\rangle = -\gamma\langle\hat{n}_i\rangle. \tag{A.13}$$

In the second to last step we recognize that $\hat{n}_i \hat{c}\rho_S$ will always yield a factor 0. The final expression makes sense given the fact that the Lindblad operator in question models a drain. The current into the drain is dependent on the occupation of the site and is proportional to the coupling strength to the drain. The sign denotes the fact that particles are leaving the system.

Now let us consider $\hat{L}_k = \gamma \hat{c}_k^\dagger$:

$$\gamma \text{Tr}\Big(\hat{n}_i \hat{c}_i^\dagger \rho_S \hat{c}_i - \frac{1}{2}\hat{n}_i(\hat{c}_i \hat{c}_i^\dagger \rho_S + \rho_S \hat{c}_i \hat{c}_i^\dagger)\Big) = \gamma \text{Tr}\Big(\hat{c}_i \hat{c}_i^\dagger \hat{c}_i \hat{c}_i^\dagger \rho_S - \hat{n}_i(1 - \hat{n}_i)\rho_S\Big)$$
$$= \gamma\big(\langle(1 - \hat{n}_i)^2\rangle - \langle\hat{n}_i(1 - \hat{n}_i)\rangle\big) = \gamma\langle(1 - \hat{n}_i)^2\rangle = \gamma\langle 1 - \hat{n}_i\rangle. \tag{A.14}$$

This expression represents the opposite of the previous one. The Lindblad operator models a source. Particles can only enter the system if the site is not already fully occupied, and the current is proportional to the coupling strength. The positive sign denotes current is flowing into the system.

B   Additional Results
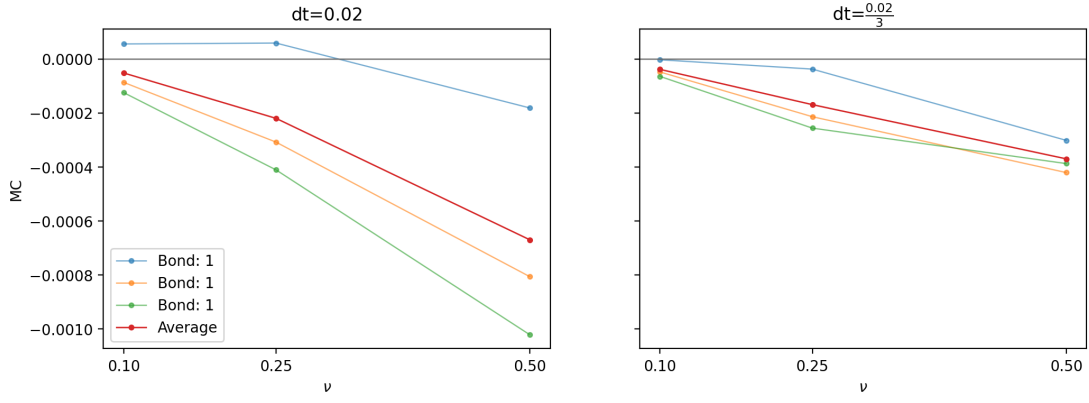
(a) Low driving.
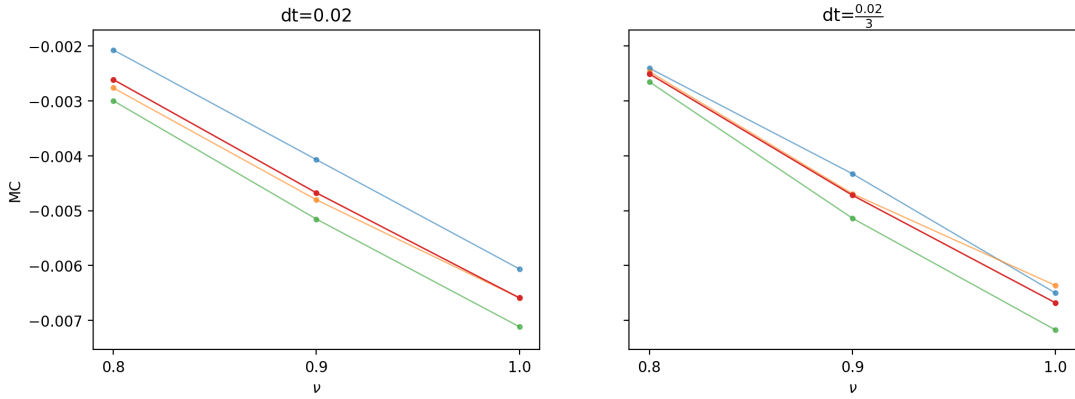
(b) High driving.

Figure B.1: Influence of a lower timestep size on the magnetocurrent profiles of the NESS for different drivings, $t = \lambda = 1$ and $U = 2$.
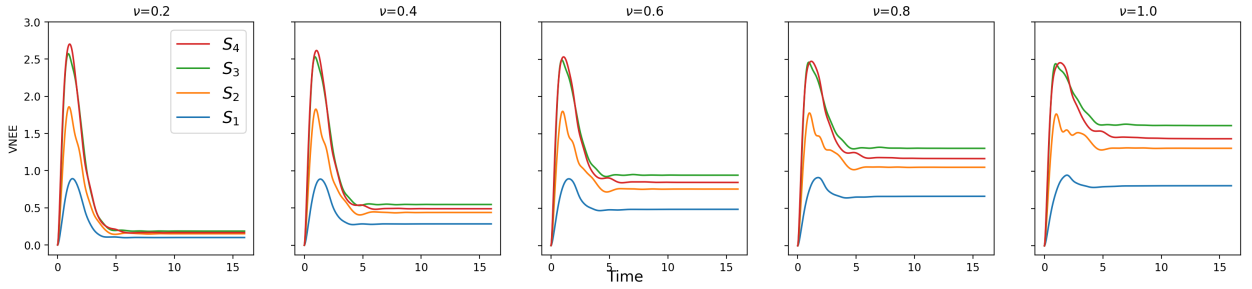
(a) Up-magnetised lead.
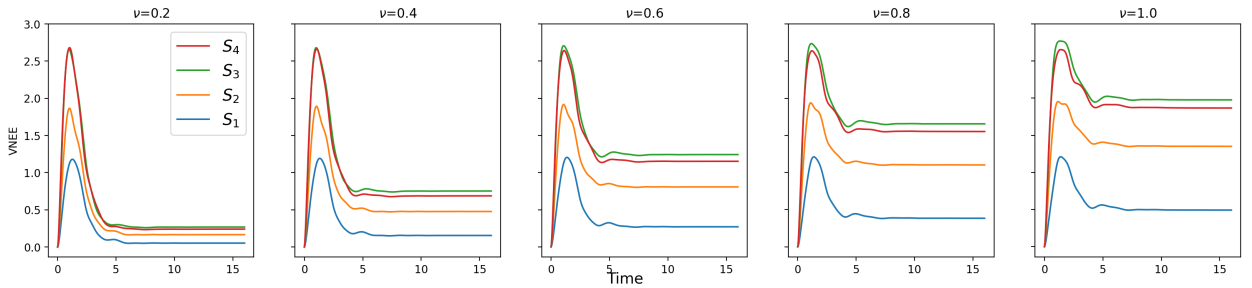
(b) Down-magnetised lead.

Figure B.2: Von Neumann entanglement entropy of the NESS of a chain of $L = 4$, $U = 1$ with spin-orbit coupling and magnetised leads for various bath parameters ν. Observe that the VNEE is hgihger for the down-magnetised lead. The VNEE is generally higher than in computations without the presence of spin-orbit coupling.
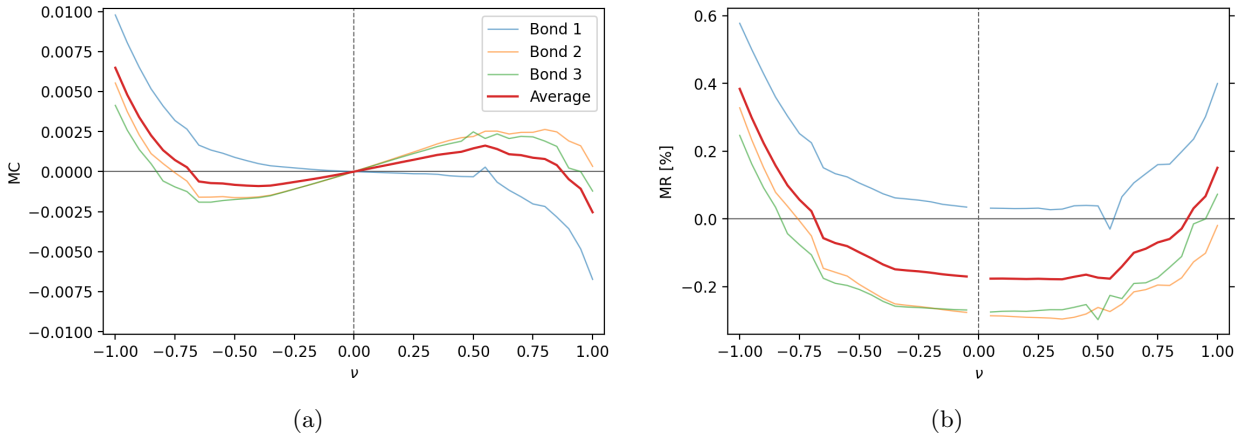
Figure B.3: (a) Magnetocurrent and (b) associated magnetoresistance for a 4-site molecule with $t = \lambda = U = 1$, with lefthanded chirality.
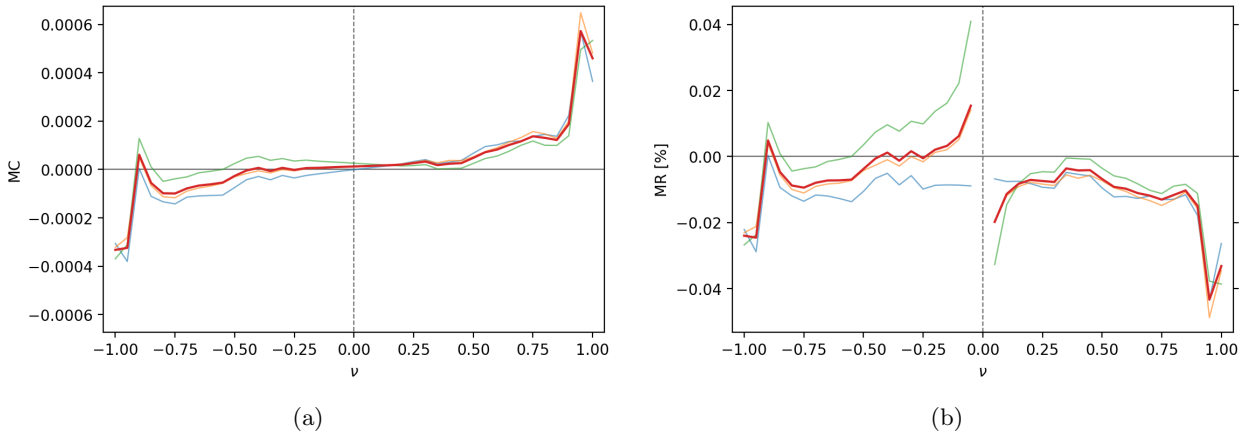
Figure B.4: (a) Magnetocurrent and (b) associated magnetoresistance for a 4-site molecule with $t = U = 1$ and $\lambda = 0.01$.
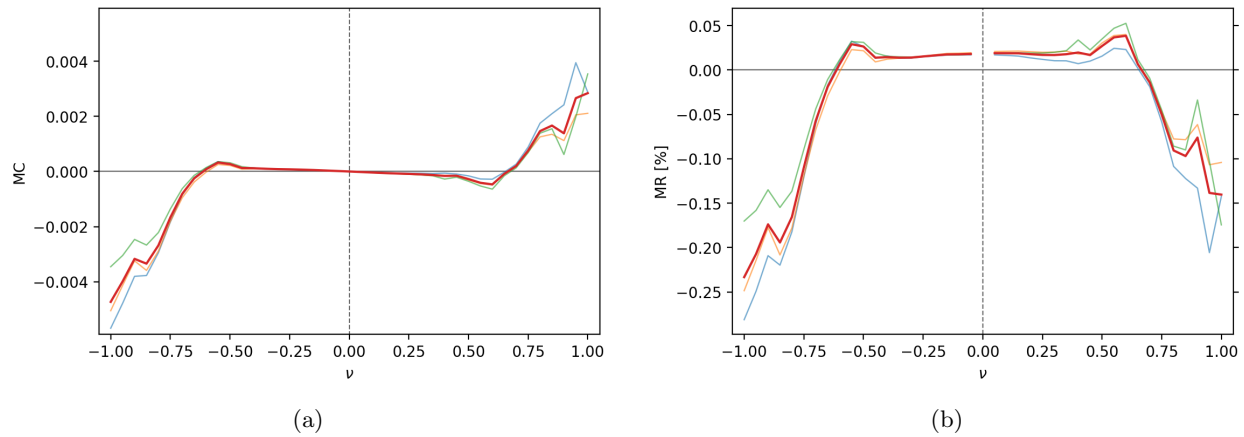
Figure B.5: (a) Magnetocurrent and (b) associated magnetoresistance for a 4-site molecule with $t = \lambda = U = 1$ and a different lead polarisation factor, $\eta = 2$ instead of $\eta = 5$. See the paragraph labeled 'The Leads' on page 36 for details.
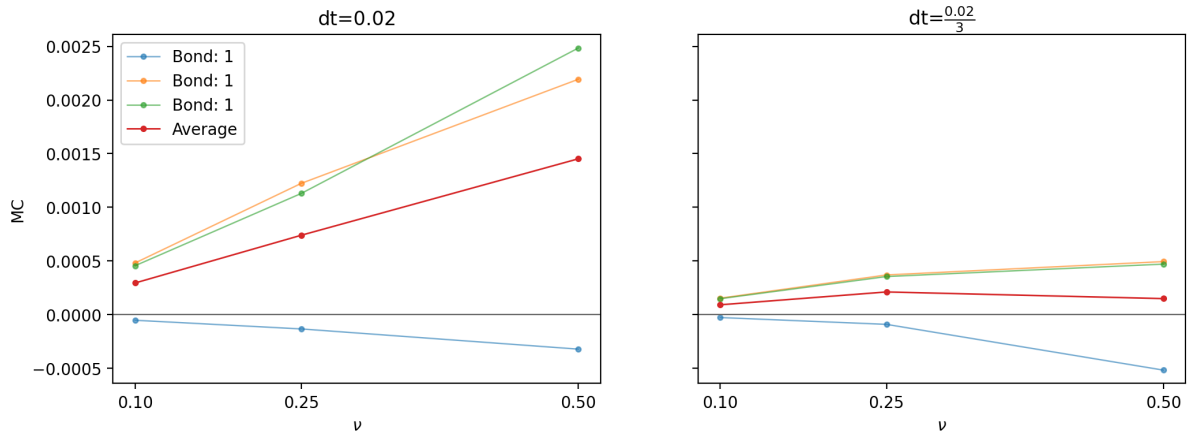
(a) Left-handed molecule.
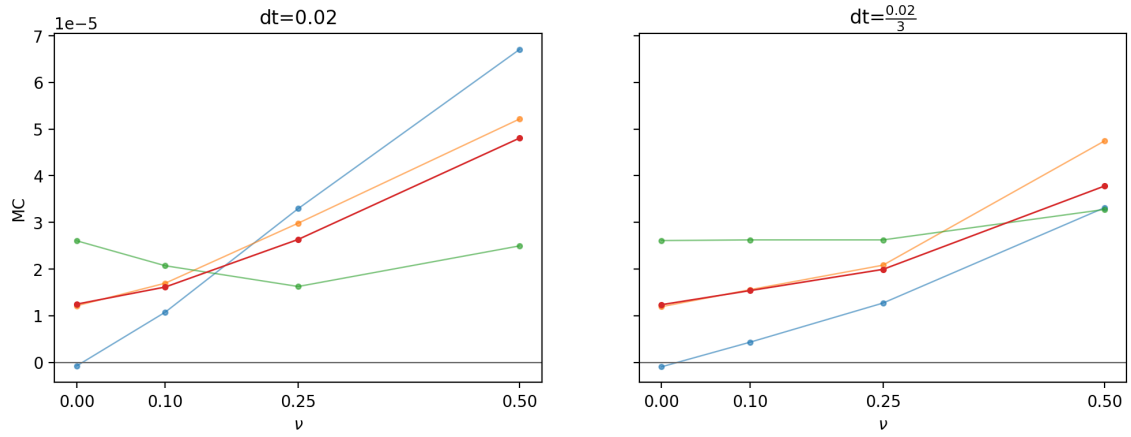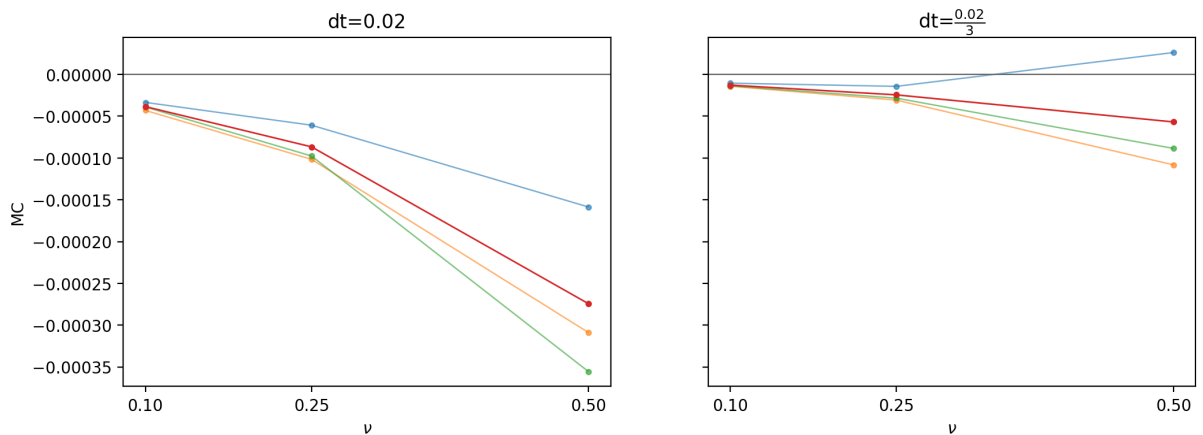
(b) $\lambda = 0.01$

(c) Magnetisation factor $\eta = 2$ instead of $\eta = 5$.

Figure B.6: Influence of a lower timestep size on the magnetocurrent profile of the NESS for different drivings in the low-to-medium driving regime.
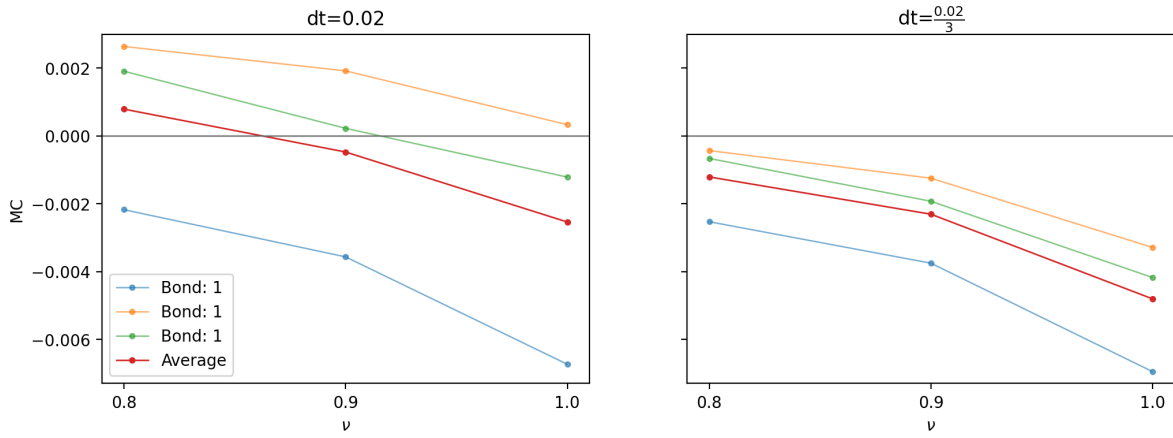
(a) Left-handed molecule.
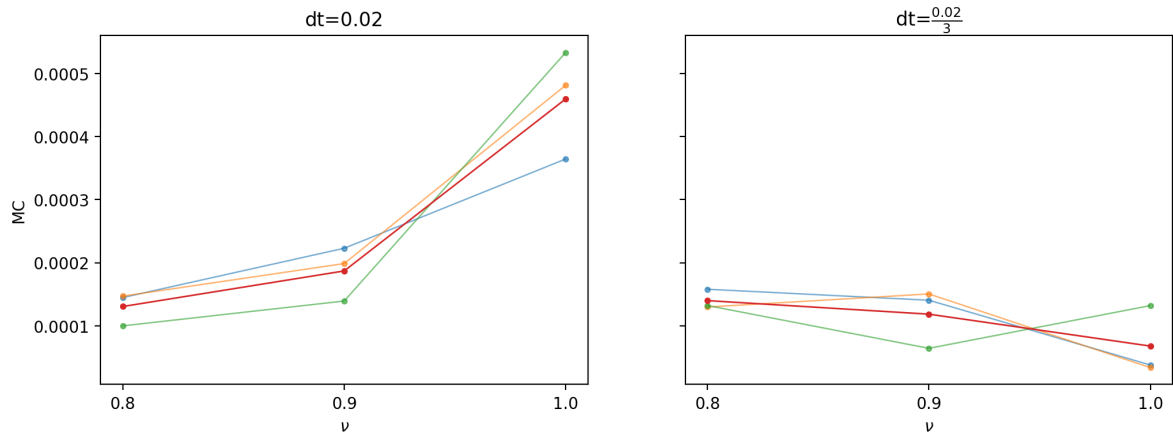
(b) $\lambda = 0.01$
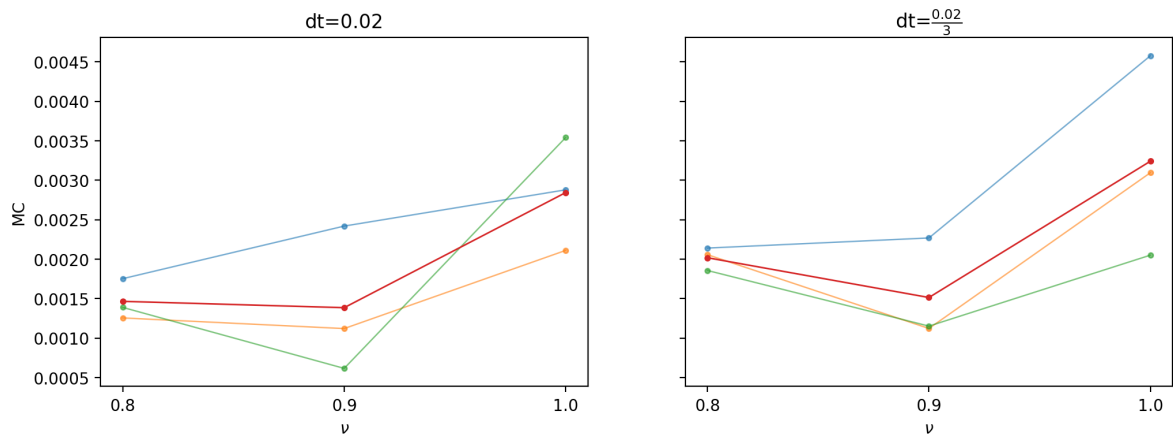
(c) Magnetisation factor $\eta = 2$ instead of $\eta = 5$.

Figure B.7: Influence of a lower timestep size on the magnetocurrent profile of the NESS for different drivings in the high driving regime.

C   Python Code

The python code used to obtain the results presented in this work can be found in the following repository:
`https://github.com/MatthijsRepository/CISS_MPS`